

# Fano Resonances in Plasmonic Nanostructures: Fundamentals, Numerical Modeling and Applications

THÈSE N° 5299 (2012)

PRÉSENTÉE LE 14 JUIN 2012

À LA FACULTÉ DES SCIENCES ET TECHNIQUES DE L'INGÉNIEUR  
LABORATOIRE DE NANOPHOTONIQUE ET MÉTROLOGIE  
PROGRAMME DOCTORAL EN PHOTONIQUE

ÉCOLE POLYTECHNIQUE FÉDÉRALE DE LAUSANNE

POUR L'OBTENTION DU GRADE DE DOCTEUR ÈS SCIENCES

PAR

**Benjamin GALLINET**

acceptée sur proposition du jury:

Prof. C. Moser, président du jury  
Prof. O. Martin, directeur de thèse  
Dr M.-A. Dupertuis, rapporteur  
Prof. H. Giessen, rapporteur  
Prof. P. J. Nordlander, rapporteur



ÉCOLE POLYTECHNIQUE  
FÉDÉRALE DE LAUSANNE

Suisse  
2012



# Acknowledgements

I would like first to thank Olivier for welcoming me at the Nanophotonics and Metrology Laboratory, the wonderful scientific discussions and advices, and for teaching me that research is a cocktail of curiosity, excitement, disappointments, dedication and patience. Thank you for transmitting to me the taste for research during these three years spent at NAM.

I would also like to thank all the NAM team. Andreas for introducing me to the surface integral method and for the great time developing together the program. Weihua, Thomas, Christian, Shourya and Andrea, I really enjoyed working with you. Thank you to all the other lab members: Lina for the initiation to Chinese culture, Sébastien, Sergio, Simon and Arash for the great times outside the lab, José, Guillaume, Daniele, Nicolas, Banafsheh, David, Volodymyr and Krishnan. A big thank you to Pierrette for taking care of all of us.

Thank you to the members of the thesis committee, Prof. Peter Nordlander, Prof. Harald Giessen, Dr. Marc-André Dupertuis and Prof. Christophe Moser, for taking the time to read the dissertation, accepting to sit at the examination, and for the fruitful scientific discussions.

Thank you to my parents, David, Aurélie, Lou, and my second family: René, Marie-Laure, Matthieu, Bertrand, Quentin, Nicole and Francis.

A very warm thank you to all my friends who made my stay in Lausanne unforgettable. A special thank you to Valérie for the moral support during the hard times, and for the patience when I could not stop thinking about Fano resonances.

Benjamin



# Abstract

Surface plasmons are able to generate extremely strong and confined optical fields at a deep-subwavelength scale, far beyond the diffraction limit, and now play a central role in nanosciences. A proper combination of plasmonic nanostructures can support Fano resonances arising from the interference between a non-radiative mode and a continuum of radiative electromagnetic waves. Fano resonances are able to confine light more efficiently and are characterized by a steeper dispersion than conventional plasmon resonances, which make them promising for nanoscale biochemical sensing, switching or lasing applications. Unfortunately, these technological developments are hindered by a lack of theoretical and numerical models able to deliver insights into the mechanisms of Fano resonances in plasmonic systems; e.g. to determine the best configuration for specific applications based on this phenomenon.

In this thesis, the fundamental properties of Fano resonances in plasmonic nanostructures, and more generally in non-conservative systems, are investigated. An *ab initio* framework to describe their properties is developed and an analytical formula for their spectral response is derived. An equivalence between the derived resonance formula and the model of two coupled oscillators is also drawn, which confirms the general character of the developed framework.

Furthermore, an original surface integral formulation for light scattering by periodic structures is developed and implemented. With this versatile numerical method, a very large variety of geometries can be simulated. The surface discretization using finite elements provides a high flexibility, allowing the investigation of irregular shapes. Thanks to the singularity subtraction technique, insights into the extreme near-field of the scatterers as well as into the corresponding far-field can be obtained with great accuracy. This particular advantage of the surface integral formulation, compared to other numerical methods, enables the detailed study of all the different aspects of Fano resonances in realistic plasmonic systems.

The developed theoretical and numerical models are then used to elaborate a methodology to tailor the optical response of plasmonic Fano resonances in the far-field and the near-field. It is also shown that there exist three different coupling regimes in Fano-resonant systems, each regime exhibiting specific properties: in the weak coupling regime, a very high sensitivity to the opening of a radiative channel for the dark mode is observed. An optimal regime of highest electromagnetic field enhancement is obtained only when the in and out-coupling balance intrinsic losses. Finally, for stronger coupling, the specific

---

features of Fano resonances are altered.

In the last part, this knowledge of the mechanisms of Fano–resonant plasmonic systems is translated to the optimization of nanoplasmonic systems for a broad range of applications. In the weak coupling regime, radiative losses of the dark mode are almost suppressed and the modulation depth becomes a physical value extremely sensitive to the modes coupling, which can be used for nanoscale plasmon rulers to measure nanometric displacements. In the intermediate regime, the best electromagnetic field enhancement is obtained, which optimizes devices for second harmonic generation, as well as for surface enhanced Raman scattering or antenna–based trapping for biomolecular recognition. The sensitivity of Fano–resonant systems to local perturbations of the refractive index is then discussed. Higher figures of merit than conventional plasmon resonances can be obtained because the contribution of radiative and non–radiative losses to the spectral width can be controlled. This analysis finally leads to the introduction of an intrinsic figure of merit for refractive index sensing using Fano–resonant systems.

**Keywords:** Plasmonics, optics, nanophotonics, plasmon resonance, Fano resonance, electromagnetically induced transparency, Wood anomalies, simulation, numerical technique, surface integral equation, boundary element method, periodic system, plasmon ruler, surface enhanced Raman scattering, refractive index sensing, nanosensor.

# Résumé

Les plasmons de surface peuvent générer des champs optiques extrêmement forts, et confinés à une échelle très petite par rapport à la longueur d'onde, loin au delà de la limite de diffraction ; ils jouent maintenant un rôle central dans les nanosciences. Une combinaison adaptée de nanostructures plasmoniques peut supporter des résonances Fano construites à partir de l'interférence d'un mode non radiatif avec un continuum d'ondes électromagnétiques radiatives. Les résonances Fano sont capables de confiner la lumière plus efficacement que les résonances plasmoniques conventionnelles, et sont caractérisées par une dispersion plus abrupte ; ce qui les rend particulièrement prometteuses dans le domaine des senseurs biologiques ou chimiques, de la communication ou des lasers. Malheureusement, ces développements technologiques sont gênés par le manque de modèles théoriques et numériques capables de délivrer une compréhension précise des mécanismes des résonances Fano dans des systèmes plasmoniques ; capables entre autres de déterminer la configuration la mieux adaptée pour des applications spécifiques basées sur ce phénomène.

Dans cette thèse sont étudiées les propriétés fondamentales des résonances Fano dans les nanostructures plasmoniques, et en général dans les systèmes non conservatifs. Sont également présentés un développement théorique *ab initio* pour décrire leurs propriétés, ainsi qu'une formule analytique pour leur réponse spectrale. Une équivalence entre cette formule et le modèle de deux oscillateurs couplés est aussi montrée, ce qui confirme le caractère général du développement théorique.

En outre, est développée et implémentée une méthode numérique originale d'intégrales de surface visant à simuler la diffusion de la lumière sur les structures périodiques. Grâce à cette méthode flexible, une très grande variété de géométries peut être simulée. La discrétisation en éléments finis garantit une grande flexibilité, d'où la possibilité par exemple d'étudier des structures irrégulières. Grâce à la technique de soustraction de singularité, la connaissance à la fois du champ extrêmement proche et du champ lointain correspondant peut être obtenue avec une très grande précision. Cet avantage particulier qu'apporte la technique d'intégrales de surface en comparaison avec les autres méthodes numériques, permet l'étude détaillée de tous les différents aspects des résonances Fano dans des systèmes plasmoniques réalistes.

Ces modèles théoriques et numériques sont ensuite utilisés pour l'élaboration d'une méthodologie ayant pour but de façonner la réponse optique des résonances Fano plasmoniques dans les champs proche et lointain. Est aussi montrée l'existence de trois différents

---

régimes de couplage dans les systèmes Fano, chacun étant caractérisé par des propriétés spécifiques : dans le couplage faible, une très forte sensibilité à l'ouverture d'un canal radiatif pour le mode sombre est observé. Le régime optimal pour l'accroissement du champ électromagnétique est obtenu uniquement quand le couplage équilibre les pertes intrinsèques. Si, enfin, le couplage est plus fort, les propriétés spécifiques des résonances Fano sont altérées.

La dernière partie montre que la connaissance acquise sur les mécanismes des résonances Fano peut être transférée vers l'optimisation de systèmes nanoplasmoniques dans le cadre d'une très grande variété d'applications. Dans le couplage faible, les pertes radiatives du mode sombre sont quasiment supprimées, et la profondeur de modulation devient une grandeur physique extrêmement sensible aux couplages des modes. Cet effet peut être utilisé pour mesurer optiquement des déplacements de l'ordre du nanomètre. Dans le régime intermédiaire est obtenu le meilleur accroissement du champ électromagnétique, ce qui est particulièrement utile pour l'optimisation de dispositifs utilisant la génération de seconde harmonique, ou la diffusion de Raman accrue par surface, ou encore le piégeage par antennes optiques pour la reconnaissance de biomolécules. La sensibilité des systèmes Fano aux perturbations locales d'indice de réfraction est ensuite discutée. Des facteurs de mérite plus élevés que les résonances plasmoniques conventionnelles peuvent être obtenus du fait que la contribution des pertes radiatives et non radiatives à la largeur spectrale peut être contrôlée. Cette analyse conduit finalement à l'introduction d'un facteur de mérite intrinsèque pour les senseurs d'indice de réfraction utilisant les résonances Fano.

**Mots-clés:** Plasmonique, optique, nanophotonique, résonance plasmon, résonance Fano, transparence induite électromagnétiquement, anomalies de Wood, simulation, technique numérique, équation intégrale de surface, méthode à éléments de bord, système périodique, mesureur plasmonique, diffusion Raman accrue par surface, senseur à indice de réfraction, nanosenseur.



# Contents

Acknowledgements	iii
Abstract (English/Français)	v
Introduction	1
<b>1 Fundamentals of plasmonic Fano resonances</b>	<b>5</b>
1.1 Historical Perspective . . . . .	5
1.1.1 Fano’s quantum formulation . . . . .	6
1.1.2 Coupled–mode theory . . . . .	9
1.2 Equivalent model of two coupled classical oscillators . . . . .	12
1.2.1 Classical equivalent of Fano resonance formula . . . . .	13
1.2.2 Generalized Fano resonance formula . . . . .	16
1.3 Electromagnetic theory . . . . .	19
1.3.1 Dark mode and radiative waves . . . . .	19
1.3.2 Dark mode and bright mode . . . . .	24
1.4 Conclusion . . . . .	26
<b>2 Surface integral equation method for periodic nanostructures</b>	<b>27</b>
2.1 Surface integral equations for periodic systems. . . . .	28
2.2 Numerical implementation . . . . .	33
2.2.1 Evaluation of the periodic Green’s function with Ewald’s method . . . . .	33
2.2.2 Solution by Method of Moments . . . . .	37
2.3 Convergence assessment . . . . .	40
2.3.1 Infinite planar interfaces . . . . .	41
2.3.2 Photonic crystal . . . . .	42
2.3.3 Asymmetric metallic film . . . . .	45
2.3.4 Negative-index metamaterial . . . . .	45
2.4 Conclusion . . . . .	46
<b>3 Mechanisms of plasmonic Fano resonances</b>	<b>47</b>
3.1 Effects of electromagnetic interactions on the line shape . . . . .	47
3.1.1 Separable bright and dark modes . . . . .	51
3.1.2 Plasmon hybridization and Fano resonances . . . . .	54

## Contents

---

3.1.3	Excitation of first orders in metallic photonic crystals . . . . .	58
3.2	Relation between near-field and far-field . . . . .	59
3.3	Conclusion . . . . .	64
<b>4</b>	<b>Applications</b>	<b>65</b>
4.1	Three coupling regimes in Fano resonances: implications for sensing. . . .	65
4.1.1	Plasmon Rulers . . . . .	68
4.1.2	Field enhancement and surface enhancement Raman scattering (SERS) . . . . .	69
4.1.3	Refractive index sensing . . . . .	72
4.2	Towards large scale fabrication . . . . .	78
4.3	Conclusions . . . . .	81
<b>5</b>	<b>Conclusion</b>	<b>83</b>
<b>A</b>	<b>Derivation of specific equations</b>	<b>87</b>
A.1	Classical equivalent of Fano resonance formula . . . . .	87
A.2	Generalized Fano formula in non-reciprocal systems . . . . .	88
A.3	Electromagnetic Fano resonance formula . . . . .	89
A.4	Field enhancement . . . . .	90
A.5	Complex integrals . . . . .	91
<b>B</b>	<b>List of symbols</b>	<b>93</b>
	<b>Bibliography</b>	<b>108</b>
	<b>Curriculum Vitae</b>	<b>109</b>

# Introduction

One of the major conceptual steps of quantum mechanics was to introduce the wave–particle dual character of matter [1]. Photonics aims at revisiting the duality wave–photon and controlling light propagation via interaction with matter [2, 3]. The interaction of light with matter has always been a major topic in modern physics. During the pioneering times of quantum mechanics in 1913, the study of Rydberg spectral lines in the hydrogen atom led Niels Bohr to develop his model for the atomic structure. While performing spectroscopy of sodium lines in 1902, Wood observed that at particular angle of incidences, the metallic grating he was using could show only one of the D lines, but not the other [4]: under white light illumination, the grating was in fact showing sharp variations in its spectrum within an extremely small wavelength interval. As this effect could not be explained at that time by conventional grating theories, these variations were called anomalies and Wood himself confessed that this problem was ‘one of the most interesting that [he had] ever met with’. Later on, Wood anomalies were attributed to oscillations of the conduction electrons plasma together with the electromagnetic field at the surface of the metallic grating [5, 6]. The quasiparticles arising from the quantization of these oscillations are called surface plasmon polaritons [7].

The origins of plasmonics are particularly difficult to trace since surface plasmons polaritons have been rediscovered in a variety of different contexts throughout the 20<sup>th</sup> century. Certainly one of the earliest utilization of them is found back in the middle–ages, where specific color effects could be obtained from metallic nanoparticles embedded in stained–glass windows, depending on their size, their shape and the material they were made of (usually coinage metals such as gold, silver, aluminum or copper) [8]. In 1998, it was discovered that a metallic film drilled with subwavelength holes enables the transmission of light by an amount much greater than could normally allow the aperture area [9–11]. It was then realized that surface plasmons are able to generate extremely strong and confined optical fields at a deep–subwavelength scale, far beyond the diffraction limit. The development of the nanofabrication techniques in the last two decades has enabled the control of light at the nanometer scale around plasmonic structures, giving to plasmonics a central role in nanosciences [12]. An interesting fact is that plasmon polaritons oscillations around metallic nanostructures are in many ways analogous to electronic wavefunctions in atoms and many quantum mechanical phenomena can be

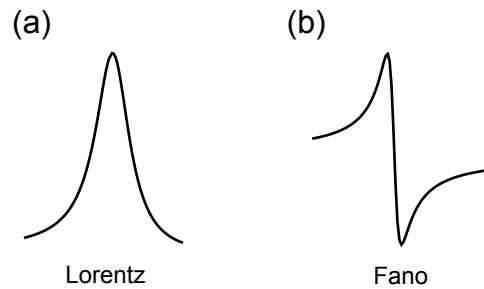


Figure 1: Spectral distributions for (a) Lorentzian resonances and (b) Fano resonances.

reproduced and controlled at the nanoscale in plasmonic systems [13].

It has been recently shown that a proper combination of plasmonic nanostructures can also support Fano resonances [14, 15]. In plasmonic systems, these resonances arise from the interference between a non-radiative mode and a continuum of radiative electromagnetic waves, and are distinguished from their Lorentzian counterpart by a characteristic asymmetric line shape. Fano resonances bear their name from Ugo Fano, who elaborated a theory unifying Wood anomalies in metallic gratings with the process of autoionization in atoms under a general interference phenomenon, and derived an analytical formula for the resulting asymmetric spectral line shape, now known as Fano formula [16–18]. His seminal paper of 1961 became one of the most important physics publications of the 20<sup>th</sup> century and has inspired for decades researchers in the field of atomic and condensed matter spectroscopy, and more recently in photonics [15]. In fact, both plasmon and Fano resonances can be originally traced back to the discovery of Wood [4] and have a very intricate story. Fano-type interferences were attributed to the phenomenon of extraordinary transmission through metallic films [10, 11, 19], and appear nowadays in a variety of sophisticated nanophotonic systems [13–15]. They have very recently attracted significant attention because quasi-localized optical modes with reduced radiative damping can be excited [14, 15], allowing in particular the development of plasmonic nanolasers [20]. Their integration with non-linear and phase-change media also finds applications in switching and electro-optics [21–23]. Electromagnetically induced transparency (EIT) is based on the Fano interference of the transition probability amplitude of two atomic states with similar energies [24]; the induced steep dispersion can be used to drastically reduce the group velocity of light in plasmonic metamaterials [25–27].

The control of the line shape of Fano resonances in plasmonic nanostructures for specific applications remains a challenging task and requires a theory able to understand the underlying physical mechanisms. Numerical and experimental data are usually fitted and analyzed with a classical analog of two coupled mechanical oscillators [28, 29] or other intuitive phenomenological models [30–32]. The quantum mechanical theory developed by Fano to explain autoionization of atoms provides a wave-like interpretation of asymmetric resonances [18], which can be adapted to a Lorentzian distribution of

the continuum [33, 34], but is not able to describe the role of intrinsic losses inherent to plasmonic systems. This is particularly critical because the mechanisms of energy transfer and energy losses in Fano-resonant plasmonic systems are fundamental to understand and optimize their implementation in future applications. Hence, a consistent and general analysis and understanding of the phenomenon of Fano-like resonances in plasmonic nanostructures is still lacking. This need of a theoretical model is accompanied by the need of a numerical method able to handle accurately the extreme near-field enhancement and the sensitivity to the geometry and fabrication conditions characteristic of Fano resonances.

In the recent literature, it was often speculated that Fano resonances are able to confine light more efficiently and are characterized by a steeper dispersion than conventional Lorentzian resonances [14, 15], which make them promising for local refractive index sensing applications [35–40] or surface enhanced Raman scattering [41]. Thanks to their extreme sensitivity to local geometrical changes makes, they also have been recently proposed as nanometer scale strain monitors or biomolecular rulers [13, 42]. However, it has never been investigated which configuration is the most sensitive, and under which conditions Fano resonances can overcome conventional plasmon resonances.

The objective of this thesis is to address these different shortcomings by developing a theoretical and numerical model to study in depth the mechanisms of Fano resonances in plasmonic systems. This model will then be used to determine the best plasmonic configurations for specific sensing applications.

This thesis is organized as follows. Chapter 1 will be dedicated to an *ab initio* model of Fano resonances in plasmonic and more generally in non-conservative systems. After an historical review of the existing theoretical models for Fano resonances, the classical analog of two coupled oscillators will be discussed and followed by the electromagnetic model based on Maxwell's equations. In particular, the generalization of Fano formula for non-conservative systems will be derived. In Chapter 2, the development of a surface integral formulation for the electromagnetic scattering by periodic nanostructures will be detailed. This formulation combines the advantages of both differential and integral numerical methods in terms of accuracy and versatility. The validity of the method will then be addressed along with its convergence properties. The results of the first two chapters will be used in Chapter 3 to illustrate the mechanisms of plasmonic Fano resonances in the near-field and in the far-field, as well as to provide a method to tailor the line shape of their spectral response. In Chapter 4, I will show how the results obtained in this thesis will impact on the development of applications based on the Fano effect, such as nanoscale biochemical sensors and rulers, surface-enhanced Raman spectroscopy and nanolasers. Then, a nanoimprint based fabrication method of Fano-resonant nanostructures will be presented. Each topic in this thesis will be completed with a concluding statement and review of the main results. A general conclusion will be finally given, along with an outlook for future developments.



# 1 Fundamentals of plasmonic Fano resonances

The development of an *ab initio* model from Maxwell's equations for Fano resonances represents the fundamental aspect of this thesis, and part of this work is published in Refs. [43] and [44]. In particular, a generalization of Fano formula for non-conservative systems will be derived. After an historical overview of different theoretical descriptions of Fano resonances, the classical analog of two coupled oscillators will be discussed in Section 1.2. The classical equivalent of the resonance formulas derived in this section provides an intuitive description of the main features of Fano resonances. Finally, a comprehensive derivation of the model based on Maxwell's equations and Feshbach formalism will be exposed.

## 1.1 Historical Perspective

The first observation of asymmetric line shapes was done by Wood in 1902 when illuminating white light onto metallic diffraction gratings [4]. He observed that the intensity of their response can be 'extremely brilliant up to a certain wavelength', but suddenly 'drops almost to zero' within a very small wavelength range, comparable to the distance between two sodium D lines. As a result, at a certain angle of incidence, the grating was able to show one of the D lines, but not the other. These rapid variations in intensity were called anomalies since they could not be explained by grating theories at that time. The dynamical theory of gratings developed by Lord Rayleigh in 1907 was based on the expansion of the electromagnetic field in radiative waves. It was able to predict the wavelengths at which these anomalies occur (Rayleigh wavelengths), but could not describe the line shape of the grating response at these particular wavelengths [45]. In 1936, Ugo Fano extended Rayleigh's theory to evanescent waves propagating at the surface of the grating [16], and could describe the asymmetric behavior of Wood's anomalies: at Rayleigh's wavelengths, evanescent waves are excited at the grating surface and interfere with propagating waves in such a way that a maximum and a minimum in intensity are observed in a small frequency interval. A formula for these characteristic

asymmetric line shapes was developed and is now known as Fano formula [16]. The observation of asymmetric peaks in the absorption spectra of noble gases by Beutler [46] led Fano to improve his original derivation of the formula to describe both phenomena in a unified way [18]. Thus, the interaction between a discrete state and a continuum at the same energy level in Rydberg atoms was described as a similar phenomenon as the interaction of excited evanescent waves with incoming radiation in a metallic grating. This seminal work for the understanding of matter–radiation interaction has inspired for decades researchers in the field of atomic and condensed matter spectroscopy, and more recently in photonics [15].

Fano resonances in plasmonic nanostructures are usually fitted and described with the Fano formula [14]. As Fano’s quantum formulation will be extensively referred to in this chapter and for the sake of acknowledging his seminal work, its main results are summarized in Section 1.1.1. Another common approach in photonics is to make use of phenomenological models, such as a classical analogy [28, 29, 47] or the coupled–mode theory [31, 32]. These models are able to illustrate intuitively some features of the Fano interference process, as will also be discussed in Section 1.2. In Section 1.1.2, the main results of coupled–mode theory are summarized.

### 1.1.1 Fano’s quantum formulation

In this section, the main results of Fano’s quantum mechanical model are exposed [18]. First, consider an atomic system with a discrete state  $\psi_d$  of energy  $E_d$  and a continuum of states  $\psi_E$ . Each of these states is assumed to be non degenerate. In the following, the energy submatrix belonging to the subset of states  $\psi_d, \psi_E$  will be diagonalized. Its elements constitute a square submatrix:

$$\langle \psi_d | H | \psi_d \rangle = E_d, \quad (1.1)$$

$$\langle \psi_{E'} | H | \psi_d \rangle = V_{E'}, \quad (1.2)$$

$$\langle \psi_E | H | \psi_{E'} \rangle = E' \delta(E' - E). \quad (1.3)$$

The discrete energy level  $E_d$  lies within the continuous range of values of  $E'$ . The eigenvector of the energy matrix is assumed to have the form:

$$\chi_E = a\psi_d + \int dE' b_{E'} \psi_{E'}, \quad (1.4)$$

where  $a$  and  $b_{E'}$  are also functions of  $E$ , but this dependence is kept implicit in the following. These coefficients are determined as solutions of the system of equations in



Eq. (1.1):

$$E_d a + \int dE' V_{E'}^* b_{E'} = E a, \quad (1.5)$$

$$V_{E'} a + E' b_{E'} = E b_{E'}. \quad (1.6)$$

The formal solution of this system of equations can be written as

$$b_{E'} = \left[ \frac{1}{E - E'} + z(E) \delta(E - E') \right] V_{E'} a, \quad (1.7)$$

where  $z(E)$  is assumed real. The asymptotic behavior of  $\chi_E$  is now compared to the continuum. If the states  $\psi_E$  are represented by a wave function with asymptotic behavior  $\propto \sin[k(E)r]$ , their superposition [Eq. (1.4)] has the following asymptotic behavior:

$$\int dE' b_{E'} \psi_{E'} \propto \{-\pi \cos[k(E)r] + z(E) \sin[k(E)r]\}, \quad (1.8)$$

$$= \sin[k(E)r + \Delta\phi], \quad (1.9)$$

in which  $\Delta\phi = -\arctan[\pi/z(E)]$  represents the phase shift due to the interaction between the continuum of states  $\psi_E$  and the discrete state  $\psi_d$ . Substituting Eq. (1.7) into Eq. (1.5) leads to an expression for  $z(E)$ :

$$z(E) = \frac{E - E_d - F(E)}{|V_E|^2}, \quad (1.10)$$

where

$$F(E) = \mathcal{P} \int dE' \frac{|V_{E'}|^2}{E - E'}, \quad (1.11)$$

where  $\mathcal{P}$  means that the principal value of the integral is taken. The phase shift  $\Delta\phi$  varies by  $\sim \pi$  as  $E$  covers an interval  $\sim |V_E|^2$  about the resonance at  $E = E_d + F$ . Therefore, the quantity  $F$  represents a shift from the discrete state's resonance position  $E_d$ . With proper normalization, the coefficients of the decomposition (1.4) are given by [18]:

$$a = \frac{\sin \Delta\phi}{\pi V_E}, \quad (1.12)$$

$$b_{E'} = \frac{V_{E'}}{\pi V_E} \frac{\sin \Delta\phi}{E - E'} - \delta(E - E') \cos \Delta\phi. \quad (1.13)$$

The probability of excitation of the stationary state  $\chi_E$  is now studied. This probability is represented by the squared matrix element of a transition operator  $T$  between an initial state  $i$  and the state  $\chi_E$ . Using Eqs. (1.4) and (1.12) this matrix element can be written as:

$$\langle \chi_E | T | i \rangle = \frac{1}{\pi V_E^*} \langle \Psi_d | T | i \rangle \sin \Delta\phi - \langle \psi_E | T | i \rangle \cos \Delta\phi, \quad (1.14)$$

where

$$\Psi_d = \psi_d + \mathcal{P} \int dE' \frac{V_{E'} \psi_{E'}}{E - E'}, \quad (1.15)$$

indicates the state  $\psi_d$  'modified by an admixture of states of the continuum' [18]. The sharp variation of  $\Delta\phi$  as  $E$  around the resonance position  $E = E_d + F$  induces a sharp variation of  $\langle \chi_E | T | i \rangle$ . Since  $\sin \Delta\phi$  is an even function and  $\cos \Delta\phi$  an odd function of  $E - E_d - F$ , their respective contributions to  $\langle \chi_E | T | i \rangle$  by  $\langle \Phi | T | i \rangle$  and  $\langle \psi_E | T | i \rangle$  'interfere with opposite phase on the two sides of the resonance', which is a characteristic feature of Fano resonances [18]. Fano also made the observation that the 'transition probability vanishes on one side of the resonance' [18]. An analytical formula for the transition probability is now derived. The reduced energy is defined by

$$\epsilon = -\cot \Delta\phi = \frac{E - E_d - F}{1/2\Gamma}, \quad (1.16)$$

in which  $\Gamma = 2\pi|V_E|^2$  indicates the spectral width of the autoionized state  $\psi_d$ . The parameter which coincides with the zero of the resonance is given by:

$$q = \frac{\langle \Psi_d | T | i \rangle}{\pi V_E^* \langle \psi_E | T | i \rangle}. \quad (1.17)$$

The ratio of the transition probability  $|\langle \chi_E | T | i \rangle|^2$  to the probability  $|\langle \psi_E | T | i \rangle|^2$  of transition of the unperturbed continuum can be represented by a single family of curves depicted in Fig. 1.1 [18]:

$$\frac{|\langle \chi_E | T | i \rangle|^2}{|\langle \psi_E | T | i \rangle|^2} = \frac{(\epsilon + q)^2}{\epsilon^2 + 1}. \quad (1.18)$$

The parameter  $q$ , as the ratio of transition probabilities between the discrete state and the continuum, describes the degree of asymmetry of the resonance.

The same procedure can be generalized to an arbitrary number of continua  $\psi_{1E}, \psi_{2E}, \dots$  that may be distinguished by suitable quantum numbers. The probability of transitions from an initial state  $i$  to all the stationary states of energy  $E$ :

$$|\langle \chi_{1E} | T | i \rangle|^2 + |\langle \chi_{2E} | T | i \rangle|^2 + \dots, \quad (1.19)$$

where the first term of this sum varies as a function of energy following Eq. (1.18). The other terms correspond to continua that do not interact with the discrete auto-ionizing state [48].

At this point, a few remarks need to be made. The interaction between the direct radiation of the continuum and the excitation of the discrete state is in fact a very general interference process and Fano's approach is able to provide analytical expressions for the

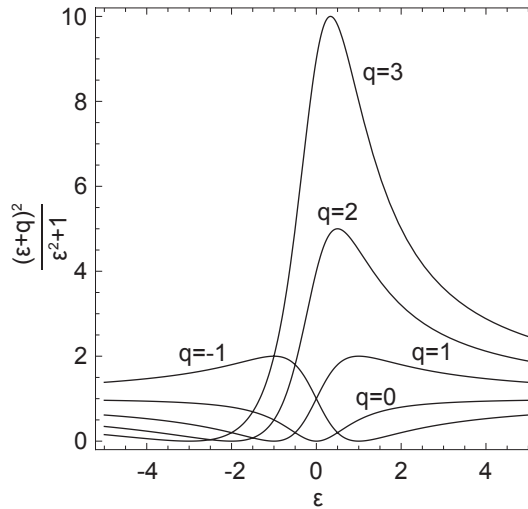


Figure 1.1: Natural line shapes for different values of  $q$ , adapted from Ref. [18].

line shape of asymmetric resonances in a unified way. However, its basic assumption of real energy eigenvalues fails when dealing with plasmonic nanostructures because of the conversion of electromagnetic energy into heat by Joule effect in the metal. An equivalent model based on Maxwell's equations with hermitian operators would not be able to describe this effect either.

### 1.1.2 Coupled-mode theory

The Fano effect is not restricted to quantum systems but is a very general wave interference phenomenon that has also been reported in the optical transmission and reflection spectra for a wide variety of structures such as metallic or dielectric gratings [4, 17, 49] or photonic systems [30, 31, 50]. The coupled-mode theory developed for waveguide-cavity systems introduces a general concept of 'transport processes from multiple input and output ports through a single-mode optical resonator' [31]. In a two-port system with mirror symmetry such as a photonic crystal slab, the observed Fano line shape can be reproduced.

We now wish to expose the main results of temporal coupled-mode theory applied to light scattering by a single obstacle [32], including plasmon resonant nanoparticles of particular interest in this thesis. In this context, the Fano effect is the result of interference of two pathways: the direct scattering of the incoming wave and the outgoing radiation from the excited resonance. The coupling constants are constrained by energy-conservation and time-reversal symmetry considerations. Although the results of this section are not based on *ab initio* considerations, they are able to illustrate intuitively the impact that the coupling constants have on the asymmetry of the Fano line shapes. Using the temporal coupled-mode theory formalism, the dynamic equation for the amplitude  $c$  of

the resonance is [32]:

$$\frac{dc}{dt} = (-i\omega_0 - \gamma_0 - \gamma)c + \iota h^+, \quad (1.20)$$

$$h^- = Bh^+ + \eta c, \quad (1.21)$$

where  $h^+$  and  $h^-$  stand for the incoming and outgoing waves respectively,  $\omega_0$  is the resonance frequency,  $\gamma_0$  the intrinsic loss rate due for example to material absorption,  $\gamma$  the external leakage rate due to the coupling of the resonance to the outgoing wave and  $B$  the background reflection coefficient. The quantities  $\iota$  and  $\eta$  correspond to the coupling constant between the resonance and the incoming or outgoing wave, respectively. The coupled-mode formalism is valid only when  $\gamma_0 + \gamma \ll \omega_0$ .

The coupling constant  $\iota$  and  $\eta$  are related to each other by energy conservation and time-reversal symmetry considerations. For  $\gamma_0 = 0$  (lossless case) and no incoming wave ( $h^+ = 0$ ), the solution of Eq. (1.20) has the following form:

$$c = Ae^{-i\omega_0 t - \gamma t}, \quad (1.22)$$

$$h^- = A\eta e^{-i\omega_0 t - \gamma t}, \quad (1.23)$$

where  $A$  is an arbitrary constant. According to energy conservation, the energy leakage rate must be equal to the power of the outgoing wave:

$$\frac{d|c|^2}{dt} = -2\gamma|c|^2 = -|h^-|^2 = -|\eta|^2|c|^2, \quad (1.24)$$

which requires that

$$|\eta|^2 = 2\gamma. \quad (1.25)$$

The time-reversed case of Eq. (1.22) corresponds to feeding the resonator with exponentially growing wave amplitude  $(h^-(-t))^*$ . Such excitation results in a resonant amplitude  $(c(-t))^*$  growing exponentially. Using Eq. (1.20):

$$\iota\eta^* = 2\gamma \quad (1.26)$$

$$B\eta^* + \eta = 0. \quad (1.27)$$

Combining Eqs. (1.25) and (1.26), one gets:

$$\iota = \eta. \quad (1.28)$$

If the system is lossless, the background reflection is  $B = e^{i\phi}$  and therefore:

$$\iota = \eta = \sqrt{2\gamma} e^{i(\phi/2 + \pi/2 - n\pi)}, \quad (1.29)$$

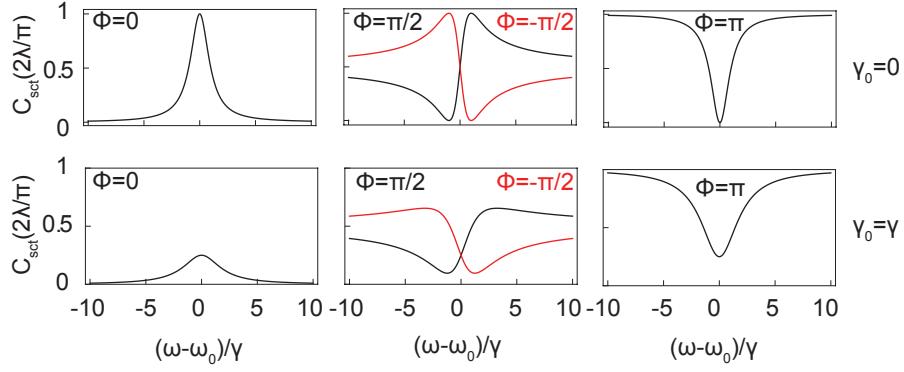


Figure 1.2: Scattering cross section as a function of the frequency for different values of the background reflection phase  $\phi$  and intrinsic losses  $\gamma_0$ .

where  $n$  is an arbitrary integer. It is expected that the strongest contribution of intrinsic losses is to the resonant properties. As an ansatz, a nonzero intrinsic loss rate  $\gamma_0$  is introduced in Eq. (1.20), while the background scattering is still approximated as a lossless process [32]. Assuming that the incoming wave oscillates at a frequency  $\omega$ , the reflection coefficient  $r = h^-/h^+$  can be obtained from Eqs. (1.20) and (1.29):

$$r = e^{i\phi} + \frac{\eta^2}{i(\omega_0 - \omega) + \gamma_0 + \gamma} = e^{i\phi} \frac{i(\omega_0 - \omega) + \gamma_0 - \gamma}{i(\omega_0 - \omega) + \gamma_0 + \gamma}. \quad (1.30)$$

Using scattering theory [32], the corresponding scattering and absorption cross sections can be written as:

$$C_{\text{sct}} = \frac{2\lambda}{\pi} \left| \frac{1}{2} \frac{(i(\omega_0 - \omega) + \gamma_0)(e^{i\phi} - 1) - \gamma(1 + e^{i\phi})}{i(\omega_0 - \omega) + \gamma_0 + \gamma} \right|^2, \quad (1.31)$$

$$C_{\text{abs}} = \frac{2\lambda}{\pi} \frac{\gamma_0\gamma}{(\omega - \omega_0)^2 + (\gamma_0 + \gamma)^2}, \quad (1.32)$$

where  $\lambda = 2\pi c/\omega$  is the vacuum wavelength. The absorption cross section is a Lorentzian of width  $\gamma_0 + \gamma$  to which both the intrinsic losses and external leakage contribute. However, the scattering cross section can display asymmetric features, as it involves the interference between the resonant mode and the background radiation (Fig. 1.2). For particular values of the frequency, the directly scattered waves can interfere destructively with the waves that have excited and are re-emitted by the resonant mode, resulting in a transparency of the system and a dip in the scattering cross section. The phase  $\phi$  of the background reflection coefficient appears to be a key parameter in the asymmetry of the resonance. For  $\phi = 0$ , the scattering cross section is a Lorentzian (corresponding to  $q = \infty$ ), whereas for  $\phi = \pi$  it becomes an anti-Lorentzian (corresponding to  $q = 0$ ). For intermediate values of  $\phi$ , the asymmetry parameter appears to be finite and its sign is controlled by the sign of  $\phi$ . By incorporating intrinsic losses to the system ( $\gamma_0 = \gamma$ ), the scattering

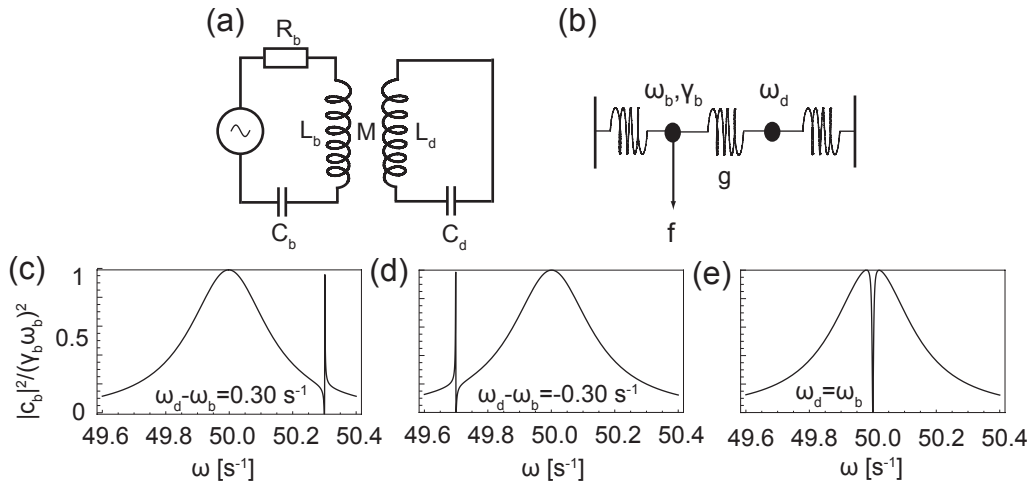


Figure 1.3: (a) Electrical circuit analog of Fano resonances: the LC circuit is excited only through its inductive coupling to the RLC circuit. (b) Mechanical model of Fano resonances: two coupled oscillators B and D with resonance frequencies  $\omega_b$  and  $\omega_d$  respectively. The oscillator B has a damping  $\gamma_b$  and is forced by an external excitation with amplitude  $f$ . Their coupling constant is  $g$ . (c-e) Amplitude of the forced oscillator as a function of the excitation frequency for different values of detuning  $\omega_d - \omega_b$  (with  $\omega_b = 50.00 \text{ s}^{-1}$ ,  $g = 2.00 \text{ s}^{-2}$  and  $\gamma_b = 0.30 \text{ s}^{-1}$ ).

cross section does not reach zero, which was a characteristic feature of Fano resonances.

The coupled-mode formalism is able to illustrate some features of the interference process but cannot provide general analytical expressions for the line shape of the resonance, the asymmetry parameter nor the role of intrinsic losses. In the following, the intuitive model of coupled oscillators is discussed and an analytical expression for the Fano resonance line shape and its parameters are derived.

## 1.2 Equivalent model of two coupled classical oscillators

In 1951, Lamb and co-workers [47] suggested an RLC circuit coupled to a LC circuit to model the interference between two transitions in the fine structure of the hydrogen atom [Fig. 1.3(a)]. The equivalent system of two masses, each one attached by a spring to the wall, with an additional spring between them, has been presented as classical analog for electromagnetically induced transparency [24, 28] and Fano resonances [29] [Fig. 1.5(a)]. Both the RLC circuit and the connected masses satisfy the equations of motion of two coupled oscillators. Apart from bringing an intuitive understanding about the interference mechanisms behind Fano resonances in atomic and photonic systems, this classical analogy is commonly used for fitting numerical and experimental spectra. With these approaches, one is able to extract the individual properties of each oscillator,

## 1.2. Equivalent model of two coupled classical oscillators

---

but it is not possible to quantitatively discuss their influence on the coupled system. In this Section, I show that the response of the system of coupled oscillators is described by a family of asymmetric line shapes.

In Section 1.2.1, a classical equivalent of the Fano resonance formula (1.16) is derived from the equations of motion of the coupled oscillators. In Section 1.2.2, a damping of the characteristic asymmetric Fano line shape is observed for non-conservative systems and a generalization of Fano formula is derived for this case.

### 1.2.1 Classical equivalent of Fano resonance formula

Let us consider a system of oscillators B and D with respective resonance frequency  $\omega_b$  and  $\omega_d$  [Fig. 1.3]. The oscillator B is driven by a harmonic external force with amplitude  $f e^{i\omega t}$ . The energy transfer from the oscillator B to an external channel is modeled by the damping constant  $\gamma_b$ . The two oscillators are coupled together by a spring with real coupling constant  $g$ . The equations of motion for this system are:

$$\ddot{x}_b + \gamma_b \dot{x}_b + \omega_b^2 x_b + g x_d = f e^{i\omega t} \quad (1.33)$$

$$\ddot{x}_d + \omega_d^2 x_d + g x_b = 0. \quad (1.34)$$

An harmonic response for the displacement  $x_b$  and  $x_d$  of the oscillators is assumed.  $x_b = c_b e^{i\omega t}$  and  $x_d = c_d e^{i\omega t}$ . The amplitude of the spectral response of the oscillator B is given by:

$$c_b = \frac{\omega_d^2 - \omega^2}{(\omega_b^2 + i\gamma_b\omega - \omega^2)(\omega_d^2 - \omega^2) - g^2} f. \quad (1.35)$$

Around the frequency of the oscillator D, the two oscillators interfere destructively and constructively, giving rise to an asymmetric resonance.

We now consider the case of a general system replacing the oscillator B. The operator  $\mathcal{L}$  is a linear differential operator containing first and second order time derivatives of the displacement  $x_b$ . The equations of motion of this general system are:

$$\mathcal{L}x_b + g x_d = f(t) \quad (1.36)$$

$$\ddot{x}_d + \omega_d^2 x_d + g x_b = 0. \quad (1.37)$$

Taking the Fourier transform of Eq. (1.36) yields:

$$\mathcal{L}_\omega c_b + g c_d = \hat{f} \quad (1.38)$$

$$(\omega_d^2 - \omega^2) c_d + g c_b = 0, \quad (1.39)$$

where  $c_b(\omega)$ ,  $c_d(\omega)$  and  $\hat{f}(\omega)$  are the Fourier components of the displacement  $x_b(t)$ ,  $x_d(t)$

and the force  $f(t)$ , respectively. The dependencies in  $\omega$  are dropped in the following. From Eq. (1.38), the amplitude  $c_b$  is given by:

$$c_b = \frac{\omega_d^2 - \omega^2}{\mathcal{L}_\omega(\omega_d^2 - \omega^2) - g^2} \hat{f}. \quad (1.40)$$

We now assume that  $\mathcal{L}_\omega$  is slowly varying in a frequency interval around  $\omega_d$  and can be evaluated at  $\omega_d$ , and as such define  $\mathcal{L}_d \equiv \mathcal{L}_\omega(\omega_d)$ . Equation (1.40) is rewritten as:

$$c_b \simeq \frac{\omega_d^2 - \omega^2}{\mathcal{L}_d(\omega_d^2 - \omega^2) - g^2} \hat{f}. \quad (1.41)$$

Around the frequency resonance  $\omega_d$  of the oscillator D, energy is resonantly transferred between the two systems. This transfer occurs at a frequency that is shifted from  $\omega_d$  by:

$$\Delta = -\frac{g^2}{|\mathcal{L}_d|^2} \frac{\text{Re}(\mathcal{L}_d)}{\omega_d}, \quad (1.42)$$

and has a spectral width of:

$$\Gamma = \frac{g^2}{|\mathcal{L}_d|^2} \text{Im}(\mathcal{L}_d). \quad (1.43)$$

The reduced frequency  $\kappa$  is defined by  $\kappa = (\omega^2 - \omega_d^2 - \omega_d \Delta)/\Gamma$ . The relative phase between the two systems depends on the frequency. As the oscillator D is subject to a frequency shift of  $\pi$  around the resonance frequency, its phase difference with the system B induces a destructive or constructive interference, and an asymmetric line shape is observed in the response  $c_b$  of system B. From Eq. (1.41), it is given by (Appendix A):

$$|c_b|^2 = \frac{|\hat{f}|^2}{|\mathcal{L}_\omega|^2} \sigma_f. \quad (1.44)$$

where  $\sigma_f$  the classical equivalent of Fano formula around the resonance frequency of the oscillator D:

$$\sigma_f = \frac{(\kappa + q)^2}{\kappa^2 + 1}. \quad (1.45)$$

The parameter  $q$  describes the degree of asymmetry of the line shape:  $q = -\text{Re}(\mathcal{L}_d)/\text{Im}(\mathcal{L}_d)$ . For  $\kappa = -q$ , the destructive interference leads to complete vanishing of  $|c_b|^2$ . Equation (1.44) is valid if the complex amplitude of the oscillator B does not strongly vary within the Fano resonance frequency interval. In such a condition, the agreement between Eq. (1.35) and Eq. (1.44) is perfect (Fig. 1.4). The response of the oscillator D around its resonance frequency normalized to the response of the uncoupled system B is derived



## 1.2. Equivalent model of two coupled classical oscillators

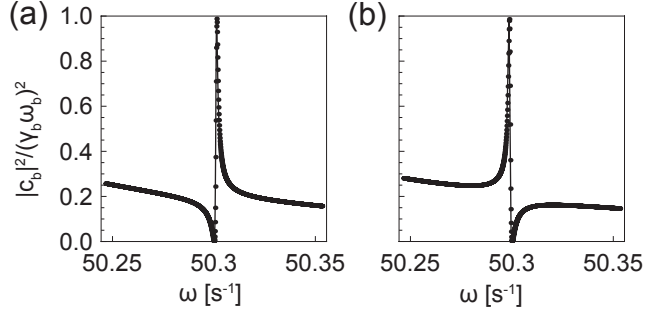


Figure 1.4: Amplitude of the forced oscillator as a function of the excitation frequency for (a) a real coupling constant  $g = 2.00 \text{ s}^{-2}$  and (b) an imaginary coupling constant  $g = 2.00i \text{ s}^{-2}$  (with  $\omega_b = 50.00 \text{ s}^{-1}$ ,  $\omega_d = 50.30 \text{ s}^{-1}$  and  $\gamma_b = 0.30 \text{ s}^{-1}$ ). Dots: calculated directly from Eq. (1.35) ; solid line: calculated from Eq. (1.44).

from Eq. (1.39) (Appendix A):

$$|c_d|^2 \frac{|\mathcal{L}_d|^2}{|\hat{f}|^2} = \frac{|\mathcal{L}_d|^4}{|g|^2 \text{Im}^2(\mathcal{L}_d)} \frac{1}{\kappa^2 + 1}. \quad (1.46)$$

Its line shape is a symmetric Lorentzian whose amplitude and width are controlled by the coupling between the two systems. As the coupling decreases, the energy transferred from system B to the oscillator D is stored longer and its amplitude increases. If the system B is an oscillator, we have  $\mathcal{L}_\omega = \omega_b^2 - \omega^2 + i\gamma_b\omega$  and  $\mathcal{L}_d = \omega_b^2 - \omega_d^2 + i\gamma_b\omega_d$ . The resonance parameters become

$$\Delta = \frac{g^2}{|\mathcal{L}_d|^2} \frac{(\omega_d^2 - \omega_b^2)}{\omega_d}, \quad \Gamma = \frac{g^2}{|\mathcal{L}_d|^2} \gamma_b \omega_d, \quad q = \frac{\omega_d^2 - \omega_b^2}{\gamma_b \omega_d}. \quad (1.47)$$

In the case of a purely imaginary coupling constant  $g = ig'$ , Eq. (1.41) becomes:

$$c_b \simeq \frac{\omega_d^2 - \omega^2}{\mathcal{L}_d(\omega_d^2 - \omega^2) + g'^2} f. \quad (1.48)$$

A physically meaningful response of the system requires that the resonance has a positive width. As a result, the resonance frequency shift and asymmetry parameter reverse their sign for a purely imaginary coupling:

$$q = \frac{\omega_b^2 - \omega_d^2}{\gamma_b \omega_d}, \quad \Delta = \frac{g'^2}{|\mathcal{L}_d|^2} \frac{(\omega_b^2 - \omega_d^2)}{\omega_d}. \quad (1.49)$$

These results imply in particular that if a  $\pi/2$  phase retardation is introduced in the oscillators coupling, the conditions of destructive and constructive interference are reversed (Fig. 1.4). In electromagnetic scattering theory, these conditions are determined by the relative phase between the resonant mode and the continuum (Fig. 1.2).

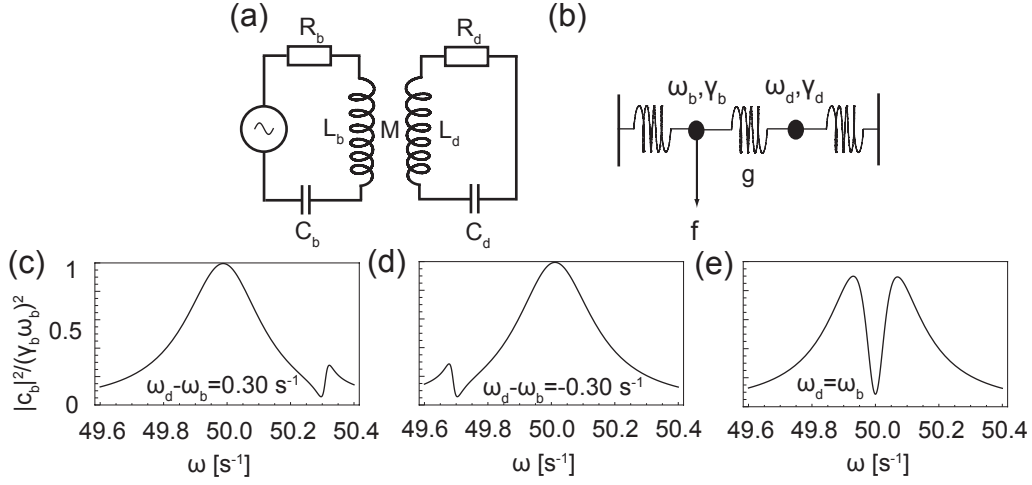


Figure 1.5: Fano resonance in non-conservative systems. (a) A resistance  $R_d$  is added to the LC circuit. (b) A damping constant  $\gamma_d$  is added to the oscillator D. (c-e) Amplitude of the forced oscillator as a function of the excitation frequency for different values of detuning  $\omega_d - \omega_b$  (with  $\omega_b = 50.00 \text{ s}^{-1}$ ,  $g = 6.00 \text{ s}^{-2}$ ,  $\gamma_b = 0.30 \text{ s}^{-1}$  and  $\gamma_d = 0.02 \text{ s}^{-1}$ ).

### 1.2.2 Generalized Fano resonance formula

Alzar [28] and Joe [29] discussed the two oscillators systems with a damping constant  $\gamma_d$  added to the oscillator D (Fig. 1.5) but did not derive a resonance formula for these systems around the resonance frequency  $\omega_d$ . In this section, I will derive a generalized Fano resonance formula for non-conservative systems. The equations of motion for the system in Fig. 1.5 are:

$$\ddot{x}_b + \gamma_b \dot{x}_b + \omega_b^2 x_b + g x_d = f e^{i\omega t} \quad (1.50)$$

$$\ddot{x}_d + \gamma_d \dot{x}_d + \omega_d^2 x_d + g x_b = 0. \quad (1.51)$$

The amplitude of the response of the oscillator B is given by:

$$c_b = \frac{\omega_d^2 + i\gamma_d \omega - \omega^2}{(\omega_b^2 + i\gamma_b \omega - \omega^2)(\omega_d^2 + i\gamma_d \omega - \omega^2) - g^2} f. \quad (1.52)$$

We now consider the case of a general system replacing the oscillator B. The operator  $\mathcal{L}$  is a linear differential operator containing first and second order time derivatives of the displacement  $x_b$ . The equations of motion of this general system are:

$$\mathcal{L}x_b + g x_d = f \quad (1.53)$$

$$\ddot{x}_d + i\gamma_d \dot{x}_d + \omega_d^2 x_d + g x_b = 0. \quad (1.54)$$

## 1.2. Equivalent model of two coupled classical oscillators

---

Taking the Fourier transform of Eq. (1.53) yields:

$$\mathcal{L}_\omega c_b + g c_d = \hat{f} \quad (1.55)$$

$$(\omega_d^2 + i\gamma_d\omega - \omega^2)c_d + g c_b = 0, \quad (1.56)$$

where  $c_b(\omega)$ ,  $c_d(\omega)$  and  $\hat{f}(\omega)$  are the Fourier components of the displacement  $x_b(t)$ ,  $x_d(t)$  and the force  $f(t)$ , respectively. The dependencies in  $\omega$  are dropped in the following. The amplitude of the response of system B is written as:

$$c_b \simeq \frac{\omega_d^2 + i\gamma_d\omega - \omega^2}{\mathcal{L}_d(\omega_d^2 + i\gamma_d\omega - \omega^2) - g^2} \hat{f}. \quad (1.57)$$

The resonance width is the sum of two contributions  $\Gamma_i = \gamma_d\omega_d$  from intrinsic losses and  $\Gamma_c = g^2 \text{Im}(\mathcal{L}_d)/|\mathcal{L}_d|^2$  from the coupling between the oscillator D and the system B:

$$\Gamma = \Gamma_i + \Gamma_c. \quad (1.58)$$

The asymmetry parameter depends now on the ratio between these two contributions:

$$q = -\frac{\text{Re}(\mathcal{L}_d)}{\text{Im}(\mathcal{L}_d)(1 + \Gamma_i/\Gamma_c)}, \quad (1.59)$$

From Eq. (1.57), we derive the response of the oscillator B as a function of frequency (Appendix A):

$$|c_b|^2 = \frac{|\hat{f}|^2}{|\mathcal{L}_d|^2} \sigma_a, \quad (1.60)$$

where  $\sigma_a$  is the generalization of Fano formula for two non-conservative systems:

$$\sigma_a = \frac{(\kappa + q)^2 + b}{\kappa^2 + 1}, \quad (1.61)$$

where the parameter  $b$  describes the modulation damping by losses in the oscillator D and is a function of the ratio  $\Gamma_i/\Gamma_c$ :

$$b = \frac{\Gamma_i^2}{(\Gamma_c + \Gamma_i)^2}. \quad (1.62)$$

The response of the oscillator D around its resonance frequency is derived from Eq. (1.56) and normalized to the response of the uncoupled system B (Appendix A):

$$|c_d|^2 \frac{|\mathcal{L}_d|^2}{|\hat{f}|^2} = \frac{|\mathcal{L}_d|^2 \Gamma_c}{\text{Im}(\mathcal{L}_d)^2 (\Gamma_c + \Gamma_i)^2} \frac{1}{\kappa^2 + 1}. \quad (1.63)$$

As the coupling decreases, the intensity  $|c_d|^2$  reaches a maximum value for  $\Gamma_c = \Gamma_i$ . As the coupling decreases, the energy is stored longer in the oscillator D but is subject to

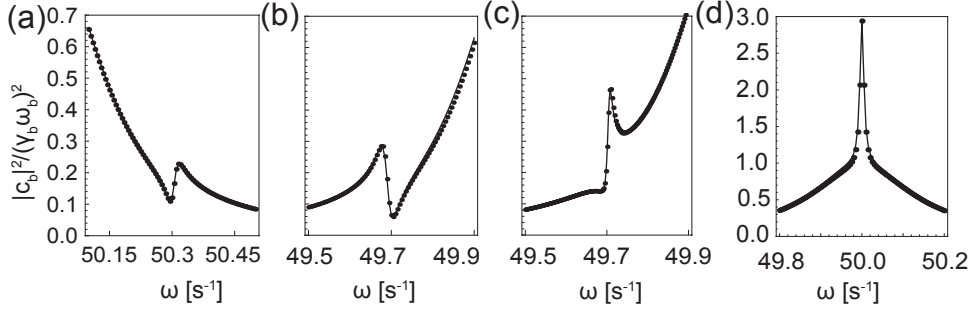


Figure 1.6: Amplitude of the forced oscillator as a function of the excitation frequency for (a)  $g = 4.00 \text{ s}^{-2}$  and  $\omega_d = 50.30 \text{ s}^{-1}$ , (b)  $g = 6.00 \text{ s}^{-2}$  and  $\omega_d = 49.70 \text{ s}^{-1}$ , (c)  $g = 4.00i \text{ s}^{-2}$  and  $\omega_d = 49.70 \text{ s}^{-1}$ , (d)  $g = 2.50i \text{ s}^{-2}$  and  $\omega_d = 50.00 \text{ s}^{-1}$  (with  $\omega_b = 50.00 \text{ s}^{-1}$ ,  $\gamma_b = 0.30 \text{ s}^{-1}$  and  $\gamma_d = 0.02 \text{ s}^{-1}$ ). Dots: calculated directly from Eq. (1.52) ; solid line: calculated from Eq. (1.60).

stronger damping, so that its intensity vanishes. For the case of two coupled oscillators,  $\mathcal{L}_\omega = \omega_b^2 - \omega^2 + i\gamma_b\omega$  and  $\mathcal{L}_d = \omega_b^2 - \omega_d^2 + i\gamma_b\omega_d$ . The resonance parameters then become:

$$\Gamma_c = \frac{g^2\gamma_b\omega_d}{|\mathcal{L}_d|^2}, \quad q = \frac{\omega_d^2 - \omega_b^2}{\omega_d\gamma_b(1 + \Gamma_i/\Gamma_c)}. \quad (1.64)$$

Equation (1.60) is valid if the complex amplitude of the oscillator B does not strongly vary within the Fano resonance frequency interval. In such conditions, the agreement between Eq. (1.52) and Eq. (1.60) is perfect (Fig. 1.6). In the case of a purely imaginary coupling constant  $g = ig'$ , Eq. (1.57) becomes:

$$c_b \simeq \frac{\omega_d^2 + i\gamma_d\omega - \omega^2}{\mathcal{L}_d(\omega_d^2 + i\gamma_d\omega - \omega^2) + g'^2} f. \quad (1.65)$$

A physically meaningful response of the system requires that the resonance has a positive width. The resonance parameters are

$$\Gamma_c = -\frac{g'^2\gamma_b\omega_d}{|\mathcal{L}_d|^2}, \quad q = \frac{\omega_b^2 - \omega_d^2}{\omega_d\gamma_b(1 + \Gamma_i/\Gamma_c)}, \quad \Delta = \frac{g'^2(\omega_b^2 - \omega_d^2)}{|\mathcal{L}_d|^2\omega_d}. \quad (1.66)$$

This results implies in particular that if a  $\pi/2$  phase retardation is introduced in the oscillators coupling, the conditions for destructive and constructive interference are reversed (Fig. 1.6). In electromagnetic scattering theory, these conditions are determined by the relative phase between the resonant mode and the continuum (Fig. 1.2). In addition, the sign of  $\Gamma_c$  becomes negative and the parameter  $b$  can reach values superior to 1 [Fig. 1.6(d)]. This situation of superscattering [51], which requires the presence of intrinsic losses, has also been called the classical equivalent of electromagnetically induced absorption [52].

## 1.3 Electromagnetic theory

In this Section, the interaction of electromagnetic radiative waves with a localized mode is investigated in the framework of Maxwell's equations. From *ab initio* calculations and using the formalism of projection operators developed by Feshbach in atomic spectroscopy [53–55], I show that the resonance spectrum can be described by a family of asymmetric curves including the contributions from intrinsic losses and derive a formula that is the generalization of Fano's formula [18] to non-conservative systems. In Section 1.3.1, the interaction of a localized mode with an arbitrary continuum is considered, followed in Section 1.3.2 by the particular case of the interaction between a localized and a radiative mode. The latter is assumed to generate a continuum of radiative waves with a Lorentzian distribution.

### 1.3.1 Dark mode and radiative waves

Let us consider the electromagnetic scattering by a dielectric or metallic object in a dielectric background. The scatterer supports a non-radiative (dark) mode interacting with a continuum of radiative waves. A harmonic time-dependence for the fields  $\mathbf{E} = \mathbf{E}_0 e^{-i\omega t}$  is assumed throughout. The relative dielectric permittivity  $\epsilon(\mathbf{r}, \omega)$  is generally complex and has frequency dispersion. The frequency dependent electric field  $\mathbf{E}$  satisfies the wave equation

$$\epsilon^{-1}(\mathbf{r}, \omega) \nabla \times \nabla \times \mathbf{E}(\mathbf{r}, \omega) - \frac{\omega^2}{c_0^2} \mathbf{E}(\mathbf{r}, \omega) = 0. \quad (1.67)$$

To simplify notation, in the following the dependence of the electric field  $\mathbf{E}$  on  $\omega$  is kept implicit. Let us assume that the scatterer permittivity is given by a Drude model with plasma frequency  $\omega_p$ ; the scaling law of Maxwell's equations allows then to scale all frequency units by  $\omega_p$  and length units by  $2\pi c_0/\omega_p$ . We introduce the generally complex and frequency dependent differential operator  $\underline{\underline{\mathcal{M}}}_\omega$  defined by

$$\underline{\underline{\mathcal{M}}}_\omega \mathbf{E}(\mathbf{r}) = \frac{c_0^2}{\epsilon(\mathbf{r}, \omega)} \nabla \times \nabla \times \mathbf{E}(\mathbf{r}). \quad (1.68)$$

The wave equation can be written for a vectorial wave function  $|\mathbf{E}\rangle$

$$(\underline{\underline{\mathcal{M}}}_\omega - \omega^2 \mathbf{I})|\mathbf{E}\rangle = 0, \quad (1.69)$$

where  $\mathbf{I}$  is the identity operator. The inner product is defined by

$$\langle \mathbf{E}_1 | \mathbf{E}_2 \rangle = \int \mathbf{E}_1^*(\mathbf{r}) \cdot \mathbf{E}_2(\mathbf{r}) d^3\mathbf{r}. \quad (1.70)$$

### Feshbach formalism of projection operators

Following Feshbach, Bhatia and Temkin, we introduce the orthogonal projection operators  $P$  and  $Q$  splitting the wave function into a radiative (bright) and a non-radiative (dark) parts [53, 55]. Any wave function  $|\mathbf{E}\rangle$  can be decomposed as  $|\mathbf{E}\rangle = Q|\mathbf{E}\rangle + P|\mathbf{E}\rangle$  where only  $P|\mathbf{E}\rangle$  satisfies the radiation condition. Equation (1.69) becomes

$$(\underline{\underline{\mathcal{M}}}_\omega - \omega^2 \mathbb{I})(Q|\mathbf{E}\rangle + P|\mathbf{E}\rangle) = 0, \quad (1.71)$$

yielding the two coupled equations:

$$(Q\underline{\underline{\mathcal{M}}}_\omega Q - \omega^2 \mathbb{I})Q|\mathbf{E}\rangle = -Q\underline{\underline{\mathcal{M}}}_\omega P|\mathbf{E}\rangle \quad (1.72)$$

$$(P\underline{\underline{\mathcal{M}}}_\omega P - \omega^2 \mathbb{I})P|\mathbf{E}\rangle = -P\underline{\underline{\mathcal{M}}}_\omega Q|\mathbf{E}\rangle. \quad (1.73)$$

We consider a unique non-radiative mode  $|\mathbf{E}_d\rangle$ , defined to be eigenfunction of the projector to non-radiative modes  $Q|\mathbf{E}_d\rangle = |\mathbf{E}_d\rangle$ , and to satisfy  $Q\underline{\underline{\mathcal{M}}}_{\omega_d} Q|\mathbf{E}_d\rangle = z_d^2 |\mathbf{E}_d\rangle$  and  $|\langle \mathbf{E}_d | \mathbf{E}_d \rangle|^2 = 1$ . Taking material losses into account, the quantity  $z_d = \omega_d + i\gamma_d$  is generally complex. Its real part  $\omega_d$  is the mode resonance frequency, and  $\gamma_d$  its intrinsic damping. The system is studied in the vicinity of the resonance frequency  $\omega_d$ . In this frequency range, we assume that the space of eigenfunctions of  $Q$  is spanned by  $|\mathbf{E}_d\rangle$  only, so that [54]

$$Q = |\mathbf{E}_d\rangle \langle \mathbf{E}_d|. \quad (1.74)$$

Equation (1.72) can be written in  $Q$ -space as:

$$Q|\mathbf{E}\rangle = \frac{1}{\omega^2 - z_d^2} |\mathbf{E}_d\rangle \langle \mathbf{E}_d | \underline{\underline{\mathcal{M}}}_\omega P|\mathbf{E}\rangle. \quad (1.75)$$

Inserting Eq. (1.75) into Eq. (1.73), a wave equation with source is obtained for  $P|\mathbf{E}\rangle$ :

$$(P\underline{\underline{\mathcal{M}}}_\omega P - \omega^2 \mathbb{I})P|\mathbf{E}\rangle = \frac{1}{z_d^2 - \omega^2} P\underline{\underline{\mathcal{M}}}_\omega |\mathbf{E}_d\rangle \langle \mathbf{E}_d | \underline{\underline{\mathcal{M}}}_\omega P|\mathbf{E}\rangle. \quad (1.76)$$

The radiative wavefunction  $|P\mathbf{E}_b\rangle$  is defined to satisfy Eq. (1.76) in the absence of the localized mode  $|\mathbf{E}_d\rangle$ . From its definition,  $|P\mathbf{E}_b\rangle$  satisfies the following homogeneous equation:

$$(P\underline{\underline{\mathcal{M}}}_\omega P - \omega^2 \mathbb{I})|P\mathbf{E}_b\rangle = 0. \quad (1.77)$$

Equation (1.76) can be solved using the Green's dyadic  $\underline{\underline{G}}_b$  of Eq. (1.77):

$$P|\tilde{\mathbf{E}}\rangle = P|\mathbf{E}_b\rangle + \frac{\langle \mathbf{E}_d | \underline{\underline{\mathcal{M}}}_\omega P|\tilde{\mathbf{E}}\rangle}{z_d^2 - \omega^2} \underline{\underline{G}}_b P\underline{\underline{\mathcal{M}}}_\omega |\mathbf{E}_d\rangle. \quad (1.78)$$

In Eq. (1.78), the wavefunction  $|\tilde{\mathbf{E}}\rangle$  is related to  $|\mathbf{E}\rangle$  but does not have the same asymptotic behavior; an expression for  $|\mathbf{E}\rangle$  is derived later. Multiplying Eq. (1.78) on the left by  $\langle \mathbf{E}_d | \underline{\mathcal{M}}_\omega$  and replacing  $\langle \mathbf{E}_d | \underline{\mathcal{M}}_\omega P | \tilde{\mathbf{E}} \rangle$  in Eq. (1.78) yields:

$$P|\tilde{\mathbf{E}}\rangle = |P\mathbf{E}_b\rangle + \frac{\langle \mathbf{E}_d | \underline{\mathcal{M}}_\omega | P\mathbf{E}_b \rangle}{\omega_d^2 + 2i\gamma_d\omega_d - \omega^2 + \omega_d\Delta} \underline{G}_b P \underline{\mathcal{M}}_\omega |\mathbf{E}_d\rangle, \quad (1.79)$$

where

$$\Delta = \frac{1}{\omega_d} \left( \gamma_d^2 - \langle \mathbf{E}_d | \underline{\mathcal{M}}_\omega P \underline{G}_b P \underline{\mathcal{M}}_\omega | \mathbf{E}_d \rangle \right) \quad (1.80)$$

is the shift in the resonance position  $\omega_d$  due to the field overlap between the continuum  $|P\mathbf{E}_b\rangle$  and  $|\mathbf{E}_d\rangle$ . Using Eqs. (1.75) and (1.79), we have a final expression for  $|\tilde{\mathbf{E}}\rangle$ :

$$|\tilde{\mathbf{E}}\rangle = |P\mathbf{E}_b\rangle + \frac{\langle \mathbf{E}_d | \underline{\mathcal{M}}_\omega | P\mathbf{E}_b \rangle}{\omega_d^2 + 2i\gamma_d\omega_d - \omega^2 + \omega_d\Delta} (\underline{G}_b P \underline{\mathcal{M}}_\omega |\mathbf{E}_d\rangle - |\mathbf{E}_d\rangle). \quad (1.81)$$

The wavefunction  $|\mathbf{E}\rangle$  must have the same norm as  $P|\mathbf{E}_b\rangle$  in the far-field (i.e.  $|P|\mathbf{E}\rangle|^2 = |P|\mathbf{E}_b\rangle|^2$ ). The asymptotic behavior of  $|P\tilde{\mathbf{E}}\rangle$  is now compared to  $|P\mathbf{E}_b\rangle$ , leading to a relation between  $|\tilde{\mathbf{E}}\rangle$  and  $|\mathbf{E}\rangle$ .

### Asymptotic behaviour

Most plasmonic nanostructures and metamaterials are embedded in a dielectric medium, allowing us to assume that the permittivity is real, homogeneous and non dispersive in the radiative region, and therefore that  $P\underline{\mathcal{M}}_\omega$  is self-adjoint and frequency-independent. For a non-homogeneous background medium, this operator is not self-adjoint, which can have an incidence on the final resonance formula. The set of solutions  $|P\mathbf{E}_b(\omega)\rangle$  of Eq. (1.77) forms an orthogonal basis of modes:

$$\langle P\mathbf{E}_b(\omega) | P\mathbf{E}_b(\omega') \rangle = e^{i\phi(\omega)} \delta(\omega' - \omega), \quad (1.82)$$

where  $\phi(\omega)$  determines the phase difference between a radiative wave  $|P\mathbf{E}_b(\omega)\rangle$  and its reciprocal. For simplicity, the phase difference  $\phi$  is assumed frequency-independent and evaluated at the resonance frequency  $\omega_d$ . This choice of radiative boundary conditions has an impact on the asymmetry of the observed resonance line shape (Fig. 1.2). The Green's function  $\underline{G}_b$  of Eq. (1.77) satisfies:

$$(P\underline{\mathcal{M}}_\omega P - \omega^2 \mathbf{I}) \underline{G}_b = \mathbf{I}. \quad (1.83)$$

The general solution  $|\mathbf{P}\mathbf{E}\rangle$  of Eq. (1.77) with current:

$$(P\underline{\mathcal{M}}_\omega P - \omega^2 \mathbf{I}) |\mathbf{P}\mathbf{E}\rangle = |\mathbf{J}\rangle, \quad (1.84)$$

can be decomposed into solutions of the homogeneous equation:

$$|P\mathbf{E}\rangle = \frac{1}{\pi} \int d\omega' a_{\omega'} |P\mathbf{E}_b(\omega')\rangle. \quad (1.85)$$

Inserting Eq. (1.85) into Eq. (1.84) leads to the definition of the action of the Green's function on a solution of Eq. (1.78):

$$|P\mathbf{E}\rangle = \frac{e^{i\phi}}{\pi} \mathcal{P} \int d\omega' \frac{\langle P\mathbf{E}_b(\omega') | \mathbf{J} \rangle |P\mathbf{E}_b(\omega')\rangle}{\omega'^2 - \omega^2} \quad (1.86)$$

$$\equiv \underline{\underline{G}}_b | \mathbf{J} \rangle. \quad (1.87)$$

For the sake of simplicity, the prefactor  $e^{i\phi}$  will be assumed to be equal to 1 in the following. We define  $\Gamma_i = 2\omega_d\gamma_d$  and  $\Gamma_c = |\langle \mathbf{E}_d | \underline{\underline{M}}_\omega | P\mathbf{E}_b \rangle|^2 / (2\omega_d)$ , and the centered frequency  $\chi = \omega^2 - \omega_d^2 - \omega_d\Delta$ . Using the expression for the Green's function [Eq. (1.86)], Equation (1.81) has the following asymptotic behaviour:

$$\lim_{|\mathbf{r}| \rightarrow \infty} P\tilde{\mathbf{E}}(\mathbf{r}) = \lim_{|\mathbf{r}| \rightarrow \infty} P\tilde{\mathbf{E}}_b(\mathbf{r}) \left[ 1 - \frac{\Gamma_c}{\chi - \Gamma_i i} \right] \quad (1.88)$$

$$= \lim_{|\mathbf{r}| \rightarrow \infty} P\tilde{\mathbf{E}}_b(\mathbf{r}) [f(\chi) - g(\chi)i]. \quad (1.89)$$

where the functions  $f$  and  $g$  of the centered frequency are given by:

$$f(\chi) = \frac{\chi^2 + \Gamma_i^2 + \Gamma_c\Gamma_i}{\chi^2 + \Gamma_i^2}, \quad g(\chi) = \frac{\Gamma_i\chi}{\chi^2 + \Gamma_i^2}. \quad (1.90)$$

The function  $f$  that is constantly equal to 1 if  $\gamma_d = 0$  accounts for the modulation depth by intrinsic losses. The total field  $P\tilde{\mathbf{E}}(\mathbf{r})$  also undergoes a rapid  $\sim \pi$  phase shift in a frequency region around  $\chi = 0$ . In order for  $|P\mathbf{E}\rangle$  to have the same norm as  $|P\tilde{\mathbf{E}}\rangle$ , they must be related by

$$|\mathbf{E}\rangle = f^{-1}(\chi) \sqrt{\frac{\xi^2}{\xi^2 + 1}} |\tilde{\mathbf{E}}\rangle, \quad (1.91)$$

where

$$\xi = \frac{\chi^2 + \Gamma_i^2 + \Gamma_c\Gamma_i}{\Gamma_c\chi}. \quad (1.92)$$

In the absence of intrinsic losses, the quantity  $\xi$  becomes the scaled frequency  $\chi/\Gamma_c = (\omega^2 - \omega_d^2 - \omega_d\Delta)/\Gamma_c$ .

### Line shape

We now consider a transition operator  $T$  from an initial state  $|g\rangle$  to a final state  $|\tilde{\mathbf{E}}\rangle$ , which can be interpreted as the response of an optical system to an external excitation,



such as the Local Density of States (LDOS) [56], the forward scattering cross-section [57] or the reflectance of a two-dimensional array. From Eq. (1.81):

$$\frac{\langle g|T|\tilde{\mathbf{E}}\rangle}{\langle g|T|P\mathbf{E}_b\rangle} = 1 - \frac{\Gamma_c}{\Gamma_i i - \chi} q', \quad (1.93)$$

with

$$q' = 2\omega \frac{\langle g|T|\mathbf{E}_d\rangle - \langle g|T\underline{G}_b P \underline{M}_\omega|\mathbf{E}_d\rangle}{(\langle \mathbf{E}_d|\underline{M}_\omega|P\mathbf{E}_b\rangle)^* \langle g|T|P\mathbf{E}_b\rangle}. \quad (1.94)$$

The parameter  $q$  is given by the ratio between the optical response of the perturbed non-radiative mode and the continuum. Assuming  $q$  is real, one gets from Eqs. (1.91) and (1.93) the ratio of the optical response of the total field  $|\mathbf{E}\rangle$  to the one of the continuum  $|P\mathbf{E}_b\rangle$ :

$$\frac{|\langle g|T|\mathbf{E}\rangle|^2}{|\langle g|T|P\mathbf{E}_b\rangle|^2} = \frac{(\chi^2 + \Gamma_i^2 + \Gamma_c \chi q')^2 + \Gamma_c^2 \Gamma_i^2 q'^2}{(\chi^2 + \Gamma_i^2 + \Gamma_c \Gamma_i)^2 + \Gamma_c^2 \chi^2}, \quad (1.95)$$

The resonance width is given by:

$$\Gamma = \Gamma_c + \Gamma_i, \quad (1.96)$$

meaning that it is the sum of two contributions, from intrinsic losses  $\Gamma_i$  and from the coupling to the radiative continuum  $\Gamma_c$ . The reduced frequency is defined by  $\kappa = \chi/\Gamma$ . From Eq. (1.95), some algebraic manipulations lead to (Appendix A):

$$\sigma_a(\kappa) = \frac{|\langle g|T|\mathbf{E}\rangle|^2}{|\langle g|T|P\mathbf{E}_b\rangle|^2} = \frac{(\kappa + q)^2 + b}{\kappa^2 + 1}, \quad (1.97)$$

with the asymmetry parameter

$$q = \frac{q'}{1 + \Gamma_i/\Gamma_c}, \quad (1.98)$$

and the modulation damping parameter

$$b = \frac{\Gamma_i^2/\Gamma_c^2}{(1 + \Gamma_i/\Gamma_c)^2}. \quad (1.99)$$

Equation (1.97) is the electromagnetic equivalent of Eq. (1.61). Its line shape as a function of the reduced frequency is shown in Fig. 1.7(b) and (c). Finally, using Eqs. (1.81) and (1.91), it can be shown that the amplitude of the field in the  $Q$ -zone (i.e. non-radiative zone) satisfies (Appendix A):

$$|\langle \mathbf{E}|Q|\mathbf{E}\rangle|^2 = \frac{1}{\kappa^2 + 1} \frac{|\langle \mathbf{E}_d|\underline{M}_\omega|P\mathbf{E}_b\rangle|^2}{(\Gamma_c + \Gamma_i)^2}. \quad (1.100)$$

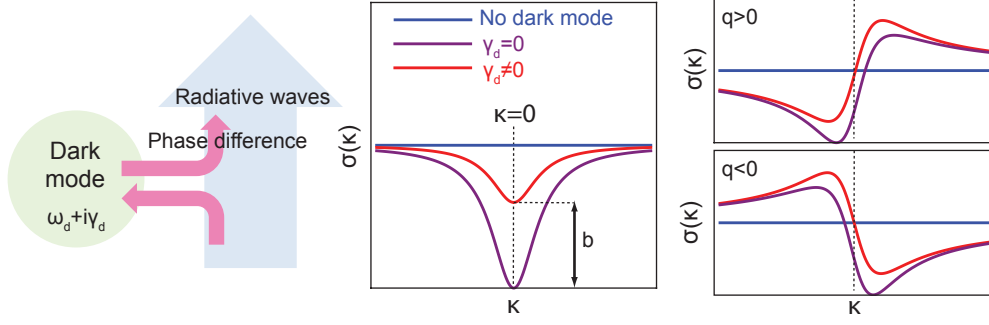


Figure 1.7: Resonance shape function  $\sigma$  as a function of the reduced frequency  $\kappa = (\omega^2 - \omega_d^2 - \omega_d \Delta) / \Gamma$  for different values of the asymmetry parameter  $q$  and the modulation damping parameter  $b$  [Eq. (1.97)].

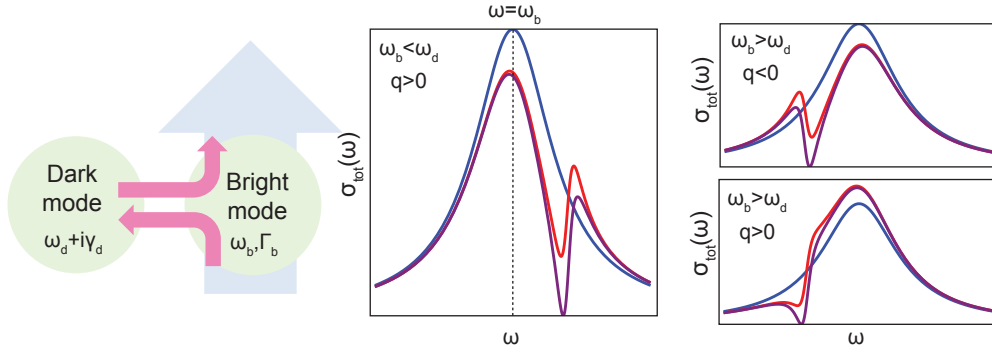


Figure 1.8: Particular case of Fano interference for which the continuum of radiative waves is generated by a bright mode. The continuum has a Lorentzian distribution of the frequency.

It is a Lorentzian of width  $\Gamma$  centered on  $\kappa = 0$  with amplitude proportional to  $\Gamma_c / (\Gamma_c + \Gamma_i)$ . As the coupling decreases, the localized mode contribution increases because it is able to store longer the electromagnetic energy. This contribution reaches a maximum value for  $\Gamma_c = \Gamma_i$  and goes to 0 for smaller  $\Gamma_c$  because the localized mode is subject to stronger damping by losses in the metallic structure.

### 1.3.2 Dark mode and bright mode

The case of the interaction between a localized (dark) mode and a radiative (bright) mode is now discussed. The bright mode is assumed to generate a continuum of radiative waves  $|P\mathbf{E}_b\rangle$  with the following pseudo-Lorentzian distribution:

$$|P\mathbf{E}_b(\omega)\rangle = \frac{\Gamma_b |P\mathbf{E}_b(\omega_b)\rangle}{\omega^2 - \omega_b^2 + i\Gamma_b}, \quad (1.101)$$

where  $\omega_b$  is the frequency of highest amplitude and  $\Gamma_b$  the width of the distribution. In this particular case, each resonance parameter in Eq. (1.97) has a closed-form expression. It is assumed that all the parameters are independent of the frequency in a spectral region around the resonance, and can be evaluated at  $\omega_d$ . From Eqs. (1.86) and (1.79), the Fano resonance frequency shift from  $\omega_d$  is given by the following integral:

$$\Delta = \frac{\gamma_d^2}{\omega_d} - \frac{1}{\pi\omega_d} \mathcal{P} \int d\omega' \frac{|\langle P\mathbf{E}_b(\omega') | \underline{\mathcal{M}} | \mathbf{E}_d \rangle|^2}{\omega'^2 - \omega_d^2} \quad (1.102)$$

$$= \frac{\gamma_d^2}{\omega_d} - \frac{|\langle P\mathbf{E}_b(\omega_s) | \underline{\mathcal{M}} | \mathbf{E}_d \rangle|^2}{\pi\omega_d} \mathcal{I}, \quad (1.103)$$

where

$$\mathcal{I} = \Gamma_b^2 \mathcal{P} \int \frac{d\omega'}{(\omega'^2 - \omega_d^2)[(\omega'^2 - \omega_b^2)^2 + \Gamma_b^2]}, \quad (1.104)$$

and  $\omega_s$  is the bright mode resonance frequency and  $\Gamma_s$  its resonance width. In order to calculate the integral  $\mathcal{I}$ , we assume that  $\omega'$  is a complex variable. The integration path in the complex plane is a closed path following the real axis and half a circle with infinite radius on the lower complex plane, including poles at  $\sqrt{\omega_b^2 + i\Gamma_b}$  and  $\omega_d$ . Using the residue theorem, one obtains:

$$\mathcal{I} \simeq \frac{\pi\Gamma_b}{2\omega_d} \frac{\omega_b^2 - \omega_d^2}{(\omega_d^2 - \omega_b^2)^2 + \Gamma_b^2}. \quad (1.105)$$

We define the reduced coupling constant by:

$$G = \frac{|\langle P\mathbf{E}_b(\omega_b) | \underline{\mathcal{M}} | \mathbf{E}_d \rangle|^2 \Gamma_b}{\omega_d [(\omega_d^2 - \omega_b^2)^2 + \Gamma_b^2]}. \quad (1.106)$$

Therefore,

$$\Delta = \frac{\gamma_d^2}{\omega_d} + G \frac{\omega_d^2 - \omega_b^2}{2\omega_d}. \quad (1.107)$$

The sign of  $\Delta$  is determined by the frequency difference between the two modes, and its magnitude linearly depends on the coupling strength, which is a signature of weak coupling.

The contribution of the coupling to the resonance width becomes  $\Gamma_c = \Gamma_b G/2$ , and the asymmetry parameter (for  $\langle g|T|\mathbf{E}_d \rangle = 0$  in the far-field):

$$q = \frac{\omega_d^2 - \omega_b^2}{2\Gamma_b(1 + \Gamma_i/\Gamma_c)}. \quad (1.108)$$

The response of the total system is the product between the bright mode response and

the asymmetric line shape of Eq. (1.97):

$$\sigma_{\text{tot}}(\omega) = \frac{\Gamma_b^2}{(\omega^2 - \omega_b^2) + \Gamma_b^2} \frac{(\kappa + q)^2 + b}{\kappa^2 + 1}. \quad (1.109)$$

This line shape is shown in Fig. 1.8 for several values of the modes detuning and asymmetry parameter. It has been assumed from Eq. (1.86) that the phase difference between a radiative wave and its reciprocal satisfies  $\phi = 0$ . If  $\phi = \pi$ , the asymmetry parameter reverses its sign:

$$q = \frac{\omega_b^2 - \omega_d^2}{2\Gamma_b(1 + \Gamma_i/\Gamma_c)}. \quad (1.110)$$

Let us finally mention that a correspondence between the expressions for the resonance parameters in this section can be found with those of the resonance parameters in the oscillators system described in Section 1.2.2.

## 1.4 Conclusion

In this chapter, the fundamental properties of Fano resonances in plasmonic nanostructures, and more generally in non-conservative systems, have been established. Fano resonances can be described as a general interference process: the interaction between a continuum of radiative waves with a localized resonant system leads to an asymmetric line shape for the total response. Since Fano's seminal work of 1961 on this phenomenon was unable to include the case of non-conservative systems, phenomenological models such as the classical analog of two coupled oscillators have been extensively used in photonics and plasmonics, in addition to providing an intuitive description. I have shown that the original Fano formula can be derived for the oscillators system, and that it can be generalized when damping is introduced in the unforced oscillator. This general line shape formula describes the behavior of coupled damped oscillators and provides an intuitive view of the main features of Fano resonances in non-conservative systems.

From Maxwell's equations and using Feshbach formalism of projection operators, the interaction between a localized mode with radiative electromagnetic waves has then been investigated. In particular, I have derived a general analytical formula for the optical response of such a system. The approach developed here overcomes the theoretical difficulty of dealing with non-hermitian operators, a characteristic feature of plasmonic systems which was not considered in Fano's original approach. Finally, the particular case of the interaction between a localized mode and a radiative mode has been discussed, and a formula for the optical response of the coupled modes system has been derived. The *ab initio* character of the approach developed here enables a general description of Fano-like phenomena in plasmonic systems.

## 2 Surface integral equation method for periodic nanostructures

The development of an original method for the electromagnetic scattering by periodic nanostructures is also one important aspect of this thesis. While the main results are published in Refs. [58] and [59], this chapter goes into greater details. Let me start by reviewing the strengths and weaknesses of existing approaches. Among the most popular methods for periodic structures, the Fourier-modal [60] and plane-wave expansion [61] methods, or the rigorous coupled-wave analysis [62], although rather straightforward to implement, are efficient only for specific types of geometries which can be decomposed into a low number of Fourier harmonics. Scattering matrix methods are well suited for calculating reflectivity or emission spectra in photonic structures [63,64]. Methods based on local formulations, such as finite-difference time-domain [65] or finite-element method (FEM) [66,67] are more flexible but do not satisfy Sommerfeld's radiation conditions. Therefore boundary conditions must be imposed at the edges of the computation window. The FEM is proven very accurate, can handle realistic structures and produces sparse matrices efficiently solved with appropriate algorithms [67]. Although the focus of the present work is on general three-dimensional (3D) periodic systems, one should mention the vast body of work developed for diffraction gratings since the early theory of Lord Rayleigh [45]: the integral and differential theories [68], the Chandezon method [69], the modal formulation [70] or methods based on finite elements [71].

Integral equation methods are multiscale and well suited for electromagnetic scattering problems, since only the discretization of the scatterer is necessary and boundary conditions are rigorously included in the calculations. Volume integral equation (VIE) methods include the discrete dipole approximation (DDA) [72] and the Green's tensor technique [73], both widespread in the nanophotonics community. The DDA method has been generalized to a periodic array of scatterers [74,75] and more recently to periodic arrays embedded in a multilayer system [76]. However, VIE methods result in full matrices with a high cost in memory and computational time, including the evaluation of the periodic Green's function. For non-homogeneous scatterers, hybrid finite-element boundary-integral methods are proven very efficient and popular for microwaves [67,77].

With surface integral equation (SIE) methods [78–81] only the scatterer surface is discretized. Although SIE methods generate dense matrices, the fact that they scale with only the second power of the lateral dimension makes them very efficient for homogeneous scatterers. Very popular in the microwave community, SIE methods based on the method of moments (MoM) [67, 82] have also been extensively used in the microwave regime for periodic lossy [77, 83–85] or periodic metallic systems [86]. Recently, they have been successfully introduced to optics to simulate individual high permittivity and plasmonic scatterers [81]. A particularly attractive feature of this semi-analytical formulation is that it gives insights into the extreme near-field behavior, even for rapidly changing fields, as well as into the corresponding far-field radiation.

In this context, the development of a SIE formulation for the numerical study of 3D periodic systems, including Fano-resonant plasmonic structures, appears to be the most adequate choice, as it overcomes the numerical challenges of accuracy in the extreme near-field and the far-field, as well as providing a high flexibility in geometry and materials. Fano resonances have been first historically observed in metallic gratings [4] and often appear in periodic structures in state-of-the-art photonics [14, 15]. The purpose of this chapter is to report on the development and implementation of an original SIE method for periodic nanostructures. In Section 2.1, the surface integral equations for electromagnetic scattering will be first derived for periodic systems in infinite 3D space. Their numerical implementation will be discussed in Section 2.2, and finally the convergence properties of the method will be assessed in Section 2.3 using different canonical and experimentally relevant systems.

### 2.1 Surface integral equations for periodic systems.

The 3D space describing our scattering system is considered to be divided into  $N$  different regions  $V_n, n = 1, \dots, N$  with dielectric permittivity  $\epsilon_n$  and magnetic permeability  $\mu_n$  (Fig. 2.1). A harmonic time-dependence for the fields  $\mathbf{U}(\mathbf{r}, t) = \mathbf{U}_0(\mathbf{r})e^{-i\omega t}$  is assumed. The electric field  $\mathbf{E}$  in each region must satisfy the equation

$$\nabla \times \nabla \times \mathbf{E}(\mathbf{r}) - k_n^2 \mathbf{E}(\mathbf{r}) = i\omega \mu_n \mathbf{j}(\mathbf{r}), \quad \mathbf{r} \in V_n, \quad (2.1)$$

where  $k_n^2 = \omega^2 \epsilon_n \mu_n / c_0^2$  is the wavenumber for electromagnetic waves in region  $V_n$  and  $\mathbf{j}$  denotes the volume current density. A dyadic Green's function  $\underline{\underline{G}}_n$  for region  $V_n$  is introduced:

$$\nabla \times \nabla \times \underline{\underline{G}}_n(\mathbf{r}, \mathbf{r}') - k_n^2 \underline{\underline{G}}_n(\mathbf{r}, \mathbf{r}') = \underline{\underline{1}} \delta(\mathbf{r} - \mathbf{r}'). \quad (2.2)$$

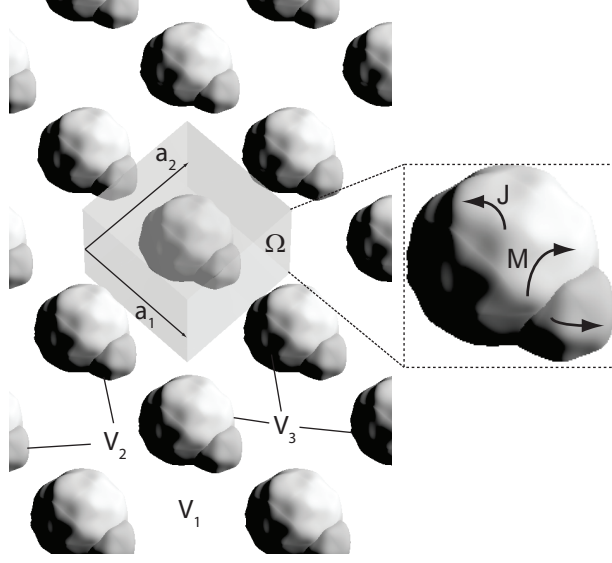


Figure 2.1: Space division into regions  $V_n$  with dielectric permittivity  $\epsilon_n$  and magnetic permeability  $\mu_n$ . The regions have the symmetry of a lattice with unit cell  $\Omega$  and primitive lattice vectors  $\mathbf{a}_i$ . Equivalent surface currents  $\mathbf{J}$  and  $\mathbf{M}$  flow on the scatterer surfaces.

Multiplying Eq. (2.1) by  $\underline{\underline{G}}_n(\mathbf{r}, \mathbf{r}')$  from the right and Eq. (2.2) by  $\mathbf{E}(\mathbf{r})$  from the left and subtracting the two equations, one obtains:

$$\begin{aligned} & [\nabla \times \nabla \times \mathbf{E}(\mathbf{r})] \cdot \underline{\underline{G}}_n(\mathbf{r}, \mathbf{r}') - \mathbf{E}(\mathbf{r}) \cdot [\nabla \times \nabla \times \underline{\underline{G}}_n(\mathbf{r}, \mathbf{r}')] \\ &= i\omega\mu_n \mathbf{j}(\mathbf{r}) \cdot \underline{\underline{G}}_n(\mathbf{r}, \mathbf{r}') - \mathbf{E}(\mathbf{r}) \delta(\mathbf{r} - \mathbf{r}'). \end{aligned} \quad (2.3)$$

Integrating Eq. (2.3) over  $V_n$ , and transforming its left-hand side following Eq. (A.45) in [87] leads to:

$$\begin{aligned} & \int_{V_n} dV \nabla \cdot \left( [\nabla \times \mathbf{E}(\mathbf{r})] \times \underline{\underline{G}}_n(\mathbf{r}, \mathbf{r}') + \mathbf{E}(\mathbf{r}) \times [\nabla \times \underline{\underline{G}}_n(\mathbf{r}, \mathbf{r}')] \right) \\ &= i\omega\mu_n \int_{V_n} dV \mathbf{j}(\mathbf{r}) \cdot \underline{\underline{G}}_n(\mathbf{r}, \mathbf{r}') - \begin{cases} \mathbf{E}(\mathbf{r}') : & \mathbf{r}' \in V_n \\ 0 : & \text{otherwise} \end{cases}. \end{aligned} \quad (2.4)$$

The integral on the right-hand side can be identified to the incident electric field  $\mathbf{E}_n^{\text{inc}}$  generated by the electrical current density  $\mathbf{j}$  inside  $V_n$ :

$$i\omega\mu_n \int_{V_n} dV \mathbf{j}(\mathbf{r}) \cdot \underline{\underline{G}}_n(\mathbf{r}, \mathbf{r}') = i\omega\mu_n \int_{V_n} dV \underline{\underline{G}}_n(\mathbf{r}', \mathbf{r}) \cdot \mathbf{j}(\mathbf{r}) = \mathbf{E}_n^{\text{inc}}(\mathbf{r}'), \quad (2.5)$$

where we used the reciprocity of the dyadic Green's function  $\underline{\underline{G}}_n(\mathbf{r}, \mathbf{r}')^T = \underline{\underline{G}}_n(\mathbf{r}', \mathbf{r})$ . The integral on the left-hand side of Eq. (2.4) can be transformed into a surface integral on

the boundary  $\partial V_n$  of region  $V_n$  using Gauss theorem:

$$\begin{aligned} & \int_{\partial V_n} dS \hat{\mathbf{n}}_n(\mathbf{r}) \cdot \left( [\nabla \times \mathbf{E}(\mathbf{r})] \times \underline{\underline{\mathbf{G}}}_n(\mathbf{r}, \mathbf{r}') + \mathbf{E}(\mathbf{r}) \times [\nabla \times \underline{\underline{\mathbf{G}}}_n(\mathbf{r}, \mathbf{r}')] \right) \\ &= \mathbf{E}_n^{\text{inc}}(\mathbf{r}') - \begin{cases} \mathbf{E}(\mathbf{r}') : & \mathbf{r}' \in V_n \\ 0 : & \text{otherwise} \end{cases}, \end{aligned} \quad (2.6)$$

where  $\hat{\mathbf{n}}_n$  is the outward oriented normal vector on the boundary  $\partial V_n$ . From the time-harmonic dependence of the fields and some dyadic analysis [87]:

$$\begin{aligned} \hat{\mathbf{n}}_n(\mathbf{r}) \cdot \left( [\nabla \times \mathbf{E}(\mathbf{r})] \times \underline{\underline{\mathbf{G}}}_n(\mathbf{r}, \mathbf{r}') \right) &= (\hat{\mathbf{n}}_n(\mathbf{r}) \times [\nabla \times \mathbf{E}(\mathbf{r})]) \cdot \underline{\underline{\mathbf{G}}}_n(\mathbf{r}, \mathbf{r}') \\ &= i\omega\mu_n \underline{\underline{\mathbf{G}}}_n(\mathbf{r}', \mathbf{r}) \cdot [\hat{\mathbf{n}}_n(\mathbf{r}) \times \mathbf{H}(\mathbf{r})]. \end{aligned} \quad (2.7)$$

On the other hand, using the reciprocity of the dyadic Green's function  $(\nabla \times \underline{\underline{\mathbf{G}}}_n(\mathbf{r}, \mathbf{r}'))^T = -\nabla \times \underline{\underline{\mathbf{G}}}_n(\mathbf{r}', \mathbf{r})$ :

$$\begin{aligned} \hat{\mathbf{n}}_n(\mathbf{r}) \cdot \left( \mathbf{E}(\mathbf{r}) \times [\nabla \times \underline{\underline{\mathbf{G}}}_n(\mathbf{r}, \mathbf{r}')] \right) &= [\hat{\mathbf{n}}_n(\mathbf{r}) \times \mathbf{E}(\mathbf{r})] \cdot [\nabla \times \underline{\underline{\mathbf{G}}}_n(\mathbf{r}, \mathbf{r}')] \\ &= -[\nabla \times \underline{\underline{\mathbf{G}}}_n(\mathbf{r}', \mathbf{r})] \cdot [\hat{\mathbf{n}}_n(\mathbf{r}) \times \mathbf{E}(\mathbf{r})]. \end{aligned} \quad (2.8)$$

Introducing the equivalent surface current densities  $\mathbf{J}_n = \hat{\mathbf{n}}_n \times \mathbf{H}$  and  $\mathbf{M}_n = -\hat{\mathbf{n}}_n \times \mathbf{E}$  defined on  $\partial V_n$  (Fig. 2.1), Eq. (2.6) becomes:

$$\begin{aligned} & i\omega\mu_n \int_{\partial V_n} dS' \underline{\underline{\mathbf{G}}}_n(\mathbf{r}, \mathbf{r}') \cdot \mathbf{J}_n(\mathbf{r}') + \int_{\partial V_n} dS' [\nabla' \times \underline{\underline{\mathbf{G}}}_n(\mathbf{r}, \mathbf{r}')] \cdot \mathbf{M}_n(\mathbf{r}') \\ &= \mathbf{E}_n^{\text{inc}}(\mathbf{r}) - \begin{cases} \mathbf{E}(\mathbf{r}) : & \mathbf{r} \in V_n \\ 0 : & \text{otherwise} \end{cases}. \end{aligned} \quad (2.9)$$

Taking the second case on the right-hand side of Eq. (2.9), the continuity of the tangential component of the fields  $\mathbf{E}$  and  $\mathbf{H}$  allows one to take the limit  $\mathbf{r} \rightarrow \partial V_n$ , leading to the electric field integral equation (EFIE):

$$\begin{aligned} & \left( i\omega\mu_n \int_{\partial V_n} dS' \underline{\underline{\mathbf{G}}}_n(\mathbf{r}, \mathbf{r}') \cdot \mathbf{J}_n(\mathbf{r}') + \int_{\partial V_n} dS' [\nabla' \times \underline{\underline{\mathbf{G}}}_n(\mathbf{r}, \mathbf{r}')] \cdot \mathbf{M}_n(\mathbf{r}') \right)_{\text{tan}} \\ &= \left( \mathbf{E}_n^{\text{inc}}(\mathbf{r}) \right)_{\text{tan}}, \quad \mathbf{r} \in \partial V_n, \end{aligned} \quad (2.10)$$

where the subscript tan denotes the tangential component of the fields. In a similar way, starting from the wave equation for the magnetic field:

$$\nabla \times \nabla \times \mathbf{H}(\mathbf{r}) - k_n^2 \mathbf{H}(\mathbf{r}) = \nabla \times \mathbf{j}(\mathbf{r}), \quad \mathbf{r} \in V_n, \quad (2.11)$$



## 2.1. Surface integral equations for periodic systems.

---

and identifying the incident magnetic field  $\mathbf{H}_n^{\text{inc}}$  generated by the electrical current density  $\mathbf{j}$  inside  $V_n$ :

$$\mathbf{H}_n^{\text{inc}}(\mathbf{r}') = \int_{V_n} dV [\nabla \times \mathbf{j}(\mathbf{r})] \cdot \underline{\underline{G}}_n(\mathbf{r}, \mathbf{r}'), \quad (2.12)$$

one obtains an equation analogous to Eq. (2.9):

$$\begin{aligned} & i\omega\epsilon_n \int_{\partial V_n} dS' \underline{\underline{G}}_n(\mathbf{r}, \mathbf{r}') \cdot \mathbf{M}_n(\mathbf{r}') - \int_{\partial V_n} dS' [\nabla \times \underline{\underline{G}}_n(\mathbf{r}, \mathbf{r}')] \cdot \mathbf{J}_n(\mathbf{r}') \\ &= \mathbf{H}_n^{\text{inc}}(\mathbf{r}) - \begin{cases} \mathbf{H}(\mathbf{r}) : & \mathbf{r} \in V_n \\ 0 : & \text{otherwise} \end{cases}, \end{aligned} \quad (2.13)$$

leading to the magnetic field integral equation (MFIE):

$$\begin{aligned} & \left( i\omega\epsilon_n \int_{\partial V_n} dS' \underline{\underline{G}}_n(\mathbf{r}, \mathbf{r}') \cdot \mathbf{M}_n(\mathbf{r}') - \int_{\partial V_n} dS' [\nabla' \times \underline{\underline{G}}_n(\mathbf{r}, \mathbf{r}')] \cdot \mathbf{J}_n(\mathbf{r}') \right)_{\text{tan}} \\ &= \left( \mathbf{H}_n^{\text{inc}}(\mathbf{r}) \right)_{\text{tan}}, \quad \mathbf{r} \in \partial V_n. \end{aligned} \quad (2.14)$$

The conservation of currents on a boundary  $\partial V_n = \partial V_m$  between two adjacent domains  $V_n$  and  $V_m$  requires  $\mathbf{J}_n = -\mathbf{J}_m$  and  $\mathbf{M}_n = -\mathbf{M}_m$  in Eqs. (2.10) and (2.14).

Let us now introduce the symmetry of a lattice in  $d$  directions ( $d = 1, 2, 3$ ). A lattice translation vector  $\mathbf{t}$  is a linear combination  $\mathbf{t} = \sum_i c_i \mathbf{a}_i$  with  $c_i \in \mathbb{Z}$  and  $\mathbf{a}_i, i = 1, \dots, d$  being the primitive lattice vectors. The unit cell of the lattice is called  $\Omega$  (Fig. 2.1). The irreducible representations of the translation group are defined by the wavevectors  $\mathbf{k}$  in the first Brillouin zone [88]. The one-dimensional spaces serving as basis for the irreducible representations are formed from Bloch functions  $\mathbf{U}_{\mathbf{k}}$  satisfying Floquet-periodic boundary conditions:

$$\mathbf{U}_{\mathbf{k}}(\mathbf{r} - \mathbf{t}) = e^{-i\mathbf{k} \cdot \mathbf{t}} \mathbf{U}_{\mathbf{k}}(\mathbf{r}). \quad (2.15)$$

The projection of the incident electric and magnetic fields onto this space are denoted by  $\mathbf{E}_{n,\mathbf{k}}^{\text{inc}}$  and  $\mathbf{H}_{n,\mathbf{k}}^{\text{inc}}$  respectively. If the source currents  $\mathbf{j}$  in Eq. (2.1) are not Floquet-periodic, one must develop the incident conditions  $\mathbf{E}_n^{\text{inc}}$  and  $\mathbf{H}_n^{\text{inc}}$  onto a linear combination of Floquet-periodic components  $\mathbf{E}_{n,\mathbf{k}}^{\text{inc}}$  and  $\mathbf{H}_{n,\mathbf{k}}^{\text{inc}}$ .

The computation of the EFIE (2.10) can be restricted to the boundary surfaces  $\partial V_n^\Omega \equiv$

$\partial V_n \cap \Omega$  in the unit cell:

$$\begin{aligned} & \left( i\omega\mu_n \int_{\partial V_n^\Omega} dS' \underline{\underline{G}}_{n,\mathbf{k}}(\mathbf{r}, \mathbf{r}') \cdot \mathbf{J}_{n,\mathbf{k}}(\mathbf{r}') + \int_{\partial V_n^\Omega} dS' [\nabla' \times \underline{\underline{G}}_{n,\mathbf{k}}(\mathbf{r}, \mathbf{r}')] \cdot \mathbf{M}_{n,\mathbf{k}}(\mathbf{r}') \right)_{\text{tan}} \\ & = \left( \mathbf{E}_{n,\mathbf{k}}^{\text{inc}}(\mathbf{r}) \right)_{\text{tan}}, \quad \mathbf{r} \in \partial V_n^\Omega. \end{aligned} \quad (2.16)$$

The same projection on the MFIE yields:

$$\begin{aligned} & \left( i\omega\epsilon_n \int_{\partial V_n^\Omega} dS' \underline{\underline{G}}_{n,\mathbf{k}}(\mathbf{r}, \mathbf{r}') \cdot \mathbf{M}_{n,\mathbf{k}}(\mathbf{r}') - \int_{\partial V_n^\Omega} dS' [\nabla' \times \underline{\underline{G}}_{n,\mathbf{k}}(\mathbf{r}, \mathbf{r}')] \cdot \mathbf{J}_{n,\mathbf{k}}(\mathbf{r}') \right)_{\text{tan}} \\ & = \left( \mathbf{H}_{n,\mathbf{k}}^{\text{inc}}(\mathbf{r}) \right)_{\text{tan}}, \quad \mathbf{r} \in \partial V_n^\Omega. \end{aligned} \quad (2.17)$$

Equations (2.16) and (2.17) are solved independently for each Floquet component of the equivalent surface currents  $\mathbf{J}_{n,\mathbf{k}}$  and  $\mathbf{M}_{n,\mathbf{k}}$ . The dyadic  $\underline{\underline{G}}_{n,\mathbf{k}}$  is the pseudo-periodic Green's function:

$$\underline{\underline{G}}_{n,\mathbf{k}}(\mathbf{r}, \mathbf{r}') = \sum_{\mathbf{t}} e^{i\mathbf{k} \cdot \mathbf{t}} \underline{\underline{G}}_n(\mathbf{r} - \mathbf{t}, \mathbf{r}'), \quad (2.18)$$

It satisfies  $\underline{\underline{G}}_{n,\mathbf{k}}(\mathbf{r} - \mathbf{t}, \mathbf{r}') = e^{-i\mathbf{k} \cdot \mathbf{t}} \underline{\underline{G}}_{n,\mathbf{k}}(\mathbf{r}, \mathbf{r}')$  and  $\underline{\underline{G}}_{n,\mathbf{k}}(\mathbf{r}, \mathbf{r}')^\dagger = \underline{\underline{G}}_{n,\mathbf{k}}(\mathbf{r}', \mathbf{r})$  where  $\underline{\underline{G}}_{n,\mathbf{k}}(\mathbf{r}, \mathbf{r}')^\dagger$  is the conjugate transposed of  $\underline{\underline{G}}_{n,\mathbf{k}}(\mathbf{r}, \mathbf{r}')$ . The equivalent surface currents  $\mathbf{J}_{n,\mathbf{k}}$  and  $\mathbf{M}_{n,\mathbf{k}}$ , solutions of the EFIE and MFIE, are not the actual currents flowing on the surfaces  $\partial V_n^\Omega$ , but they produce the same electromagnetic field inside the regions  $V_n^\Omega$ .

In a similar way, from the first case in Eqs. (2.9) and (2.13), an expression for the electric and magnetic fields scattered by the objects at any point  $\mathbf{r} \in V_n$  can be derived:

$$\begin{aligned} \mathbf{E}_{n,\mathbf{k}}^{\text{scat}}(\mathbf{r}) & = \\ & - i\omega\mu_n \int_{\partial V_n^\Omega} dS' \underline{\underline{G}}_{n,\mathbf{k}}(\mathbf{r}, \mathbf{r}') \cdot \mathbf{J}_{n,\mathbf{k}}(\mathbf{r}') - \int_{\partial V_n^\Omega} dS' [\nabla' \times \underline{\underline{G}}_{n,\mathbf{k}}(\mathbf{r}, \mathbf{r}')] \cdot \mathbf{M}_{n,\mathbf{k}}(\mathbf{r}'), \end{aligned} \quad (2.19)$$

$$\begin{aligned} \mathbf{H}_{n,\mathbf{k}}^{\text{scat}}(\mathbf{r}) & = \\ & - i\omega\epsilon_n \int_{\partial V_n^\Omega} dS' \underline{\underline{G}}_{n,\mathbf{k}}(\mathbf{r}, \mathbf{r}') \cdot \mathbf{M}_{n,\mathbf{k}}(\mathbf{r}') + \int_{\partial V_n^\Omega} dS' [\nabla' \times \underline{\underline{G}}_{n,\mathbf{k}}(\mathbf{r}, \mathbf{r}')] \cdot \mathbf{J}_{n,\mathbf{k}}(\mathbf{r}'). \end{aligned} \quad (2.20)$$

For simplicity, the labels  $\mathbf{k}$  and  $\Omega$  are omitted in the following. With Equations (2.19) and (2.20), one can calculate at any point of space the electric and/or the magnetic fields induced by the currents  $\mathbf{J}_{n,\mathbf{k}}$  and  $\mathbf{M}_{n,\mathbf{k}}$ .

## 2.2 Numerical implementation

Details on the numerical implementation of the EFIE (2.16) and MFIE (2.17) are given in this section. They require the evaluation of the periodic Green's function, a time-consuming step without the use of an accelerating technique such as Ewald's method. Hence, the utilization of Ewald's method for this problem is first detailed. It is followed by the discretization of the EFIE and MFIE with the MoM for an arbitrary number of regions and boundary surfaces. For periodic systems, this requires the implementation of specific boundary conditions when the scatterer completely fills the unit cell.

### 2.2.1 Evaluation of the periodic Green's function with Ewald's method

Although the integral Eqs. (2.16) and (2.17) can be applied for periodicities in 1, 2 or 3 directions, we shall now focus on the most common physical situation and assume that the regions  $V_n$  carry the symmetry of a two-dimensional lattice with primitive translation vectors  $\mathbf{a}_1$  and  $\mathbf{a}_2$ . Details about the implementation of Ewald's method for periodicities in 1, respectively 3 directions can be found e.g. in Refs. [89, 90], respectively [91]. The area of the unit cell is  $|\Omega| = |\mathbf{a}_1 \times \mathbf{a}_2|$ . Let us define  $\mathbf{R} = \mathbf{r} - \mathbf{r}'$  and  $\mathbf{R}_t = \mathbf{R} - \mathbf{t}$  with  $\mathbf{t} = c_1 \mathbf{a}_1 + c_2 \mathbf{a}_2$  and  $c_1, c_2 \in \mathbb{Z}$ . The periodic dyadic Green's function (2.18) depends on  $\mathbf{R}$  only:

$$\underline{\underline{G}}_n(\mathbf{r}, \mathbf{r}') = \left( \underline{\underline{1}} + \frac{\nabla \nabla}{k_n^2} \right) G_n(\mathbf{r}, \mathbf{r}'), \quad (2.21)$$

where

$$G_n(\mathbf{r}, \mathbf{r}') = \sum_{\mathbf{t}} \frac{e^{ik_n |\mathbf{R}_t|}}{4\pi |\mathbf{R}_t|} e^{i\mathbf{k} \cdot \mathbf{t}}. \quad (2.22)$$

In fact, Eqs. (2.16) and (2.17) can be transformed following Ref. [81] to involve the evaluation of the Green's function (2.22) and its gradient only. The infinite sum in Eq. (2.22) converges slowly and requires many terms to reach a reasonable accuracy. The asymptotic behavior of these terms for  $|\mathbf{t}| \gg k_n^{-1}$  is in  $|\mathbf{t}|^{-1}$ . The sum is expected to converge and can be truncated for a numerical evaluation with a given precision requirement. Another possibility of evaluating  $G_{n,\mathbf{k}}$  is to expand it into the reciprocal lattice using Poisson formula [92]:

$$G_{n,\mathbf{k}}(\mathbf{R}) = \frac{1}{|\Omega|} \sum_{\mathbf{u}} \tilde{G}_n(\mathbf{k} - \mathbf{u}, \mathbf{R}), \quad (2.23)$$

where

$$\tilde{G}_n(\mathbf{k} - \mathbf{u}, \mathbf{R}) = \int_{\mathbb{R}^2} \frac{e^{ik_n |\mathbf{R}_t|}}{4\pi |\mathbf{R}_t|} e^{i(\mathbf{k}-\mathbf{u}) \cdot \mathbf{t}} d\mathbf{t}. \quad (2.24)$$

## Chapter 2. Surface integral equation method for periodic nanostructures

---

Note that in Eq. (2.24) the vector  $\mathbf{t}$  is not anymore a discrete but continuous linear combination of lattice vectors  $\mathbf{a}_i$ . With Eq. (2.23), an infinite amount of terms is also required for evaluating  $G_{n,\mathbf{k}}$ , which become small for  $|\mathbf{u}| \gg k_n$ . Both sums in Eqs. (2.22) and (2.23) converge slowly [92]. Their evaluation is very long in order to reach an acceptable degree of accuracy and an accelerating technique is therefore required.

It has been shown that Ewald's transformation efficiently accelerates the convergence of the Green's function computation [86]. The following identity is applied to each term of Eq. (2.22):

$$\frac{e^{ikR}}{R} = \frac{2}{\sqrt{\pi}} \int_0^{\infty} e^{-R^2 s^2 + \frac{k^2}{4s^2}} ds, \quad (2.25)$$

where the path of integration has to be carefully chosen [93]. Breaking the integral into two parts  $(0, E)$  and  $(E, \infty)$ , the sum of Eq. (2.22) is now written as:

$$G_{n,\mathbf{k}} = G_{n,\mathbf{k}}^{(1)} + G_{n,\mathbf{k}}^{(2)}, \quad (2.26)$$

where

$$G_{n,\mathbf{k}}^{(1)}(\mathbf{R}) = \frac{1}{4\pi} \sum_{\mathbf{t}} e^{i\mathbf{k}\cdot\mathbf{t}} \frac{2}{\sqrt{\pi}} \int_0^E e^{-|\mathbf{R}\mathbf{t}|^2 s^2 + \frac{k_n^2}{4s^2}} ds \quad (2.27)$$

$$G_{n,\mathbf{k}}^{(2)}(\mathbf{R}) = \frac{1}{4\pi} \sum_{\mathbf{t}} e^{i\mathbf{k}\cdot\mathbf{t}} \frac{2}{\sqrt{\pi}} \int_E^{\infty} e^{-|\mathbf{R}\mathbf{t}|^2 s^2 + \frac{k_n^2}{4s^2}} ds. \quad (2.28)$$

Let us define  $R_{\perp}$  as the component of  $\mathbf{R}$  in the direction normal to both  $\mathbf{a}_1$  and  $\mathbf{a}_2$ . For  $G_{n,\mathbf{k}}^{(1)}(\mathbf{R})$ , we use Eqs. (2.23) and (2.24) to transform Eq. (2.27) into a sum over the

reciprocal lattice vectors:

$$\begin{aligned}
 & \sum_{\mathbf{t}} e^{i\mathbf{k}\cdot\mathbf{t}} \int_0^E e^{-|\mathbf{R}\mathbf{t}|^2 s^2 + \frac{k_n^2}{4s^2}} ds \\
 &= \frac{1}{|\Omega|} \sum_{\mathbf{u}} e^{i(\mathbf{k}-\mathbf{u})\cdot\mathbf{R}} \int_0^E ds e^{\frac{k_n^2}{4s^2}} \int_{\mathbb{R}^2} dt e^{-i(\mathbf{k}-\mathbf{u})\cdot\mathbf{t}} e^{-|\mathbf{t}|^2 s^2} e^{-R_{\perp}^2 s^2} \\
 &= \frac{\pi}{|\Omega|} \sum_{\mathbf{u}} e^{i(\mathbf{k}-\mathbf{u})\cdot\mathbf{R}} \int_0^E ds \frac{e^{\frac{k_n^2}{4s^2} - \frac{|\mathbf{k}-\mathbf{u}|^2}{4s^2}}}{s^2} e^{-R_{\perp}^2 s^2} \\
 &= \frac{\pi}{|\Omega|} \sum_{\mathbf{u}} e^{i(\mathbf{k}-\mathbf{u})\cdot\mathbf{R}} \int_{1/E}^{\infty} ds e^{-(\gamma_{n,\mathbf{k},\mathbf{u}})^2 s^2/4} e^{-R_{\perp}^2/s^2} \\
 &= \frac{\pi^{3/2}}{2|\Omega|} \sum_{\mathbf{u}} e^{i(\mathbf{k}-\mathbf{u})\cdot\mathbf{R}} \sum_{\pm} \frac{e^{\pm\gamma_{n,\mathbf{k},\mathbf{u}} R_{\perp}}}{\gamma_{n,\mathbf{k},\mathbf{u}}} \operatorname{erfc}\left(\frac{\gamma_{n,\mathbf{k},\mathbf{u}}}{2E} \pm R_{\perp} E\right), \tag{2.29}
 \end{aligned}$$

where  $\gamma_{n,\mathbf{k},\mathbf{u}} = \sqrt{|\mathbf{k}-\mathbf{u}|^2 - k_n^2}$  and the second sum has two terms: one where  $\pm$  is replaced by  $-$  and the other by  $+$ . In the last step of Eq. (2.29), the identity

$$\int_E^{\infty} e^{-p^2 s^2 + \frac{q^2}{4s^2}} ds = \frac{\sqrt{\pi}}{4p} \sum_{\pm} e^{\pm ipq} \operatorname{erfc}\left(pE \pm \frac{iq}{2E}\right) \tag{2.30}$$

has been used. With the choice of integration path of Jordan [93], the imaginary part of  $s$  is positive when its real part is in  $[1/E, \infty]$ . If  $p^2 < 0$ , the imaginary part of  $p$  has to be negative in order to ensure the convergence of the integral, implying the choice an appropriate definition for  $\gamma_{n,\mathbf{k},\mathbf{u}}$  on the square root branch cut. Finally, from Eq. (2.29):

$$G_{n,\mathbf{k}}^{(1)}(\mathbf{R}) = \frac{1}{4|\Omega|} \sum_{\mathbf{u}} e^{i(\mathbf{k}-\mathbf{u})\cdot\mathbf{R}} \sum_{\pm} \frac{e^{\pm\gamma_{n,\mathbf{k},\mathbf{u}} R_{\perp}}}{\gamma_{n,\mathbf{k},\mathbf{u}}} \operatorname{erfc}\left(\frac{\gamma_{n,\mathbf{k},\mathbf{u}}}{2E} \pm R_{\perp} E\right). \tag{2.31}$$

On the other hand, a direct application of the identity (2.30) yields:

$$G_{n,\mathbf{k}}^{(2)}(\mathbf{R}) = \frac{1}{8\pi} \sum_{\mathbf{t}} e^{i\mathbf{k}\cdot\mathbf{t}} \sum_{\pm} \frac{e^{\pm ik_n |\mathbf{R}\mathbf{t}|}}{|\mathbf{R}\mathbf{t}|} \operatorname{erfc}\left(|\mathbf{R}\mathbf{t}| E \pm \frac{ik_n}{2E}\right), \tag{2.32}$$

where  $\mathbf{R}\mathbf{t} = \mathbf{r} - \mathbf{r}' - \mathbf{t}$ . Equivalently, the sum in Eq. (2.32) has terms comparable to  $\exp(-|\mathbf{t}|^2 E^2)/(E|\mathbf{t}|^2)$  for  $|\mathbf{t}| \gg k_n^{-1}$ , ensuring a Gaussian convergence rate as well. Figure 2.2 shows that the Green's function evaluation with Eq. (2.26) is efficiently accelerated. The evaluation of complex error functions requires however a numerical effort. In order to further reduce the computation time, the values of this function are precomputed and stored in a table, reducing each call of the function to only a first

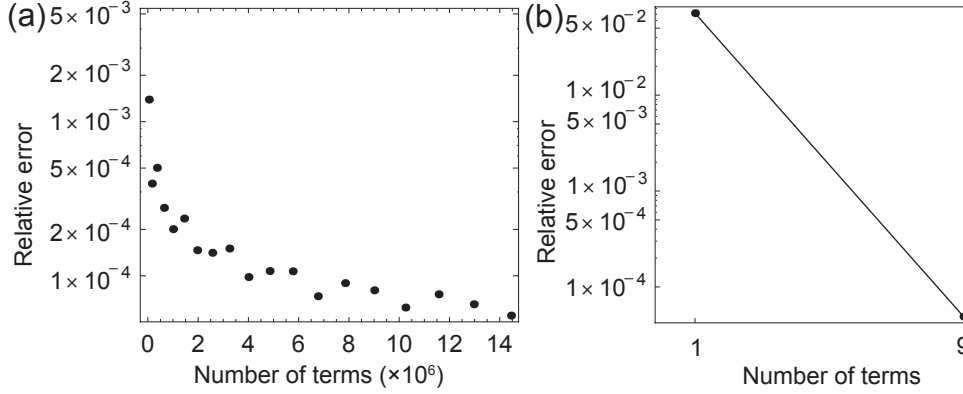


Figure 2.2: Relative error  $|G(\mathbf{r}, \mathbf{r}') - G_{\text{ref}}(\mathbf{r}, \mathbf{r}')|/|G_{\text{ref}}(\mathbf{r}, \mathbf{r}')|$  in the evaluation of the pseudo-periodic Green's function with (a) the direct method [Eq. (2.22)] and (b) Ewald's method [Eq. (2.26)] as a function of the number of terms in the sums. The period  $a$  in each direction is 100 nm, the wavelength  $\lambda/a=4$ , the relative position  $\mathbf{r} - \mathbf{r}' = (a/2, a/2, 0)$  and  $\mathbf{k} = (0, 0, 0)$ . The reference value is obtained from Ewald's sum with a large number of terms. For this example, the evaluation with Ewald's method in (b) is 5140 times faster than with the direct sum in (a).

order interpolation. Ewald's transformation has been able to very efficiently improve the convergence of  $G_{n,\mathbf{k}}(\mathbf{r}, \mathbf{r}')$  for a periodicity in two dimensions.

Another required quantity is the gradient of the Green's function. For the Ewald's sums we have:

$$\begin{aligned} \nabla G_{n,\mathbf{k}}^{(1)}(\mathbf{r}, \mathbf{r}') &= \frac{1}{4|\Omega|} \sum_{\mathbf{u}} e^{i(\mathbf{k}-\mathbf{u})\cdot\mathbf{R}} \sum_{\pm} \left[ \pm \hat{n} \left( e^{\pm\gamma_{n,\mathbf{k},\mathbf{u}}R_{\perp}} \operatorname{erfc} \left( \frac{\gamma_{n,\mathbf{k},\mathbf{u}}}{2E} \pm R_{\perp}E \right) \right) \right. \\ &+ i(\mathbf{k} - \mathbf{u}) \frac{e^{\pm\gamma_{n,\mathbf{k},\mathbf{u}}R_{\perp}}}{\gamma_{n,\mathbf{k},\mathbf{u}}} \operatorname{erfc} \left( \frac{\gamma_{n,\mathbf{k},\mathbf{u}}}{2E} \pm R_z E \right) \\ &\mp \left. \frac{2E\hat{n}}{\gamma_{n,\mathbf{k},\mathbf{u}}\sqrt{\pi}} e^{\pm\gamma_{n,\mathbf{k},\mathbf{u}}R_{\perp}} e^{-\left(\frac{\gamma_{n,\mathbf{k},\mathbf{u}}}{2E} \pm R_{\perp}E\right)^2} \right]. \end{aligned} \quad (2.33)$$

$$\begin{aligned} \nabla G_{n,\mathbf{k}}^{(2)}(\mathbf{r}, \mathbf{r}') &= \frac{1}{8\pi} \sum_{\mathbf{t}} \frac{\mathbf{R}_{\mathbf{t}}}{|\mathbf{R}_{\mathbf{t}}|} e^{i\mathbf{k}\cdot\mathbf{t}} \left[ -\frac{4E}{|\mathbf{R}_{\mathbf{t}}|\sqrt{\pi}} e^{-|\mathbf{R}_{\mathbf{t}}|^2 E^2 + \frac{k_n^2}{4E^2}} \right. \\ &+ \left. \sum_{\pm} \frac{(-1 \pm ik_n |\mathbf{R}_{\mathbf{t}}|) e^{\pm ik_n |\mathbf{R}_{\mathbf{t}}|}}{|\mathbf{R}_{\mathbf{t}}|^2} \operatorname{erfc} \left( |\mathbf{R}_{\mathbf{t}}| E \pm \frac{ik_n}{2E} \right) \right], \end{aligned} \quad (2.34)$$

where  $\hat{n}$  is a unit vector oriented along  $\mathbf{a}_1 \times \mathbf{a}_2$ . The best choice  $E_0$  for the splitting parameter  $E$  is the one that balances the decay rate of the two series  $G_n^{(1)}$  and  $G_n^{(2)}$  [86]. Good results are obtained for  $E_0 = \sqrt{\pi/|\Omega|}$  for wavelengths similar to the array period [86].

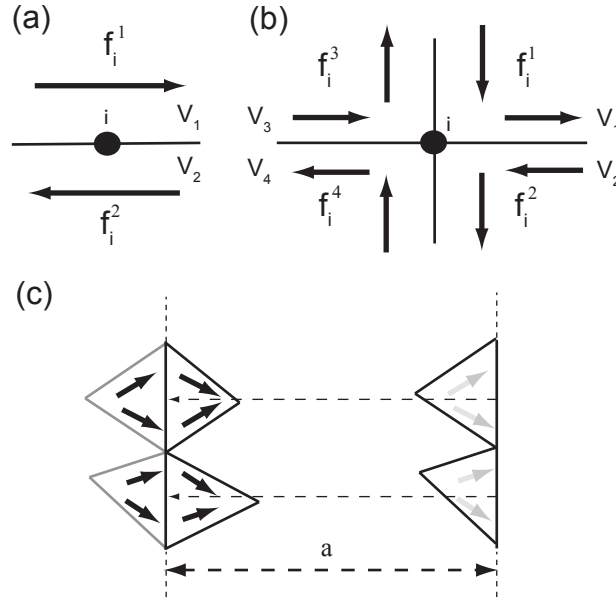


Figure 2.3: (a) Conservation of the current across the boundary between regions  $V_1$  and  $V_2$  implies for the RWG functions  $\mathbf{f}_i^1$  and  $\mathbf{f}_i^2$  associated to the same edge  $i$  to have opposite signs. (b) This property can be generalized to an arbitrary number of boundaries associated to the same edge. (c) If the discretization reaches opposite ends of the unit cell, currents on these borders are not linearly independent. The mesh has to be translation symmetric and one border is removed from the calculations.

### 2.2.2 Solution by Method of Moments

A technique for solving the EFIE (2.16) and the MFIE (2.17) is the method of moments (MoM) [82]. The equivalent surface currents are expanded in terms of Rao-Wilton-Glisson (RWG) basis functions  $\mathbf{f}_i^n$  building a triangular mesh approximating the boundary surface  $\partial V_n$  [94]:

$$\mathbf{J}_n = \sum_i \alpha_i \mathbf{f}_i^n \quad (2.35)$$

$$\mathbf{M}_n = \sum_i \beta_i \mathbf{f}_i^n, \quad (2.36)$$

where the index  $i$  labels the different edges within all regions (Fig. 2.1). If two RWG functions  $\mathbf{f}_i^n$  and  $\mathbf{f}_i^{n'}$  are associated to the same edge, the conservation of current on  $\partial V_n = \partial V_{n'}$  between the two adjacent regions  $V_n$  and  $V_{n'}$  implies  $\mathbf{f}_i^n = -\mathbf{f}_i^{n'}$  (Fig. 2.3(a), see also Ref. [95]). If more than two regions are touching an edge, all the expansion coefficients related to this edge are identified [Fig. 2.3(b)]. In this case, more than one RWG function is associated to the same edge, but only one per adjacent region. If region  $V_n$  is not adjacent to the edge  $i$ , then  $\mathbf{f}_i^n \equiv 0$ . Similarly to the FEM, the Galerkin method

is applied, multiplying Eqs. (2.16) and (2.17) with the basis functions and integrating over  $\partial V_n$ . Defining the sets  $\{\alpha\}$  and  $\{\beta\}$  of expansion coefficients  $\alpha_i$  and  $\beta_i$ , the EFIE (2.16) can be rewritten as a matrix equation for  $\{\alpha\}$  and  $\{\beta\}$ :

$$\begin{bmatrix} i\omega\mu_n \mathbf{D}^n & \mathbf{K}^n \end{bmatrix} \cdot \begin{bmatrix} \{\alpha\} \\ \{\beta\} \end{bmatrix} = \mathbf{q}^{(E),n}, \quad (2.37)$$

with submatrices

$$D_{ij}^n = \int_{\partial V_n} dS \mathbf{f}_i^n(\mathbf{r}) \cdot \int_{\partial V_n} dS' \underline{\underline{G}}_n(\mathbf{r}, \mathbf{r}') \cdot \mathbf{f}_j^n(\mathbf{r}') \quad (2.38)$$

$$K_{ij}^n = \int_{\partial V_n} dS \mathbf{f}_i^n(\mathbf{r}) \cdot \int_{\partial V_n} dS' [\nabla' \times \underline{\underline{G}}_n(\mathbf{r}, \mathbf{r}')] \cdot \mathbf{f}_j^n(\mathbf{r}'), \quad (2.39)$$

and

$$q_i^{(E),n} = \int_{\partial V_n} dS \mathbf{f}_i^n(\mathbf{r}) \cdot \mathbf{E}_n^{\text{inc}}(\mathbf{r}). \quad (2.40)$$

A similar matrix equation can be found for the MFIE (2.17):

$$\begin{bmatrix} \mathbf{K}^n & -i\omega\epsilon_n \mathbf{D}^n \end{bmatrix} \cdot \begin{bmatrix} \{\alpha\} \\ \{\beta\} \end{bmatrix} = \mathbf{q}^{(H),n}, \quad (2.41)$$

with

$$q_i^{(H),n} = - \int_{\partial V_n} dS \mathbf{f}_i^n(\mathbf{r}) \cdot \mathbf{H}_n^{\text{inc}}(\mathbf{r}). \quad (2.42)$$

The integrals (2.38) and (2.39) can be computed numerically using Gaussian quadrature [96]. The periodic Green's function and its gradient are evaluated using the results of Section 2.2.1. In some cases, solving for  $\{\alpha\}$  and  $\{\beta\}$  with the EFIE or the MFIE does not result in the same values. In fact, especially in resonant conditions such as plasmonic systems, the values may also exhibit large errors due to poor testing. The Poggio-Miller-Chang-Harrington-Wu-Tsai formulation (PMCHWT) combines EFIE and MFIE to solve them simultaneously [97]. Although the PMCHWT formulation might lead to poor conditioning of the system matrix and a slow convergence for iterative solvers [78], it has proven to give stable and accurate results [98,99], even in resonant conditions [81]. In that case, Eqs. (2.37) and (2.41) are combined for all regions, summing over  $n$ :

$$\begin{bmatrix} \sum_n i\omega\mu_n \mathbf{D}^n & \sum_n \mathbf{K}^n \\ \sum_n \mathbf{K}^n & -\sum_n i\omega\epsilon_n \mathbf{D}^n \end{bmatrix} \cdot \begin{bmatrix} \{\alpha\} \\ \{\beta\} \end{bmatrix} = \sum_n \begin{bmatrix} \mathbf{q}^{(E),n} \\ \mathbf{q}^{(H),n} \end{bmatrix}. \quad (2.43)$$



Equation (2.43) can be solved for  $\{\alpha\}$  and  $\{\beta\}$  to obtain the values of the equivalent surface currents  $\mathbf{J}$  and  $\mathbf{M}$  flowing on the interfaces between different media. The scattered electric and magnetic fields can then be obtained in each region  $V_n$  from  $\{\alpha\}$  and  $\{\beta\}$ . Inserting the decompositions (2.35) and (2.36) in Eqs. (2.19) and (2.20):

$$\mathbf{E}_n^{\text{scat}}(\mathbf{r}) = \sum_i -i\omega\mu_n \int_{\partial V_n} dS' \underline{\underline{G}}_n(\mathbf{r}, \mathbf{r}') \cdot \alpha_i \mathbf{f}_i^n(\mathbf{r}') - \int_{\partial V_n} dS' [\nabla' \times \underline{\underline{G}}_n(\mathbf{r}, \mathbf{r}')] \cdot \beta_i \mathbf{f}_i^n(\mathbf{r}'), \quad (2.44)$$

$$\mathbf{H}_n^{\text{scat}}(\mathbf{r}) = \sum_i -i\omega\epsilon_n \int_{\partial V_n} dS' \underline{\underline{G}}_n(\mathbf{r}, \mathbf{r}') \cdot \beta_i \mathbf{f}_i^n(\mathbf{r}') + \int_{\partial V_n} dS' [\nabla' \times \underline{\underline{G}}_n(\mathbf{r}, \mathbf{r}')] \cdot \alpha_i \mathbf{f}_i^n(\mathbf{r}'). \quad (2.45)$$

The matrix elements in Eqs. (2.38) and (2.39) can be turned into integrals involving the scalar Green's function  $G_n(\mathbf{r}, \mathbf{r}')$  or its gradient in their integrand, which are known to diverge for  $|\mathbf{r}' - \mathbf{r}| \rightarrow 0$ . This behavior of the Green's function can also lead to inaccurate results in the numerical evaluation of the matrix elements relative to neighboring triangles. An elegant way to overcome this difficulty is to separate the Green's function into a singular part that can be integrated in a closed form and a smooth, slowly varying part that can be accurately integrated numerically. Following Ref. [100] [Eqs. (6) and (20)], the matrix elements in Eq. (2.38) can be transformed into:

$$\begin{aligned} D_{ij}^n &= \int_{\partial V_n} dS \mathbf{f}_i^n(\mathbf{r}) \cdot \left( \underline{\underline{1}} + \frac{\nabla \nabla}{k_n^2} \right) \cdot \int_{\partial V_n} dS' G_n(\mathbf{r}, \mathbf{r}') \cdot \mathbf{f}_j^n(\mathbf{r}') \\ &= \frac{1}{k_n^2} \int_{\partial V_n} dS \mathbf{f}_i^n(\mathbf{r}) \cdot \nabla \int_{\partial V_n} dS' G_n(\mathbf{r}, \mathbf{r}') \nabla' \cdot \mathbf{f}_j^n(\mathbf{r}') \\ &\quad + \int_{\partial V_n} dS \mathbf{f}_i^n(\mathbf{r}) \cdot \int_{\partial V_n} dS' G_n(\mathbf{r}, \mathbf{r}') \mathbf{f}_j^n(\mathbf{r}') \\ &= -\frac{1}{k_n^2} \int_{\partial V_n} dS \nabla \cdot \mathbf{f}_i^n(\mathbf{r}) \int_{\partial V_n} dS' G_n(\mathbf{r}, \mathbf{r}') \nabla' \cdot \mathbf{f}_j^n(\mathbf{r}') \\ &\quad + \int_{\partial V_n} dS \mathbf{f}_i^n(\mathbf{r}) \cdot \int_{\partial V_n} dS' G_n(\mathbf{r}, \mathbf{r}') \mathbf{f}_j^n(\mathbf{r}'). \end{aligned} \quad (2.46)$$

Using the identity  $\nabla' \times \underline{\underline{G}}_n(\mathbf{r}, \mathbf{r}') = -[\nabla \underline{\underline{G}}_n(\mathbf{r}, \mathbf{r}')] \times \underline{\underline{1}}$ , the matrix elements in Eq. (2.39) become:

$$\begin{aligned} K_{ij}^n &= \int_{\partial V_n} dS \mathbf{f}_i^n(\mathbf{r}) \cdot \int_{\partial V_n} dS' [\nabla' \times \underline{\underline{G}}_{n,\mathbf{k}}(\mathbf{r}, \mathbf{r}')] \cdot \mathbf{f}_j^n(\mathbf{r}') \\ &= \int_{\partial V_n} dS \mathbf{f}_i^n(\mathbf{r}) \cdot \int_{\partial V_n} dS' [\nabla' G_n(\mathbf{r}, \mathbf{r}')] \times \mathbf{f}_j^n(\mathbf{r}'). \end{aligned} \quad (2.47)$$

The lattice sum  $G_n^{(2)}$  [Eq. (2.32)] has a singularity for  $|\mathbf{R}| \rightarrow 0$ . The Green's function and its gradient can be separated into a singular part that can be integrated in a closed form [100] and a smooth, slowly varying part that can be accurately integrated numerically:

$$G_n(\mathbf{r}, \mathbf{r}') = G_n^{(s)}(\mathbf{R}) + \frac{1}{4\pi} \left( \frac{1}{|\mathbf{R}|} - \frac{k_n^2 |\mathbf{R}|}{2} \right), \quad (2.48)$$

where  $G_n^{(s)}(\mathbf{r}, \mathbf{r}')$  is non-singular and differentiable for  $|\mathbf{R}| \rightarrow 0$ . The following formulae around the singularity can be used:

$$\lim_{R \rightarrow 0} \left[ \sum_{\pm} \frac{e^{\pm ikR}}{R} \operatorname{erfc} \left( RE \pm \frac{ik}{2E} \right) - \frac{2}{R} \right] = -\frac{4E}{\sqrt{\pi}} e^{\frac{k^2}{4E^2}} + 2ik \left[ \operatorname{erfc} \left( \frac{ik}{2E} \right) - 1 \right] \quad (2.49)$$

$$\begin{aligned} \lim_{R \rightarrow 0} \left[ -\frac{4E}{R\sqrt{\pi}} e^{-R^2 E^2 + \frac{k^2}{4E^2}} + \sum_{\pm} \frac{-1 \pm ikR}{R^2} e^{\pm ikR} \operatorname{erfc} \left( RE \pm \frac{ik}{2E} \right) + \frac{2}{R^2} \right] \\ = -k^2. \end{aligned} \quad (2.50)$$

With this procedure, highly conductive metals with Green's function approaching a Dirac distribution can therefore be handled accurately. The same procedure can be repeated for the fields evaluation using Eqs. (2.44) and (2.45), which guarantees an accurate field evaluation close to the scatterer surface.

If the discretized object completely fills the unit cell, the discretization mesh must be translation symmetric on opposite edges, in order to guaranty the continuity of the current flowing across the unit cell [Fig. 2.3(c)]. The periodic boundary condition (2.15) imposes a constraint on the equivalent surface currents:

$$\begin{aligned} \mathbf{J}_n(\mathbf{r} - \mathbf{t}) &= e^{-i\mathbf{k} \cdot \mathbf{t}} \mathbf{J}_n(\mathbf{r}) \\ \mathbf{M}_n(\mathbf{r} - \mathbf{t}) &= e^{-i\mathbf{k} \cdot \mathbf{t}} \mathbf{M}_n(\mathbf{r}). \end{aligned}$$

Hence, currents on opposite borders are not linearly independent. If two edges are separated from each other by a lattice vector, their associated expansion coefficients must be identified. The RWG function associated to the resulting edge is defined over the existing border triangle inside the unit cell and a translation of the triangle attached to the opposite, discarded, edge [Fig 2.3(c)].

## 2.3 Convergence assessment

In this Section, the convergence of the SIE method is assessed using routine tests from grating theories. The first of them consists in comparing the numerical and the analytical solutions for the simple case of infinite planar interfaces. In Section 2.3.2, the optical

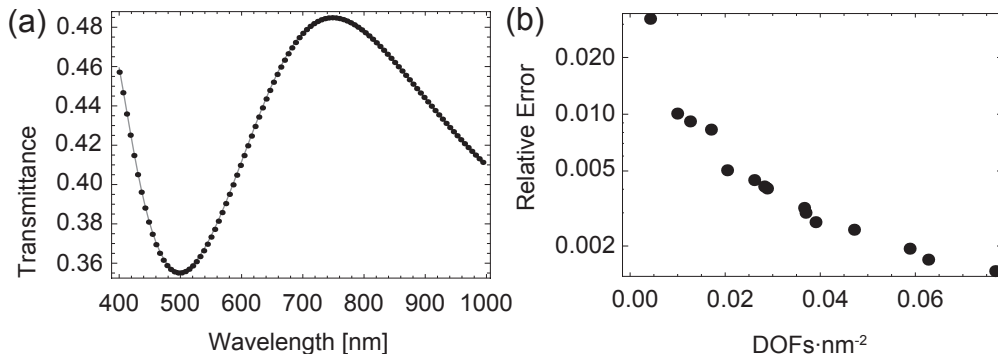


Figure 2.4: Transmittance spectrum on an asymmetric dielectric slab. The superstrate is air and the substrate has a refractive index of 1.5. The slab is a dielectric material with a refractive index of 2 and is illuminated by a  $s$ -polarized plane wave at  $45^\circ$  incidence from air. (a) Solid line: analytical solution. Points: computation with the SIE method. (b) Relative error in the numerical evaluation of the transmittance at  $\lambda = 600$  nm as a function of the surface density of degrees of freedom (DOFs).

properties of a photonic crystal of dielectric pillars with square and hexagonal periodicities are investigated, and energy conservation and reciprocity are tested as a function of the incident wavelength. In Section 2.3.3, surface plasmon resonances are excited on a silver thin film and compared to results obtained with a transfer matrix method. As a final illustration of the technique, the effective refractive index of a fishnet metamaterial is compared to published experimental data.

### 2.3.1 Infinite planar interfaces

In this first example, the scatterer surface is made of two parallel square surfaces separated by 200 nm and filling completely the unit cell, mimicking an infinite slab between two semi-infinite media with different dielectric permittivities. To assess the accuracy of the method, the transmittance spectrum is computed and compared to the analytical solution  $T_{\text{anal}}$  in Fig. 2.4(a). The intensity of the scattered field is computed in the substrate at approximately 50 wavelengths from the slab to obtain the transmittance  $T_{\text{comp}}$ . The accurate evaluation of the Green's function with Ewald's method ensures that the obtained transmittance is independent of the evaluation position in the far-field. The relative error  $|T_{\text{comp}} - T_{\text{anal}}|/|T_{\text{comp}}|$  as a function of the surface density of degrees of freedom (DOFs) is computed and reported in Fig. 2.4(b). The number of DOFs is twice the number of edges in the mesh, since two unknowns are associated to each edge. The system of equations is solved with the LU decomposition package LAPACK [101]. The SIE formulation presented for individual scatterers in Ref. [81] has been proven to be more accurate than VIE methods. Comparing Fig. 2.4 and Fig. 3 of Ref. [81], the surface

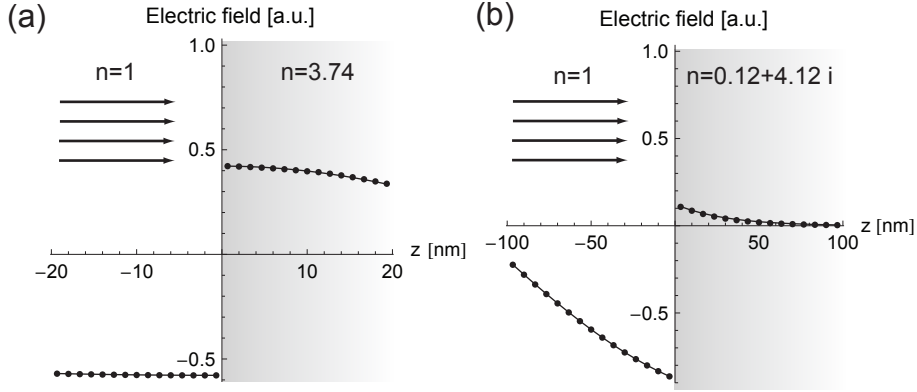


Figure 2.5: Plane wave scattering at normal incidence on a single infinite planar interface between air and a dielectric medium with refractive index  $n$  [(a) high permittivity dielectric (b) metal]. The density of DOFs is approximately  $0.02 \text{ DOF}\cdot\text{nm}^{-2}$ . The real part of the instantaneous scattered electric field is shown as a function of the coordinate  $z$  normal to the plane. Lines: analytical solution; dots: numerical results.

density of degrees of freedom required to reach a given level of accuracy is comparable (for 2% error, approximately  $0.009 \text{ DOF}\cdot\text{nm}^{-2}$  in Ref. [81] for a dielectric sphere, and approximately  $0.006 \text{ DOF}\cdot\text{nm}^{-2}$  in our case for an incidence wavelength of  $600 \text{ nm}$ ). This shows that the SIE/PMCHWT formulation presented here has the same accuracy as that presented in Ref. [81] for individual scatterers. In most cases, the density of DOFs will be chosen between  $0.04$  and  $0.06 \text{ DOF}\cdot\text{nm}^{-2}$ .

In Figure 2.5, the scattering of a plane wave impinging normally on a single planar infinite interface between air and a dielectric medium is investigated. The cases of a high permittivity dielectric [Fig. 2.5(a)] and a metal [Fig. 2.5(b)] are considered. The real part of the scattered field on both sides of the interface is computed and compared with the analytical solution. Thanks to the singularity subtraction technique, very good agreement is obtained arbitrarily close to the interface, without any trace of the discretization.

### 2.3.2 Photonic crystal

The reflection properties of a square array of pillars with refractive index  $n = 3.36$  as a function of the incident wavelength  $\lambda$  are investigated in Fig. 2.6. The periodic Green's function is evaluated with 9 terms in the Ewald sum. The linear system of equations is also solved with LU decomposition. From Eq. (2.19) the intensity of the scattered electric field is calculated  $50 \mu\text{m}$  above the array on the incidence side and normalized to the intensity of the incident plane wave, yielding the reflectance of the system. For both the square [Fig. 2.6(b)] and the hexagonal [Fig. 2.6(c)] arrays, a very high reflectance between  $\lambda = 340 \text{ nm}$  and  $\lambda = 460 \text{ nm}$  is observed, indicating the position

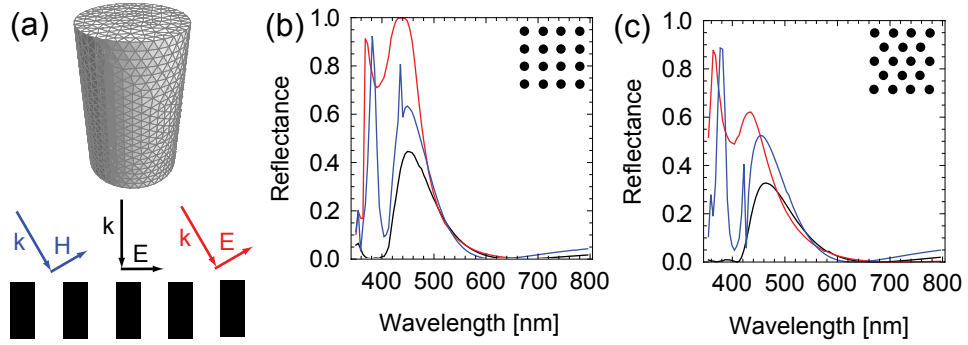


Figure 2.6: Reflection properties of a photonic crystal of dielectric pillars of refractive index 3.36. (a) Geometry and discretization of a single pillar with diameter 100 nm and height 200 nm. The mesh finesse is  $0.076 \text{ DOFs}\cdot\text{nm}^{-2}$ . (b) Reflectance of a square array with period 200 nm. (c) Reflectance of an hexagonal array with period 200 nm. (b–c) Black: normal incidence; red:  $30^\circ$  s-polarized incidence; blue:  $30^\circ$  p-polarized incidence.

of a full photonic band-gap. However, a normal incidence wave is less reflected due to the finite thickness of the array. For larger wavelengths the system is almost transparent [Figs. 2.6(b) and 2.6(c)]. In order to confirm the validity of these results, canonical tests of energy conservation and reciprocity are performed. The first of them is energy balance. The time-averaged Poynting vector

$$\mathbf{P} = \frac{1}{2} \mathbf{E} \times \mathbf{H}^*, \quad (2.51)$$

is evaluated in post processing. For any surface  $S$  which encloses no scatterer made of a lossy material nor a source current, it must satisfy

$$F_E = \oint dS \hat{n} \cdot \mathbf{P}(\mathbf{r}) = 0, \quad (2.52)$$

where  $\hat{n}$  is the surface outward pointing normal vector. The surface  $S$  has been chosen here to be a rectangular box of section  $\Omega$  and height  $50\mu\text{m}$  centered around a pillar. As periodic boundary conditions have been chosen for the Green's function, the energy balance is automatically satisfied on the sides of  $S$ . Therefore, the flux  $F_E$  can be evaluated only on surfaces parallel to the array. The second test involves reciprocity. Let  $\mathbf{E}_1$  and  $\mathbf{H}_1$  denote the scattered electric and magnetic fields of a given diffraction problem. Consider another diffraction problem by choosing a propagating reflected order of the first problem and returning an incident field of the same wavelength along the direction of this outgoing order. The scattered electric and magnetic fields of the second problem are denoted  $\mathbf{E}_2$  and  $\mathbf{H}_2$ . Considering again a surface  $S$  enclosing the array,

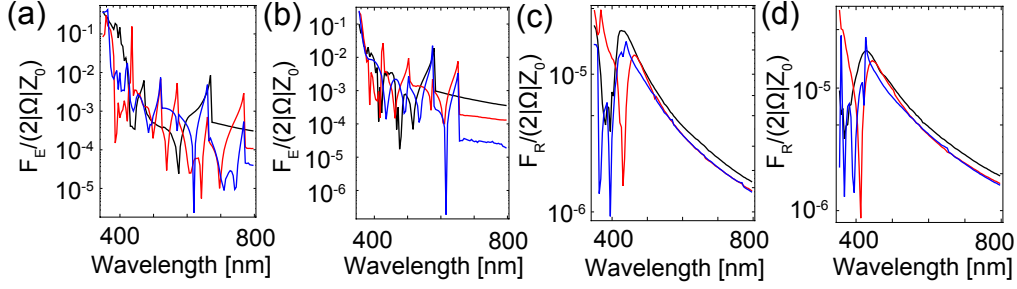


Figure 2.7: (a) Test of energy conservation for a photonic crystal with square periodicity and (b) with hexagonal periodicity with the geometry and incidence conditions of Fig. 2.6. (c) Test of reciprocity for a photonic crystal with square periodicity and (b) with hexagonal periodicity. Black: normal incidence; blue:  $p$  polarized  $45^\circ$  incidence; red:  $s$ -polarized  $45^\circ$  incidence.

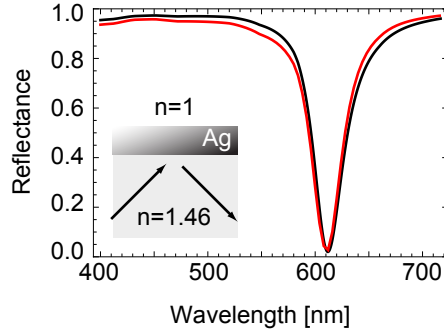


Figure 2.8: Plane wave excitation at  $45^\circ$  incidence with  $p$ -polarization on a 50 nm silver thin film. Experimental data for the silver permittivity of silver are taken from experimental data [102]. Black: reflectance obtained from transfer matrix calculations, red: reflectance obtained from the SIE method with a mesh finesse of  $0.03 \text{ DOF} \cdot \text{nm}^{-2}$ .

reciprocity implies:

$$F_R = \oint dS \hat{n} \cdot (\mathbf{E}_1 \times \mathbf{H}_2 - \mathbf{E}_2 \times \mathbf{H}_1)(\mathbf{r}) = 0. \quad (2.53)$$

We have chosen the 0th order transmitted wave as the second diffraction problem. The total fluxes  $F_E$  and  $F_R$  are numerically non-zero and have been normalized to  $2|\Omega|Z_0$ , where  $Z_0$  is the free space impedance. From Fig. (2.7), the error is exponentially decreasing with increasing wavelength for a constant mesh finesse for both the energy conservation and the reciprocity test, because the mesh becomes able to better render the oscillations of the field.

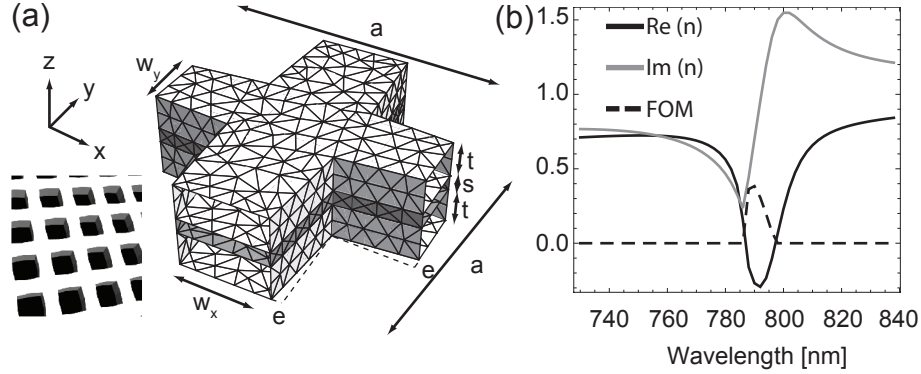


Figure 2.9: (a) Geometry of the metamaterial unit cell (1352 mesh triangles): period  $a = 300$  nm, Ag layer thickness  $t = 40$  nm,  $\text{MgF}_2$  layer thickness  $s = 17$  nm, deviation from rectangular shape  $e = 8$  nm, width  $w_x=102$  nm and  $w_y=102$  nm. Inset: three-dimensional view of the array. (b) Metamaterial effective refractive index  $n$  as a function of the wavelength: real, imaginary parts and figure of merit  $\text{FOM} = -\text{Re}(n)/\text{Im}(n)$ . The FOM is set to zero if  $\text{Re}(n)$  is positive.

### 2.3.3 Asymmetric metallic film

In Figure 2.8, the propagating surface plasmon of a thin asymmetric silver film is excited. The reflectance computed with SIE method is compared to transfer matrix calculations and good agreement is observed with a reasonable mesh finesse. This shows its capability to provide results with high accuracy even in the extreme conditions of the the excitation of a surface plasmon, thanks to the PMCHWT formulation.

### 2.3.4 Negative-index metamaterial

We compare in this section the results of our method to the published results of Dolling *et al.* [103], where they experimentally and numerically demonstrate a negative-index metamaterial operating around  $\lambda = 780$  nm. The geometry shown in Fig. 2.9(a) and materials are directly taken from Ref. [103]. The metamaterial is made from a Ag– $\text{MgF}_2$ –Ag multilayer. The refractive index of  $\text{MgF}_2$  is 1.38, and Drude model with plasma frequency  $1.37 \times 10^{16} \text{s}^{-1}$  and damping  $9 \times 10^{13} \text{s}^{-1}$  is taken for silver. The incident plane wave is  $p$ -polarized with the propagation vector in the  $x$ - $z$  plane, making an angle of  $6^\circ$  with the normal to the array. In order to retrieve the effective refractive index, a homogeneous film with a thickness, complex transmission and reflection coefficients identical to those of the metamaterial is considered [104]. Very good agreement with the results of Ref. [103] is obtained in Fig. 2.9(b), showing a negative effective refractive index of the metamaterial for wavelengths between 786 nm and 796 nm. The index reaches -0.3 at 790 nm, for a figure of merit of 0.4. This illustrates that relatively complex periodic geometries including different materials can be accurately simulated with the technique

described in this chapter.

### 2.4 Conclusion

In this chapter, a surface integral formulation for light scattering by periodic structures has been developed. The electric field and magnetic field equations on the scatterers surfaces in the unit cell with periodic boundary conditions have been derived and their numerical implementation detailed into two main steps: the evaluation of the periodic Green's function with Ewald's method and the numerical solution with the method of moments. By implementing a singularity subtraction technique, all occurring singular integrals can be computed analytically and the remaining non-singular parts computed numerically. This provides an accurate description of the electromagnetic field even at very short distances from the scatterer surface.

The convergence of the method has been tested using canonical tests from grating theory. For an infinite interface between different media, the numerical and analytical solutions have been compared in the extreme near-field and far-field, showing very good agreement. For a photonic crystal of dielectric pillars with square and hexagonal periodicities, the energy conservation and reciprocity have been tested as a function of the incident wavelength. The optical properties of a propagating plasmon on a thin metallic film have also been compared to transfer matrix calculations. As a final illustration of the technique, the refractive index of a fishnet metamaterial has been calculated and a negative refractive index in the near infrared region of the optical spectrum has been retrieved, in good agreement with published experimental data.

With this versatile formulation, a very large variety of geometries can be simulated, including two-dimensional arrays of individual nanostructures on a substrate or in multilayered backgrounds, which is a situation often encountered in experimental nanophotonics. The surface discretization provides a high flexibility, allowing the investigation of irregular shapes. Another advantage of the formulation is that it can give insights into the extreme near-field of the scatterers, while providing at the same time the corresponding far-field. The technique developed in this chapter will be extensively used in Chapters 3 and 4 to investigate plasmonic systems that exhibit Fano resonances.



# 3 Mechanisms of plasmonic Fano resonances

In this chapter, the mechanisms of plasmonic Fano resonances discussed in Chapter 1 are illustrated by analyzing the near-field and the far-field of different nanostructures using surface integral computations. Part of this work is published in Refs. [105] and [106]. In Section 3.1, the influence of the interactions between the resonant mode and the continuum of radiative waves onto the line shape of the optical response and the resonance parameters will be studied. In Section 3.2, the behavior of the electromagnetic field at the vicinity of the nanostructures will be linked to the far-field response.

## 3.1 Effects of electromagnetic interactions on the line shape

In Chapter 1, an electromagnetic model of Fano resonances has been developed. The main analytical results that have been derived and the definitions that have been introduced are now recalled to facilitate the following discussion. Fano-like resonances are built from the interference between a continuum of radiative waves and a non-radiative (dark) mode that spectrally and spatially overlap. Two pathways have to be considered: the direct excitation of the continuum and the excitation and reemission of the dark mode through its coupling to the continuum. The frequency dependent phase difference between the direct and indirect pathways leads both to a destructive and a constructive interference at the origin of the asymmetric nature of the resonance (Figs. 3.1 and 3.2). The type of interference also depends on the scattering angle and therefore on the observable that is chosen to monitor the resonance. For example, a constructive interference in reflection corresponds to a destructive interference in transmission due to energy conservation. The dielectric permittivity of metals, and consequently the dark mode resonance frequency  $\omega_d + i\gamma_d$ , have an imaginary part accounting for intrinsic losses: in this case, the phase difference between the direct and indirect pathways does not lead to a complete destructive or constructive interference since some energy is absorbed in the metal through the indirect pathway [Fig. 3.2(d)].

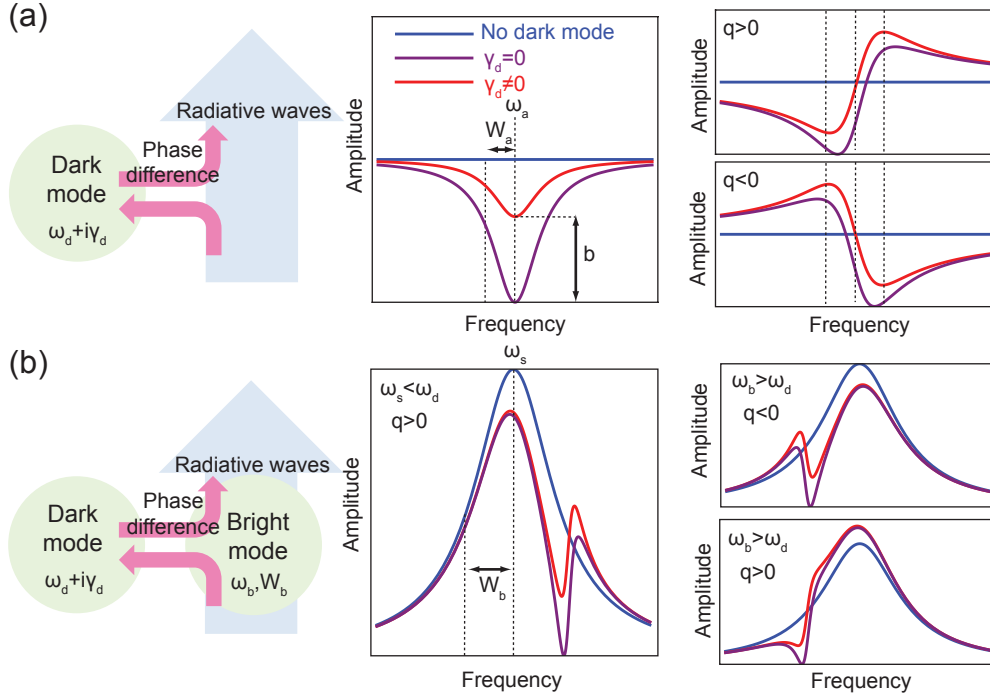


Figure 3.1: (a) Mechanism of Fano-like interferences between a resonant dark mode with complex resonance frequency  $\omega_d + i\gamma_d$  and a flat continuum of radiative waves. Two pathways have to be considered: the direct excitation of continuum and the excitation of the dark mode through its coupling to the continuum. The frequency-dependent phase difference between the direct and indirect pathways leads both to a destructive and a constructive interference. The resulting line shape modulates the continuum and satisfies Eq. (3.2), with  $\omega_a$  the Fano-like resonance frequency,  $W_a$  its spectral width,  $q$  the asymmetry parameter and  $b$  the modulation damping parameter. (b) Fano-like interference between a resonant dark mode and a bright mode with an amplitude satisfying Eq. (3.4) with resonance frequency  $\omega_b$  and spectral width  $W_b$ .

The width of the resonance is the sum of two contributions:  $\Gamma = \Gamma_i + \Gamma_c$ , where  $\Gamma_i$  is associated to the energy converted to heat by intrinsic losses in the metallic structures and  $\Gamma_c$  to radiative losses by coupling to the continuum. The resonance is located at a frequency

$$\omega_a^2 = \omega_d^2 + \omega_d \Delta, \quad (3.1)$$

where  $\Delta$  is the shift from the original dark mode resonance frequency  $\omega_d$ . The interference between the two pathways induces a spectral response satisfying the following asymmetric

### 3.1. Effects of electromagnetic interactions on the line shape

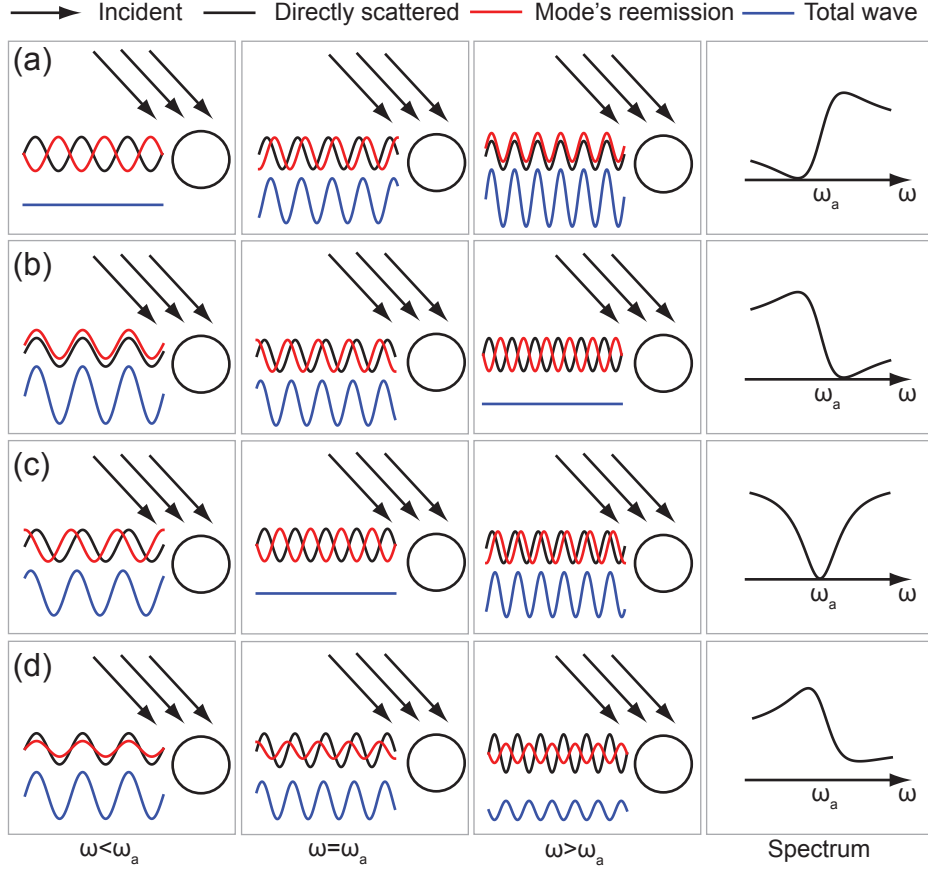


Figure 3.2: Mechanism of Fano interference between a resonant mode and a continuum of scattered waves. Around the resonance frequency  $\omega_a$ , the dark mode shifts its phase by  $\pi$ . The phase dependence of the mode reemission induces destructive or constructive interference, resulting in an asymmetric response. (a)  $q > 0$  and  $b = 0$ , (b)  $q < 0$  and  $b = 0$ , (c)  $q = 0$  and  $b = 0$ , (d)  $q < 0$  and  $b \neq 0$ .

analytical function:

$$\sigma_a(\omega) = \frac{\left(\frac{\omega^2 - \omega_a^2}{\Gamma} + q\right)^2 + b}{\left(\frac{\omega^2 - \omega_a^2}{\Gamma}\right)^2 + 1}, \quad (3.2)$$

where  $q$  is the asymmetry parameter and

$$b = \frac{\Gamma_i^2 / \Gamma_c^2}{(1 + \Gamma_i / \Gamma_c)^2} \quad (3.3)$$

is the modulation damping parameter. We define  $W_a$  as the resonance width in frequency units by  $\Gamma = 2W_a\omega_a$ . If the asymmetry parameter  $q = 0$ , the resonance is symmetric and appears as a dip in the spectrum with minimal value  $\sigma(\omega_a) = b$ . The quantity  $W_a$  is

### Chapter 3. Mechanisms of plasmonic Fano resonances

---

defined such that  $\sigma(\omega_a \pm W_a) \simeq (1 + b)/2$  for  $W_a \ll \omega_a$ , where  $(1 + b)/2$  is the average value between the modulation minimum and its asymptotic value.

The continuum of radiative waves can be constructed from the radiative (bright) mode of a plasmonic nanostructure [Fig. 3.1(b)]. The bright mode resonance strength follows the following symmetric pseudo-lorentzian line shape as a function of the frequency  $\omega$ :

$$\sigma_b(\omega) = \frac{a^2}{\left(\frac{\omega^2 - \omega_b^2}{\Gamma_b}\right)^2 + 1}, \quad (3.4)$$

where  $a$  is the maximum amplitude of the resonance,  $\omega_b$  the resonance frequency and  $\Gamma_b$  its width. We define  $W_b = \Gamma_b/(2\omega_b)$  as an approximation of its spectral width in frequency units for  $W_b \ll \omega_s$ . The quantity  $W_b$  gives an approximation of the resonance spectral width and is expressed in frequency units. The symmetric resonance (SR) given by Eq. (3.4) builds a continuum supporting a Fano-like resonance (also called superradiant envelope [39]). The structure generating the SR is placed in close vicinity of another one supporting the dark mode [26, 37, 39]; alternatively, one can also use the strong coupling of two modes hybridizing into a bright and a dark modes [42, 107–110]. The resonance strength of the entire system represents the measurable quantity and is given by the product of the SR  $\sigma_s$  line shape [3.4] with the asymmetric resonance (AR) line shape [Fig. 3.1(b)]:

$$\sigma_{\text{tot}}(\omega) = \sigma_b(\omega)\sigma_a(\omega). \quad (3.5)$$

The analytical function  $\sigma_{\text{tot}}$  can be used to fit various theoretical or experimental spectra including *e.g.* reflectance, transmittance, extinction, absorbance, radar backscattering, forward scattering or total cross section. In the case of a dark-bright modes interaction, the frequency shift  $\Delta$  and asymmetry parameter  $q$  become:

$$\Delta = \frac{\gamma_d^2}{\omega_d} \pm \frac{\omega_d}{2\Gamma_b^2} \Gamma_c (\omega_d^2 - \omega_b^2), \quad q = \pm \frac{\omega_d^2 - \omega_b^2}{2\Gamma_b(1 + \Gamma_i/\Gamma_c)}. \quad (3.6)$$

where the  $\pm$  sign is determined by the phase of the directly scattered field. Two different situations of dark-bright modes interactions can be distinguished: in Section 3.1.1, the two modes are supported by two different nanostructures, which makes them separable, whereas in Section 3.1.2, the interaction between two hybridized modes supported by the same nanostructure, and therefore inseparable, is discussed. The first reported historical case of Fano resonances is finally discussed in Section 3.1.3: the excitation of the first orders in metallic gratings.

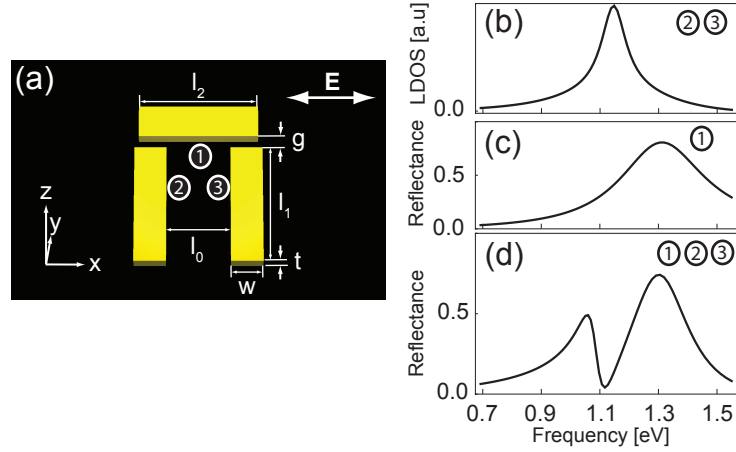


Figure 3.3: Structural decomposition of a Fano resonance in a dolmen-type plasmonic structure in air: beam 1 supports a radiative dipolar mode, whereas beams 2 and 3 support a non-radiative quadrupolar mode. (a) Structure dimensions:  $w = 40$  nm,  $l_0 = 160$  nm,  $t = 80$  nm,  $g = 30$  nm and  $l_1 = l_2 = 300$  nm. The dolmens material is chosen to satisfy a Drude model with plasma frequency  $\omega_p = 1.37 \times 10^{16} \text{s}^{-1}$  and damping  $\gamma = 0.009\omega_p$ , describing the dielectric permittivity of gold. (b) Local density of states (LDOS) of a dipole emitter placed 50nm from the end of beam 2 in the absence of beam 1, (c) reflectance of the isolated beam 1, (d) reflectance of the composite system.

### 3.1.1 Separable bright and dark modes

We first consider the example of a dolmen-type plasmonic structure [26, 37, 38], made of three metallic beams arranged as in Fig. 3.3. In the quasistatic approximation, a dark mode cannot be excited by a planewave, but by a rapidly varying field, such as a dipole placed in the near-field of the structure [111]. The local density of states (LDOS), defined as the imaginary part of the Green's tensor at the position of the dipole, provides all the spectral and scattering information for the structure [112]. It is computed in Fig. 3.3(b) at one end of the double beam structure, revealing the existence of a non-radiative quadrupole mode at a frequency  $\omega_d = 1.14$  eV. The dipolar mode of the perpendicular beam has a larger spectral width due to radiative losses and ensures the coupling of the non-radiative mode to the radiative continuum [Fig. 3.3(c)]. In this system, the bright and the dark modes are supported by two separate parts of the complete system. The total reflectance spectra is fitted with Eq. (3.5) by variation of the 7 parameters  $a$ ,  $\omega_b$ ,  $W_b$ ,  $\omega_a$ ,  $W_a$ ,  $q$  and  $b$  [Eqs. (3.2) and (3.4)]. In order to fulfill energy conservation, the SR amplitude  $a$  is constrained to be smaller than 1. Values of the parameters are reported in Table 3.1. The fit is shown in Fig. 3.4(a), along with the individual extracted SR line shape [Eq. (3.4)] and AR line shape [Eq. (3.2)] in Fig. 3.4(b). It has been shown that the field overlap between the two modes plays an important role into the control of the AR width and position, and can be tuned by changing the gap size  $g$ . From Table 3.1, the width of the resonance is strongly influenced by such a variation of the

	$a$	$\omega_b$ [eV]	$W_b$ [eV]	$\omega_a$ [eV]	$W_a$ [eV]	$q$	$b$
Fig. 3.4(a)	1.000	1.284	0.121	1.080	0.034	-0.939	0.304
Fig. 3.4(c)	1.000	1.287	0.120	1.079	0.038	-0.870	0.397
Fig. 3.4(e)	0.934	1.269	0.130	1.117	0.023	-0.373	0.663
Fig. 3.4(g)	1.000	1.248	0.130	1.554	0.025	1.297	0.148
Fig. 3.6(a)	0.836	1.883	0.405	1.383	0.137	0.666	0.267
Fig. 3.6(b)	0.865	1.823	0.334	1.422	0.120	0.594	0.338
Fig. 3.6(c)	0.913	1.565	0.431	1.754	0.130	-0.058	0.183
Fig. 3.6(d) LF	0.921	1.828	0.333	1.196	0.150	0.326	0.775
Fig. 3.6(d) HF				1.962	0.135	0.124	0.363
Fig. 3.7(b)	0.309	1.932	0.028	1.681	0.030	-2.826	1.385
Fig. 3.7(c)	0.289	1.848	0.044	1.670	0.027	-1.096	0.257
Fig. 3.7(d)	0.265	1.812	0.054	1.692	0.021	-0.490	0.258
Fig. 3.7(e)	0.944	1.845	0.044	1.690	0.039	-1.355	0.586
Fig. 3.8(b)	0.149	2.688	0.115	2.870	0.058	1.032	0.135
Fig. 3.9(b)				1.986	0.007	1.493	1.238
Fig. 3.9(c)	1.000	1.547	0.280	2.110	0.014	0.940	0.296

Table 3.1: Value of the different parameters obtained by a fit with 3.5 of the spectra in Figs. 3.4 to 3.9, except for Fig. 3.6(e) and Fig. 3.9(b) (see text).

gap size, going from 0.034 eV for  $g=30$  nm in Fig. 3.4(a) to 0.023 eV for  $g=45$  nm in Fig. 3.4(e). This effect of the coupling to the AR line shape has also been observed in terahertz split ring resonators, where the control of the coupling of the dark mode to the bright mode is performed by symmetry breaking [113]. The increase of the modes coupling, i.e. their field overlap, decreases the time spent for the power transfer through the indirect pathway and results to a spectral broadening of the AR. It is also at the origin of a spectral shift of the AR frequency from the dark mode resonance frequency. Losses engineering is another way of controlling the AR parameters. In Fig. 3.4(c), the Drude damping parameter used for the metal is increased in the beams 2 and 3. As predicted from the electromagnetic theory, intrinsic losses damp the AR and strongly affect the AR width, asymmetry and modulation depth (compare the first and second lines in Table 3.1). A very small shift of the AR frequency is also observed.

The modes coupling has a strong influence on the shape parameters  $q$  and  $b$ . In the presence of intrinsic losses, the interference between the direct and indirect pathways is not total and the Fano modulation is damped. The  $b$  parameter quantifies this effect; it is a function of the ratio between the intensity lost to the metallic structure and the intensity transferred from the bright mode to the dark mode. If the coupling between the two modes is too weak compared to intrinsic losses, almost no modulation is observed. The parameter  $b$  increases from 0.304 for a gap size of  $g=30$  nm [Fig. 3.4(a)] to 0.663 for  $g=45$  nm [Fig. 3.4(e)]: this provides a quantitative description of a phenomenon that has been observed in previous works on dolmen nanostructures [25, 37]. An increase

### 3.1. Effects of electromagnetic interactions on the line shape

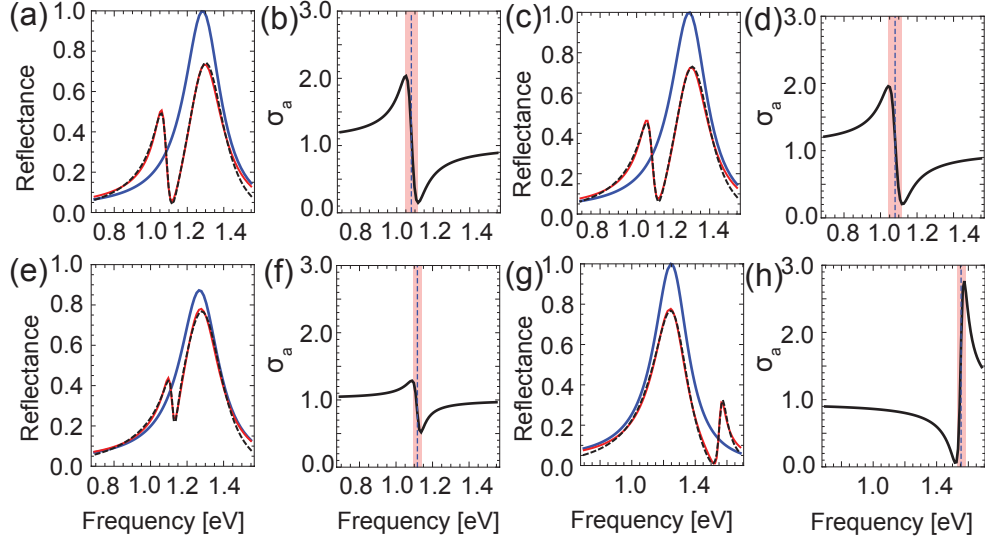


Figure 3.4: Influence of electromagnetic interactions on the resonance line shape of dolmen nanostructures. Reflectance of dolmen plasmonic nanostructures is calculated for a normal illumination with  $x$ -polarized electric field: (a–b) geometry of Fig. 3.3. (b–c) modified Drude damping  $\gamma = 0.009\omega_p$  for beams 2 and 3, (d–e) modified gap size  $g = 45$  nm, (f–g) modified gap size  $g = 45$  nm and length of the beams 2 and 3  $l_1 = 200$  nm. (a), (c), (e) and (g): black dashed–numerical simulations; red thick–fit with  $\sigma_{\text{tot}}$  [3.5]; blue thin–background resonance  $\sigma_b$  extracted from the fit [Eq. (3.4)]; (b), (d), (f) and (h): respective asymmetric line shapes  $\sigma$  extracted from the fit [Eq. (3.2)]; the blue dashed line and red rectangle show respectively the resonance frequency  $\omega_a$  and width  $W_a$ .

of the parameter  $b$  is also observed with an increase of the intrinsic losses [Fig. 3.4(c)]. The parameter  $b$  determines the maximal amount of light that can be transmitted and is therefore critical for achieving the plasmonic equivalent of electromagnetically induced transparency [26]. The absolute value of the asymmetry parameter  $q$  also depends on the ratio between the intensity lost to the metallic structure and the intensity transferred from the bright mode to the dark mode: from Table 3.1, it decreases from 0.939 to 0.373 when the gap size increases from 30 nm to 45 nm. The sign of the asymmetry parameter is determined by the frequency difference between the dark and the bright mode. In Fig. 3.4(g), the length of the beams 2 and 3 is shortened from 300 nm to 200 nm, resulting in a blue-shift of the dark mode resonance frequency. As a consequence, the AR frequency is shifted from 1.117 eV to 1.554 eV, and the asymmetry parameter flips its sign from -0.373 to 1.297. This can also be easily observed from the curves shape: in Fig. 3.4(a), the AR consists of a local maximum at low energies, followed by a local minimum, while the opposite happens in Fig. 3.4(g). The phase shift of the bright mode around its resonance frequency flips the conditions of destructive or constructive interference and consequently of the asymmetry parameter (Fig. 3.2).

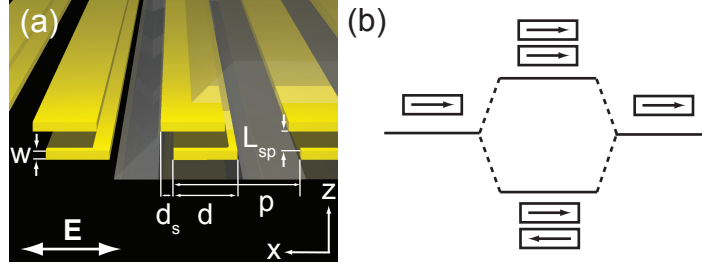


Figure 3.5: (a) Plasmonic double grating with grating separation  $L_{sp}$  and symmetry breaking  $d_s$ . The other structure dimensions are  $d = 100\text{nm}$ ,  $p = 200\text{nm}$  and  $w = 15\text{nm}$ . The wires are made of gold (data from Johnson and Christie [102]) and embedded in a silica matrix (refractive index 1.46). (b) Hybridization scheme of the metallic double grating. If two individual bars supporting a dipolar plasmon mode are strongly coupled, the resulting structure supports a high energy symmetric mode and a low energy antisymmetric mode.

### 3.1.2 Plasmon hybridization and Fano resonances

Let us now consider geometries where the bright and dark modes cannot be assigned to separate entities. In the metallic double grating structure in Fig. 3.5, the individual plasmon modes of each metallic wire hybridize to a symmetric mode with high energy and an antisymmetric mode with low energy [107, 114]. The high energy mode has a strong dipole moment whereas the two dipoles pointing in opposite directions of the low energy mode induce a vanishing dipole moment. The antisymmetric mode is therefore dark. As discussed in Chapter 1, in plasmonics the linear operator equivalent to the quantum Hamiltonian is not hermitian, its eigenvalues are not real and its eigenmodes not orthogonal. As a result, the hybridization process of Fig. 3.5(b) is not ideal and the two hybridized modes are also not completely orthogonal in the symmetric configuration. The small field overlap between the two modes is sufficient to induce a weak coupling and the appearance of a Fano resonance. The offset  $d_s$  between the two wires introduces a symmetry breaking in the structure which can be used to tune the resonance frequency of the two modes [107, 114]. The parameters used for fitting the reflectance spectra are reported in Table 3.1. For the bright mode, charges of identical sign are moved further apart by the symmetry breaking, resulting in a red-shift of the SR [from 1.883 eV to 1.565 eV in Fig. 3.6(a) to (c)]. On the other hand, for the dark mode the symmetry breaking brings charges of identical sign closer to each other, resulting in a blue-shift of the AR [from 1.42 eV to 1.75 eV in Fig. 3.6(a) to (c)]. The reduction of the modes detuning makes the AR shape more symmetric. When the wires are brought close to each other so that  $L_{sp} = 10\text{ nm}$ , the AR energy shifts from 1.42 eV to 1.19 eV because charges of opposite sign are brought close to each other; the inverse shift is observed for the bright mode. Furthermore, an additional AR appears for  $d_s = 20\text{ nm}$  at 1.96



### 3.1. Effects of electromagnetic interactions on the line shape

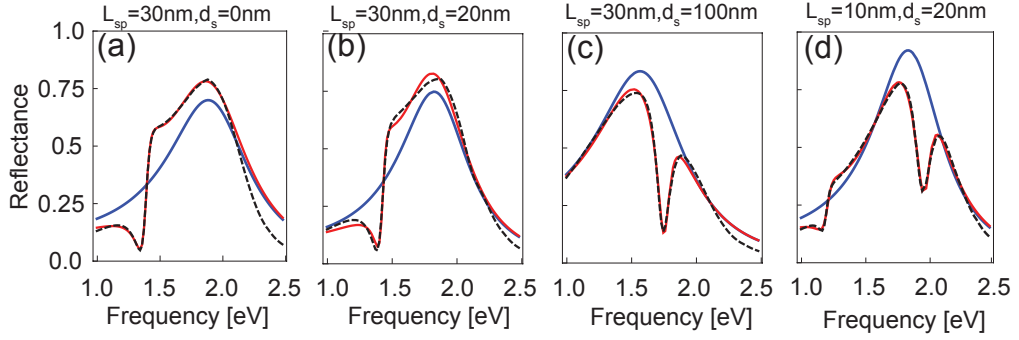


Figure 3.6: Reflectance of the plasmonic double grating of Fig. 3.5 for varying gratings separation  $L_{sp}$  and symmetry breaking  $d_s$  at normal incidence. (a–d) Black dashed–numerical simulations; red thick–fit with  $\sigma_t$  [Eq. (3.5)]; blue thin–background resonance  $\sigma_s$  extracted from the fit [Eq. (3.4)]. In (d), two resonances of different order occur, labeled as Low Frequency (LF) and High Frequency (HF), in which the quadrupolar and octupolar modes are respectively excited.

eV [Fig. 3.6(d)], resulting from the interference between an octupolar mode and the dipolar mode [107]. Four additional parameters have been added to the fit in order to take this higher order AR into account. In Fig. 3.6(a) to (d), the sign of the asymmetry parameter is positive even though the AR is located on the low frequency shoulder of the SR. This sign reversal is due to the antisymmetric nature of the dark modes with respect to the  $z = 0$  plane [Fig. 3.5]. The phase difference between the direct and indirect pathways is opposite to the phase difference induced by a  $z$ -symmetric dark mode, and as a consequence so is the sign of the asymmetry parameter (Fig. 3.2).

Plasmonic oligomers – such as the quadrumer shown in Fig. 3.7(a) – use the hybridization of a circular chain of nanoparticles with a central nanoparticle to produce a dark and a bright mode, whose interference gives rise to a Fano-like resonance [115, 116]. Due to the metallic character of the particles, the dark and bright modes are not completely orthogonal. Note that their coupling and the subsequent generation of the Fano resonance does not require a structural symmetry breaking. In the bright mode configuration, the central particle is in phase with the outer ring particles whereas in the dark mode configuration, the central particle is out of phase, reducing the overall dipole moment of the structure. A structure supporting such modes with a minimal amount of nanoparticles is a quadrumer whose outer ring is composed of three particles and carries the symmetry  $D_{3h}$  (or  $C_{3v}$  if placed on a substrate) as shown in Fig. 3.7.

The reflectance of plasmonic quadrumers placed in an array is calculated in Fig. 3.7(b), (c) and (d) for separation distances between the central particle and the outer ring of 25 nm, 55 nm and 70 nm, respectively. The electric field distribution in the structure at the AR frequency shows that the central particle oscillates out of phase with the exterior particles, therefore reducing the overall dipole moment [116]. The bright mode

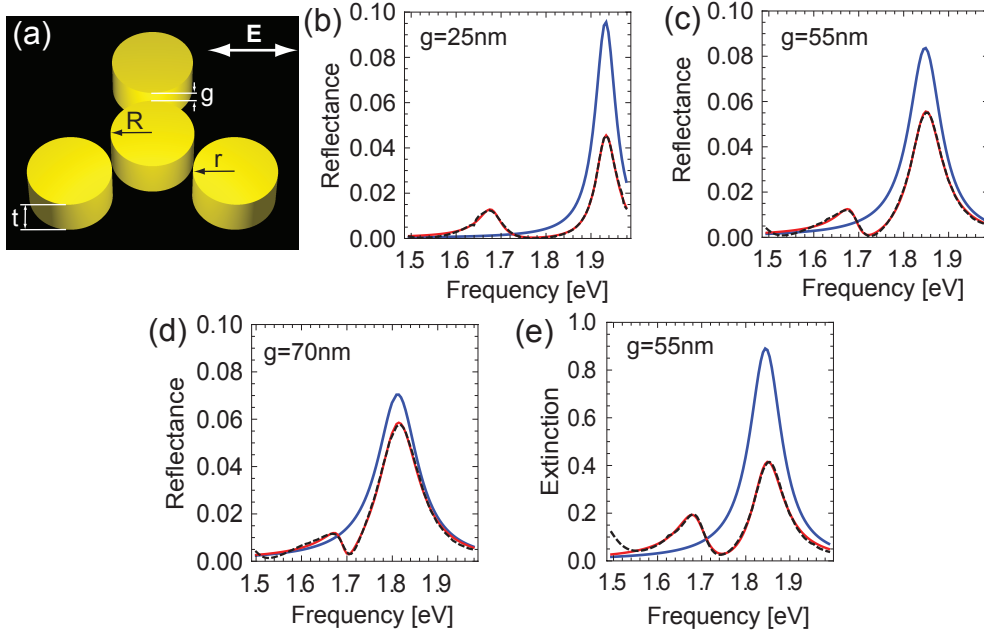


Figure 3.7: Optical properties of gold quadrumers. (a) Geometry and surface discretization of the unit cell with dimensions  $R = 80\text{nm}$ ,  $r = 75\text{nm}$  and  $t = 80\text{nm}$ . The quadrumers are made of metal with Drude model with plasma frequency  $\omega_p = 1.37 \times 10^{16}\text{s}^{-1}$  and damping  $\gamma = 4.08 \times 10^{13}\text{s}^{-1}$ , placed in a two-dimensional array of period  $1400\text{ nm}$ , and embedded in a dielectric background of refractive index  $1.25$ . (b)–(d) Reflectance and (e) extinction at normal incidence. (b–e) Black dashed—numerical simulations; red thick—fit with  $\sigma_{\text{tot}}$  [Eq. (3.5)]; blue thin—background resonance  $\sigma_b$  extracted from the fit [Eq. (3.4)].

is relatively narrow, but its spectral overlap with the AR ensures the validity of Eq. (3.5). Since the two modes interfering to produce a Fano-like resonance are supported by the same structure, the SR background cannot be explicitly computed. Nevertheless, the fit of the total spectrum enables the extraction of the SR for both reflection and extinction [blue curves in Fig. 3.7(b) to (e)] in the same way as in Fig. 3.4 and Fig. 3.4. Similarly to the dolmen nanostructure, an increase of the gap  $g$  leads to a decrease of the field overlap between the two modes and consequently of the AR width (Table 3.1). This suggests that the bright mode resembles the resonance of the same structure without the central particle [116]. The asymmetry parameter has a relatively large absolute value compared to the other structures investigated in this chapter, so that the overall optical response has the appearance of two distinct peaks [Fig. 3.7(b), (c) and (d)]. In the extinction spectrum of Fig. 3.7(e), similar results for the spectral positions and width of the SR and AR are obtained, but the asymmetry parameter is even larger, resulting in an even more pronounced peak of the AR [for infinitely large absolute values of  $q$ , the AR is given by a lorentzian, see Eq. (3.2)]. This drastic change of  $q$  and  $b$  when comparing the reflectance and the extinction spectra of the same structure under the same illumination conditions, shows that these two parameters depend not only on the near-field interactions between

### 3.1. Effects of electromagnetic interactions on the line shape

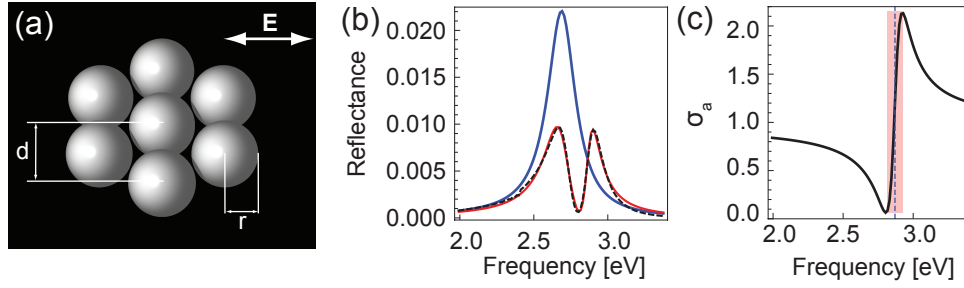


Figure 3.8: Reflectance of a two-dimensional array of heptamers of spherical nanoparticles at normal incidence. (a) Geometry of a single structure with dimensions  $r = 30\text{nm}$  and  $d = 65\text{nm}$ . The heptamers are separated by a period of  $900\text{ nm}$  and placed in vacuum. Experimental data for silver has been taken for the particles material [102]. (b) Black dashed—numerical simulations; red thick—fit with  $\sigma_{\text{tot}}$  [Eq. (3.5)]; blue thin—background resonance  $\sigma_b$  extracted from the fit [Eq. (3.4)]. (c) Respective asymmetric line shapes  $\sigma$  extracted from the fit [Eq. (3.2)]; the blue dashed line and red rectangle show respectively the resonance frequency  $\omega_a$  and width.

the bright and dark modes, but also on how the resonance is monitored (see for instance Babic *et al.* [117]). This fact has been observed for the case of Mie scattering of a metallic sphere [14, 118]: the dipolar and quadrupolar modes of the sphere interfere together to form a Fano resonance in the vicinity of the quadrupolar mode resonance frequency. In this case, the  $q$  parameter reverses its sign depending whether a forward or backward scattering cross section is considered.

For the quadrumers, a vectorial symmetry analysis shows that in-plane dipolar modes are always two-fold degenerate [111, 119]. The dark mode of the quadrumer structure is also degenerate. Hence the two degenerate bright modes and the two degenerate dark modes produce to degenerate Fano resonances at the same frequency, the degeneracies related to the two different polarizations.

A Fano-like resonance can be found in plasmonic oligomers with a higher number of surrounding particles, such as heptamers [110, 115]. In Fig. 3.8, we consider an arrangement of seven silver spheres. From Table 3.1, the AR appears larger with this geometry than the other cases treated in this work, but it has, on the other hand, the lowest value of  $b$ . This quantitatively illustrates that the line shape almost reaches zero with a very large modulation depth. Plasmonic heptamers show a high degree of tunability by controlling the spacing, shape and dimensions of the particles, and the various ways of breaking its high symmetry [110, 115, 116]. How the variation of these parameters affect the shape of the AR can be quantified following the same procedure, provided that no radiative channel for the dark mode is open. The heptamer structures carry the high symmetry  $D_{6h} = C_s \otimes C_{6v}$ . Similarly to the quadrumers with  $D_{3h}$  symmetry, the bright and dark modes are two-fold degenerated. A similar resonance is obtained for the

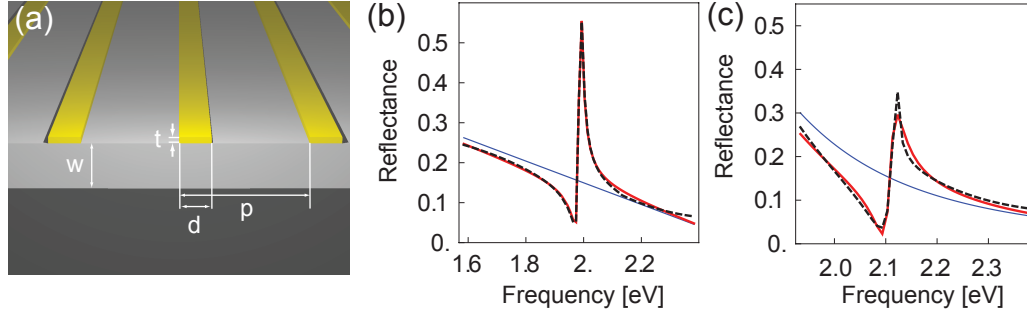


Figure 3.9: Reflectance of a planar metallic photonic crystal structure at normal incidence. (a) The structure dimensions are  $t = 20\text{nm}$ ,  $d = 100\text{nm}$ ,  $p = 400\text{nm}$  and  $w = 140\text{nm}$ . (b) TE illumination (electric field parallel to the gold wires). (c) TM illumination (electric field perpendicular to the gold wires). Black dashed-numerical simulations; red thick-fit with  $\sigma_t$  [3.5]; blue thin-background resonance  $\sigma_s$  extracted from the fit [3.4].

orthogonal polarization. Hence, contrary the other structures investigated in this chapter, plasmonic oligomers are able to generate quasi-isotropic Fano resonances [110, 115, 116].

### 3.1.3 Excitation of first orders in metallic photonic crystals

The Fano resonance is also supported by periodic metallic crystals [120]. In Fig. 3.9, the reflectance spectra of an array of gold nanowires placed on a single-mode slab waveguide is calculated for both polarizations at normal incidence. The metallic grating on top is made of gold (data from Johnson and Christie [102]), the waveguide layer of ITO (refractive index 1.9), and the substrate of quartz (refractive index 1.46). In Fig. 3.9(b), the excitation of TE quasi-guided modes induces an AR. Another waveguide mode is excited through the grating for a TM polarization in Fig. 3.9(c). For TE polarization, the background is not created from a plasmon resonance [121], and has been fitted with the function of the frequency  $\sigma_s(\omega) = g\omega + h$ , corresponding to a Taylor expansion of the background profile around the AR frequency: with such a procedure, one can fit a Fano-like resonance with any background by considering its local behaviour in a small frequency interval. Let us also stress that this spectrum cannot be fitted with the original Fano formula ( $b = 0$ ). Indeed, the substrate can induce a phase shift between the direct and indirect pathways that is different from an homogeneous medium and the model of a real  $q$  parameter is not valid anymore [117]. In this case, the modulation damping parameter also contains contributions from the imaginary part of  $q$ . The value of the AR parameters are reported in Table 1 together with  $g = -0.27 \text{ eV}^{-1}$  and  $h = 0.70$ . The frequency window used for the fit is robust: the parameters remain identical up to the second digit. In TM polarization, the individual metallic wires support a plasmon resonance at lower frequency, and the coupling between plasmon and waveguide modes can form waveguide plasmon polaritons [120]. In this case, the background can be fitted with Eq. (3.4). With

the dielectric character of the ITO layer chosen in the simulations, the waveguide modes do not have strong intrinsic losses and even a very weak coupling from the metallic grating is sufficient to induce the AR. As a result, the two ARs in Fig. 3.9(b) and (c) are the narrowest with  $W_a = 0.007$  eV and  $W_a = 0.014$  eV, respectively, but do not correspond to a dark mode confined in three directions. It is worth mentioning that the excitation of quasi-guided first order waves from a metallic grating, also known as Wood or Rayleigh anomaly, has been recently unified with the Fano interferences [122, 123], and is at the origin of extraordinary transmission in subwavelength hole arrays [10, 11].

## 3.2 Relation between near-field and far-field

We now discuss how the near-field interactions within different plasmonic nanostructures building a Fano system are related to the far-field response. To this end, we consider the dolmen-type geometry and illumination conditions in Fig. 3.3 and study in the near-field and the far-field the evolution of the system as a function of the illumination frequency [Fig. 3.10(a)]. For calculating the spectrum in Fig. 3.10(b), the electric field is sampled at each frequency on a 5 nm homogeneous grid of points at 1 nm from the nanostructures surface. The surface integral method used calculates the field semi-analytically at positions arbitrarily close to surfaces and therefore does not suffer from numerical inaccuracies [124]. The maximal value of the electric intensity for each frequency is reported in Fig. 3.10(b). The maximal near-field enhancement is found at 1.08 eV, which corresponds exactly to the resonance frequency  $\omega_a$  found from the fit in Fig. 3.4(a). The points of maximal near-field enhancement are located at both top interior corners of the beam pair. Figures 3.10(c) to (i), which show the normalized intensity enhancement and the corresponding polarization charges through the structure, indicate that the quadrupolar mode of the double beam structure is resonantly excited at  $\omega_a$ . The second peak in Fig. 3.10(b) corresponds to the excitation of the bright mode with maximum intensity enhancement found at 1.29 eV, which also corresponds exactly to its resonance frequency  $\omega_b$  found from the fit. The maximum intensity enhancement observed at  $\omega_a$  is about 2.3 times the maximum intensity enhancement observed for the excitation of the bright mode at  $\omega_b$ . In the minimum of the resonance spectrum (around 1.1 eV), the Fano interference opens a narrow transparency window for the incoming light. At this frequency, the maximum intensity enhancement is only about 0.4 times the maximum intensity enhancement observed for the excitation of the dark mode at  $\omega_a$ . This shows that locating the central resonance frequency  $\omega_a$  is a critical point for applications such as refractive index sensing or lasing [14, 20, 125]; this will be discussed in greater details in Chapter 4. In Fig. 3.11(a), the same geometry and illumination conditions are considered, but for a single dolmen instead of an array. It has been shown that due to retardation effects, the quadrupolar mode can be excited under grazing incidence illumination [37]. As the excitation angle  $\theta$  increases, a radiative channel, which was forbidden by the periodic symmetry of the array at normal incidence,

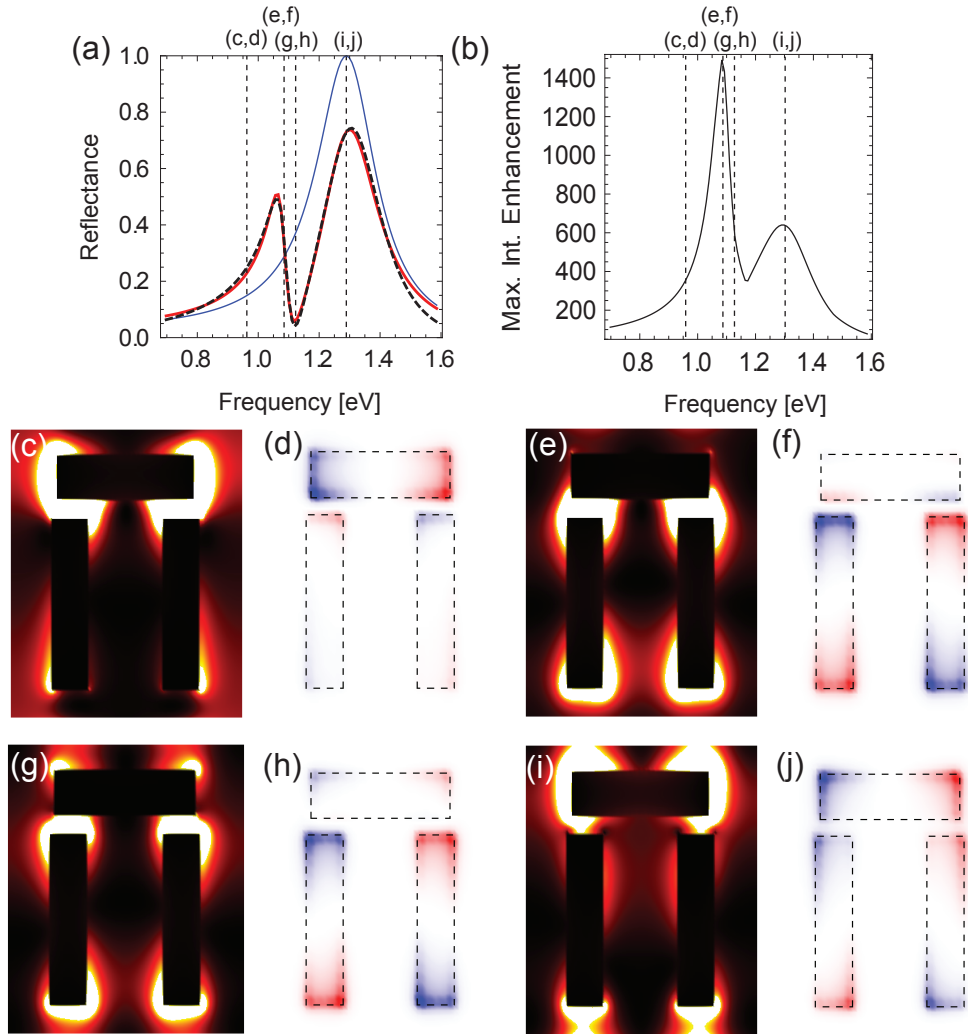


Figure 3.10: (a) Reflectance at normal incidence for an  $x$ -polarized electric field propagating in the  $-z$ -direction, as a function of the illumination frequency. Black dashed line: numerical simulations; thick red solid line: fit with Eq. (3.5); thin blue solid line: bright mode resonance extracted from the fit [Eq. (3.4)], reproduced from Fig. 3.3. (b) Maximum intensity enhancement as a function of the illumination frequency. (c,e,g,i) Near-field behavior Normalized intensity enhancement in a plane through the center of the structure at particular frequencies of the spectra in (a) and (b): black  $\rightarrow$  0 and white  $\rightarrow$  1. (d,f,h,j) Corresponding normalized amplitude of the  $z$ -component of the instantaneous electric field 5 nm above the structure: blue  $\rightarrow$  -1 and red  $\rightarrow$  1.

opens and the reflectance spectrum becomes that of two radiative modes rather than an asymmetric modulation of the radiative mode amplitude. This case does not satisfy the basic assumptions of the electromagnetic theory and the classical oscillators model, both assuming the interference between a radiative and a non radiative channel. In the

### 3.2. Relation between near-field and far-field

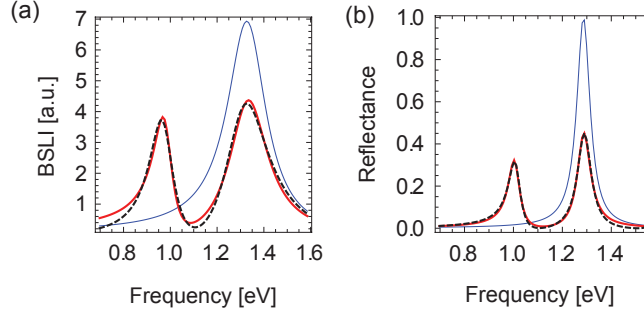


Figure 3.11: (a) Back Scattered Light Intensity (BSLI) of a single dolmen nanostructure with the geometry and illumination conditions of Fig. 3.3. (b) Reflectance of an array of dolmen nanostructures with the geometry and illumination conditions of Fig. 3.3, placed in a two dimensional array of period 800 nm. Black dashed line: numerical simulations; thick red solid line: fit with Eq. (3.5); thin blue solid line: bright mode resonance extracted from the fit [Eq. (3.4)].

geometry of Fig. 3.10 and Fig. 3.11(b), positioning the structures in a subwavelength array suppresses radiation of the quadrupolar mode and ensures that it remains a true dark mode. As a result, the fit of Fig. 3.11(a) (with parameters  $a = 2.63$ ,  $\omega_b = 1.33$  eV,  $W_b = 0.10$  eV,  $\omega_a = 0.98$  eV,  $W_a = 0.05$  eV,  $q = -1.83$ ,  $b = 1.80$ ) is not as satisfying as the fit of Fig. 3.11(b) (with parameters  $a = 1.00$ ,  $\omega_b = 1.29$  eV,  $W_b = 0.03$  eV,  $\omega_a = 1.00$  eV,  $W_a = 0.03$  eV,  $q = -3.88$ ,  $b = 3.75$ ) or the fit of Fig. 3.10(a). This illustrates that in a periodic array, near-field interactions between nearest neighbors have to be taken into account, as will be discussed later.

This interplay between near-field and far-field is also observed in Fig. 3.12 for a metallic double grating structure. The electric field is sampled at each frequency on a 1 nm homogeneous grid of positions at 1 nm from the nanostructures surface. The maximal electric field intensity for each frequency is then reported in Fig. 3.12(b). The maximal intensity in the spectrum of Fig. 3.12(b) is fitted with a lorentzian profile similar to Eq. (3.4). Its central frequency is found at approximately 1.39 eV and has a width of 0.06 eV. These values agree well with the values of  $\omega_a$  and  $W_a$  found from the fit of Fig. 3.12(a). At this frequency, the maximum intensity enhancement is about 16 times that observed for the excitation of the bright mode at  $\omega_s$ , showing that the dark mode is resonantly excited at this frequency. The near-field distribution in Fig. 3.12(c) also indicates a quadrupolar charges configuration in the structure at  $\omega_a$ . The points of maximal near-field enhancement are located at  $(x, z) = (\pm 50, 14)$  nm, i.e. at the two bottom corners of the top nanoparticle. Let us emphasize that it is not possible to determine *a priori* the resonance frequency  $\omega_a$  from a Fano resonance spectrum such as the black dashed curve in Fig. 3.10(a) or in Fig. 3.12(a), since its shape is determined by many parameters and  $\omega_a$  does not correspond to a specific point in the spectrum (for instance a local minimum or maximum). However, the fit with Eq. (3.5) is able to

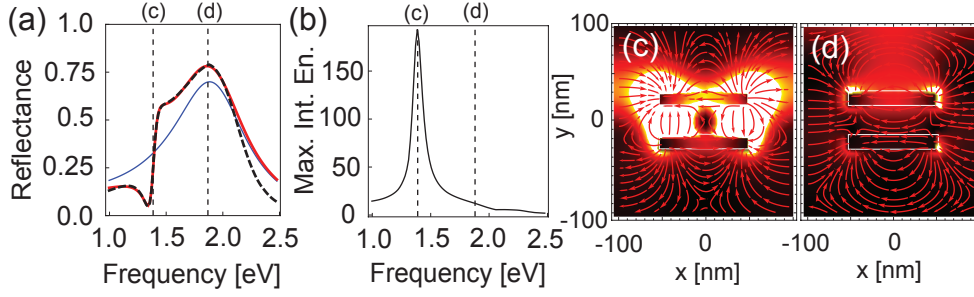


Figure 3.12: Fano-like resonance in a metallic double grating with the geometry of Figs. 3.5 and 3.6. The system is illuminated at normal incidence with a field propagating in the  $-z$ -direction, with the magnetic field polarized along the  $y$ -direction. (a) Reflectance as a function of the illumination energy. Black dashed line: numerical simulations; thick red solid line: fit with Eq. (3.5); thin blue solid line: bright mode resonance extracted from the fit [Eq. (3.4)]. (b) Maximum intensity enhancement as a function of the illumination energy. (c–d) Normalized intensity enhancement in the cross section plane at particular frequencies shown in (a) and (b): black  $\rightarrow 0$  and white  $\rightarrow 1$ .

extract  $\omega_a$  easily, without detailed knowledge of the near-field interactions.

It has been experimentally observed [25, 37] and theoretically demonstrated in Chapter 2 that the coupling between the bright and dark modes plays an important role for controlling the line shape of Fano-like resonances. This dominant effect of coupling is described by the modulation damping parameter  $b$  depending on the ratio between the energy lost in the metallic structure and the energy transferred from the bright mode to the dark mode [Eq. (3.3)]. The near-field intensity enhancement maps in Figs. 3.10 indicate that the most efficient way to change the coupling is by tuning the gap size  $g$  between the single beam and the pair of parallel beams, Fig. 3.13. For high coupling, in the spectral minimum in the reflectance response, the Fano interference opens a narrow transparency window for the incoming light, whose magnitude depends on the  $b$  parameter. As  $g$  increases, the coupling between the two modes decreases, the  $b$  parameter drastically increases and the resonance modulation depth is reduced. As a result, the reflectance of the system approaches that of the bright mode alone [Fig. 3.13(g) to (i)]. This effect appears only in the presence of intrinsic losses and goes along with a reduction of the absolute value of the asymmetry parameter (from  $-1.68$  for  $g = 15$  nm to  $-0.21$  for  $g = 50$  nm). As the coupling decreases, the resonance becomes more symmetric and its frequency shifts towards the reflectance dip. In addition, the resonance frequency blue shifts, and converges to the non-perturbed resonance frequency of the dark mode. The coupling of the dark mode to the bright mode opens a radiative decay channel for the dark mode, which in turns widens the Fano resonance. Figure 3.13(b) shows the intensity enhancement in the structure at the resonance frequency  $\omega_a$  extracted from a fit with Eq. (3.5); this frequency is indicated by a red dot in panel (a). The correlation between



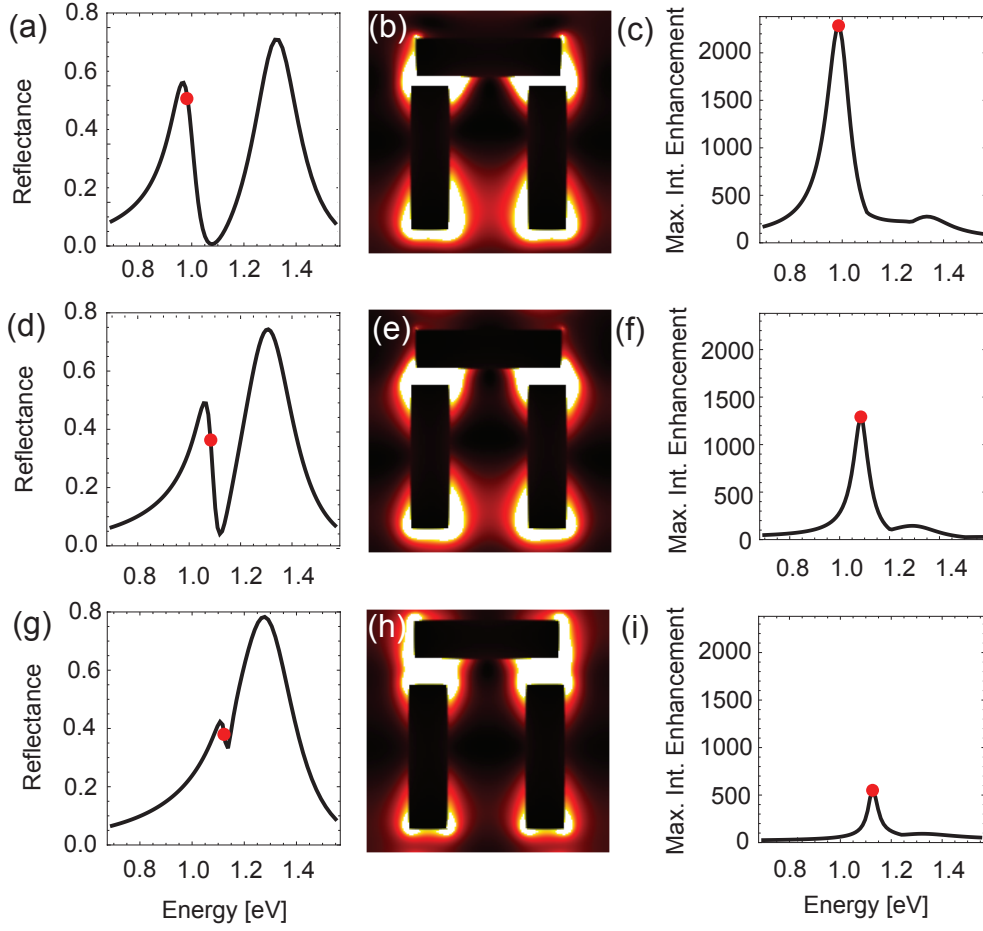


Figure 3.13: Influence of modes coupling on the resonance line shape for dolmen gold nanostructures with dimensions  $w = 40$  nm,  $l_0 = 160$  nm,  $t = 80$  nm, and  $l = L = 300$  nm. The coupling is changed by tuning the gap size  $g$ : (a–c)  $g = 15$  nm (d–f)  $g = 30$  nm (g–i)  $g = 55$  nm. (a,d,g) Reflectance at normal incidence for an  $x$ -polarized electric field propagating in the  $-z$ -direction, as a function of the illumination energy. The red dot indicates the Fano resonance frequency position. (b,e,h) Normalized intensity enhancement in a plane through the center of the structure at the Fano resonance frequency: black  $\rightarrow 0$  and white  $\rightarrow 1$ . (c,f,i) Maximum in intensity enhancement

near-field and far-field is also verified in this case: as the two modes decouple, the power transfer between the two modes becomes less effective. This results in a decrease of the field intensity in the two parallel beams, leading finally to field enhancement solely at the extremities of the single beam, when both structures are decoupled and the Fano resonance has disappeared. As mentioned previously, the structures are placed in an array to ensure that the quadrupolar mode is a true dark mode. Although its subwavelength character does not produce grating effects, this configuration is accompanied by strong near-field interactions between nearest neighbors. Actually, the gap size of  $g = 60$  nm

leading to a complete vanishing of the Fano resonance corresponds to a configuration for which the dipolar beam is placed at the same distance from its two adjacent beam pairs, i.e. to a configuration for which the array has a second symmetry plane. Moving the dipolar bar from this position induces the symmetry breaking required for the excitation of the dark mode, which explains the high sensitivity of the resonance line shape to the gap size  $g$ . The usage of symmetry breaking for sensing applications will be discussed in Chapter 4.

### 3.3 Conclusion

The optical properties of plasmonic nanostructures supporting Fano resonances have been investigated with surface integral numerical calculations and compared to the predictions of the electromagnetic theory developed in Chapter 1. By fitting the analytical formula to the numerical results, it has been shown that the line shape of Fano resonances satisfy the predictions of the electromagnetic theory in a broad variety of plasmonic nanostructures, and that this procedure is applicable for any continuum of radiative waves. In most plasmonic nanostructures, Fano-like resonances arise from the interference between a radiative and a non-radiative mode. The frequency position of the asymmetric resonance is determined by the dark mode frequency and its coupling to the bright mode. The width of the asymmetric resonance is determined by the coupling and intrinsic losses in the metallic structure, while intrinsic losses drastically affect the modulation depth and asymmetry of the resonance. The relative phase between the dark mode and the continuum determines the condition of constructive and destructive interference and the asymmetry of the resonance: the asymmetry parameter is a function of the spectral detuning between the dark and bright modes and depends on the observable that is chosen to monitor the resonance, for instance reflectance or extinction spectra.

It has further been shown that the central frequency of the asymmetric modulation extracted from the fit with the analytical formula corresponds to the maximum near-field intensity enhancement in the structure, but does not correspond to a specific point of the reflectance spectrum (for instance a local minimum or maximum). We have also related the far-field spectrum to the near-field configuration of the bright and dark modes, and addressed the effect of their coupling. The methodology described in this chapter should be useful to analyze and design a broad variety of Fano plasmonic systems with tailored near-field and far-field properties.

## 4 Applications

In the recent literature, it was often speculated that Fano resonances are able to confine light efficiently and are characterized by a very steep dispersion [14,15], which make them promising for sensing applications [36,40,41,126]. However, it was never investigated which configuration is the most sensitive. I will show that Fano resonances in plasmonic systems can be decomposed into three coupling regimes: weak coupling, regime of best field enhancement and strong coupling. For each of these regimes, the best configuration for sensing applications such as nanoscale rulers, surface enhanced Raman scattering and refractive index sensing will be determined analytically using results from Chapter 1, verified numerically with the method developed in Chapter 2 and experimentally. This analysis will lead to the introduction of an intrinsic figure of merit characterizing the sensitivity of Fano resonances to refractive index perturbations. In Section 4.2, a high throughput and cost efficient nanofabrication technique for Fano resonances will be finally discussed.

### 4.1 Three coupling regimes in Fano resonances: implications for sensing.

The influence of the modes coupling on the line shape, near-field enhancement and sensitivity to local perturbations of Fano-resonant systems is studied in details with extensive numerical simulations using the SIE method developed in Chapter 2. The Fano-resonant gold nanostructure under study is similar to the dolmen structures of Chapter 3 [Fig. 4.1]. The refractive index of the surrounding medium is 1.33 (water) and the dielectric permittivity of the nanostructure is taken from experimental data [102]. A single antenna (called beam in previous chapters) supports an electric dipole mode whose field distribution enables interaction with the far-field radiation. Two coupled parallel antennas support an electric quadrupole mode, whose interaction with the far-field radiation is forbidden. The interference between the two electromagnetic modes referred as radiative (bright) and non-radiative (dark) in the following, leads to the formation

of a Fano resonance. The three antennas are arranged in three dimensions to enable tunability from a symmetric configuration where the excitation of the dark mode is symmetry–forbidden, to a symmetry–broken configuration where the dark mode can be excited via its coupling to the bright mode. In the mechanical analog of two coupled oscillators, this effect is reproduced by tuning the constant of the spring linking the two masses. As modes eigenvalues for Maxwell’s equations are in units of frequency squared, the resonance formulas have been given in this thesis as a function of  $\omega^2$ . The plasmon resonances are located in the red part of the optical spectrum, so that their frequencies are much larger than their width. In this context, the resonance formula in Chapter 1 and 3 for the bright mode can be simplified and expressed as a function of  $\omega$  only. The Lorentzian width  $\gamma_b$  in units of  $\omega$  is determined by Taylor expansions to the second order around the resonance frequency  $\omega_b$ :  $\gamma_b = \Gamma_b/(2\omega_b)$ . The same procedure is applied to the generalized Fano resonance formula and its parameters.

In the symmetric configuration, the reflectance shows a single peak centered at the dipolar (bright) mode frequency [Fig. 4.1(b)]. Its amplitude  $R_b$  as a function of the frequency satisfies a Lorentzian distribution centered around  $\omega_b=1.599$  eV with a width of  $\gamma_b=0.040$  eV [Fig. 4.1(b)]. The central bar is then displaced from the symmetric position by a distance  $s$  along the  $y$ –axis. This breaking of the symmetry allows the excitation of the quadrupolar mode through its coupling to the dipolar mode. The mechanical equivalent of this process is to tune the coupling spring constant in a two oscillators system [Fig. 4.1(b)]. To facilitate the discussion, let me reintroduce the definitions of the main physical quantities in Fano–resonant systems. Assuming the dark mode has a resonance frequency  $\omega_d$ , the Fano resonance appears at a frequency  $\omega_a$  slightly shifted from  $\omega_d$ . The width  $\gamma_a$  of this resonance is given by the sum of two contributions:  $\gamma_a = \gamma_c + \gamma_i$ , where  $\gamma_c$  is related to radiative losses arising from the coupling of the dark mode to the bright mode, and  $\gamma_i$  is related to intrinsic losses by Joule effect in the metallic structure. Two pathways have to be considered: the direct excitation of the bright mode and the excitation and reemission of the dark mode through its coupling to the bright mode. The frequency dependent phase difference between the direct and indirect pathways leads to both a destructive and a constructive interference at the origin of the asymmetric nature of the resonance. The reflectance  $R_b$  of the bright mode is perturbed by an asymmetric modulation, so that the reflectance spectrum  $R$  satisfies:

$$R = R_b \frac{(\omega - \omega_a + q\gamma_a)^2 + b\gamma_a^2}{(\omega - \omega_a)^2 + \gamma_a^2}, \quad (4.1)$$

where  $q = (\omega_d - \omega_b)/[2\gamma_b(1 + \gamma_i/\gamma_c)]$  is the asymmetry parameter. With the configuration chosen in Fig. 4.1 and the following, the modes detuning is small compared to the bright mode width. This allows us to set in the weak coupling regime  $q \simeq 0$  in Eq. (4.1), which is equivalent to approximating the Fano resonance profile with an anti–Lorentzian. Light that has excited the dark mode and is reemitted has lost part of its intensity by absorption in the metal and the resulting destructive or constructive interference is

#### 4.1. Three coupling regimes in Fano resonances: implications for sensing.

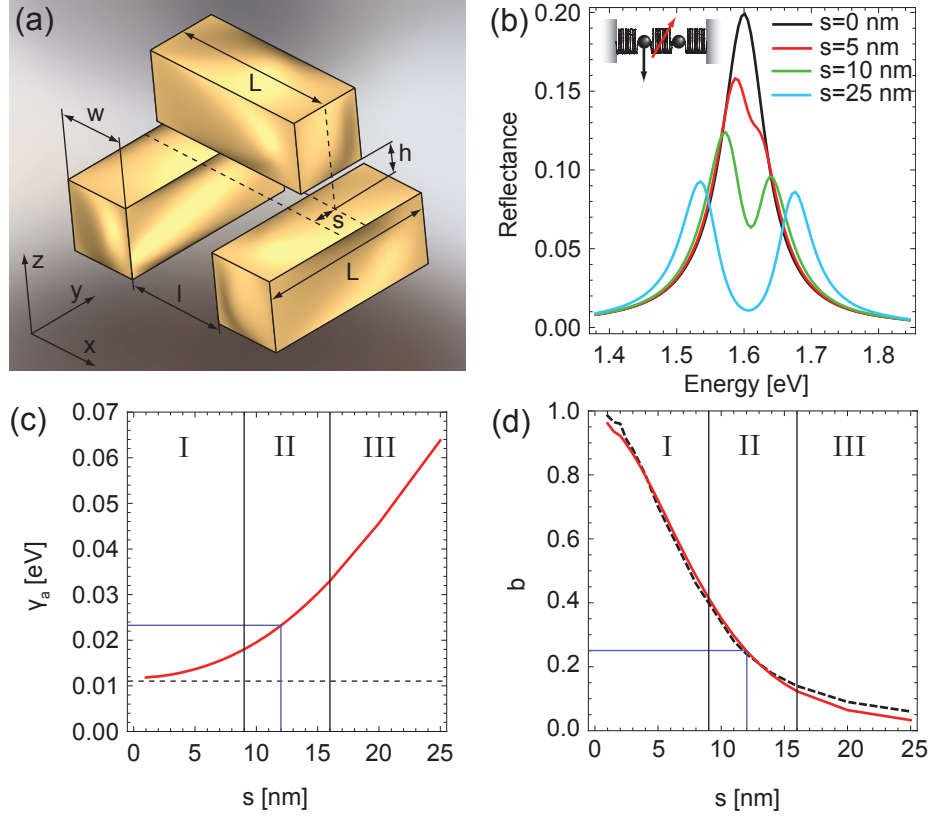


Figure 4.1: (a) Fano-resonant gold structure using the coupling between the dipole mode of the top bar with the quadrupole mode of the bottom bars in a symmetry broken configuration:  $L = 100$  nm,  $h = 20$  nm,  $l = 60$  nm and  $w = 40$  nm. It is placed in a two-dimensional array of period 500 nm. (b) Reflectance spectra of an array of the nanostructures for several values of the relative displacement  $s$  of the top bar from the symmetric position allowing the excitation of the quadrupolar mode. (c) Width  $\gamma_a$  of the Fano-like resonance reported as a function of the displacement  $s$ . (d) Modulation damping parameter as a function of the displacement evaluated in two different ways. Dashed black: ratio of the reflectance at the minimum of the Fano resonance to the reflectance of the symmetric system at the same frequency. Continuous red: the radiative and non-radiative contributions to the width  $\gamma_a$  are extracted from (c) and the modulation damping  $b$  is evaluated following Eq. (4.2).

altered. This effect is quantified by the modulation damping parameter, whose expression depends on the ratio of the power absorbed to the total power lost by the dark mode:

$$b = \frac{\gamma_i^2}{(\gamma_c + \gamma_i)^2}. \quad (4.2)$$

In the weak coupling regime,  $\gamma_c \ll \gamma_i$  and  $b \simeq 1$ , whereas in the strong coupling regime  $\gamma_c \gg \gamma_i$ ,  $b \simeq 0$  and Eq. (4.1) is close to original Fano formula (Chapter 1).

### 4.1.1 Plasmon Rulers

The evolution of the Fano–resonant structure optical spectrum when the modes coupling is increased from the weak to the strong coupling regimes is now studied in greater details. In Fig. 4.1(c), the width of the anti–resonance is extracted from the reflectance and reported as a function of the symmetry breaking  $s$ . When the modes coupling increases, the Fano resonance width increases; the minimum value of the width [dashed line in Fig. 4.1(c)] corresponds to the situation for which the dark mode excitation is forbidden and the mode suffers only from intrinsic losses. This minimum value cannot be evaluated directly from the spectra in Fig. 4.1(b) because no Fano resonance is observed. However, it can be defined as an asymptotic value for  $s \rightarrow 0$  and extracted by linear extrapolation: in this case  $\gamma_i=0.011$  eV. The contribution of the modes coupling to the total width  $\gamma_a$  is then calculated as a function of the symmetry breaking using its definition  $\gamma_c = \gamma_a - \gamma_i$ . This value is inserted into Eq. (4.2) and the modulation damping parameter reported in Fig. 4.1(d) as a function of the symmetry breaking. On the other hand, the parameter  $b$  can be directly evaluated from the far–field spectra as the ratio of the reflectance  $R$  at the minimum of the anti–resonance to the reflectance  $R_b$  of the symmetric structure. Its evaluation with both methods agree perfectly [Fig. 4.1(d)], which confirms the validity of the model and shows that the radiative and non–radiative lifetimes of the Fano–resonant mode can be evaluated in two consistent ways.

During the process of symmetry breaking, the spectral properties of this Fano–resonant system are drastically altered. In Figure 4.1(d), it is observed that in a quasi–symmetric configuration equivalent to a weak coupling regime, a displacement of 10 nm is equivalent to a change of 66% in intensity at a fixed frequency while the spectral shift of the minimum of the Fano resonance never goes beyond 3 nm, which is approximately 15% of the bright mode spectral width. The physical quantity that appears to be the most affected by the mechanical displacement is the modulation damping  $b$ , which strongly varies when a radiative channel is open for the dark mode. In this system, the direction of the displacement cannot be optically recognized, but using a more complex one with broken symmetry enables the measurement of three–dimensional mechanical displacements [126].

Plasmon resonances are extremely sensitive to local geometrical changes, which makes them very efficient as nanometer scale rulers [13]. Plasmon rulers have been first demonstrated by linking a pair of metallic nanoparticles by a DNA tether and optically monitor the biochemical processes resulting in the folding or buckling of the DNA tether [127]. They can also be used to develop an optical strain monitor [128]. More recently, the spectral behavior of Fano resonance system where monitored by placing them on a flexible substrate [42]. The generalization of the ruler concept to three–dimensions has been introduced using multiple Fano resonances [126]. The use of Fano resonances for rulers takes mostly advantage of their sharp spectral modulation, but we have shown in this section another approach which takes advantage of the high sensitivity of Fano resonances to the coupling between the dark and the bright modes as the symmetry of

## 4.1. Three coupling regimes in Fano resonances: implications for sensing.

the structure is broken and a radiative channel is opened for the dark mode. A sensing based on the measurement of the modulation damping  $b$  appears therefore to overcome the efficiency of wavelength-based rulers.

### 4.1.2 Field enhancement and surface enhancement Raman scattering (SERS)

We now investigate the evolution of the near-field enhancement in the nanostructure when the modes coupling channel is opened. In the symmetric configuration, only the bright mode is excited and the electromagnetic field is mostly confined in the top bar with a dipolar distribution of the phase [Fig. 4.2(a) and (b)]. The field enhancement is a lorentzian function of the frequency everywhere in the structure [Fig. 4.2(e)]. As the symmetry breaking increases, the electromagnetic field displays a quadrupolar distribution at the Fano resonance frequency [Fig. 4.2(c) and (d)]. In the zone where the dipolar mode is also present (top bar), their interference leads to an asymmetric line shape similar to that in the far-field response. However, in the zone where the dark mode is only present (bottom bars), the intensity enhancement satisfies a lorentzian distribution around the Fano resonance frequency [Fig. 4.2(e)], meaning that the electromagnetic energy density is redistributed from the bright mode to the dark mode. It has been shown analytically in Chapter 1 that the near-field intensity enhancement of the dark mode is proportional to  $\gamma_c/(\gamma_c + \gamma_i)^2$ . In the ideal case where the metallic structures would be perfect conductors (i.e.  $\gamma_i = 0$ ), light would remain longer in the dark mode and more electromagnetic energy would be stored as the coupling decreases. In a non-ideal case however, intrinsic losses drastically damp the electromagnetic oscillations with a long lifetime, so that the intensity enhancement for very weak coupling ( $\gamma_c \ll \gamma_i$ ) vanishes [Fig. 4.2(f)]. As the coupling increases, the in-coupled energy balances losses, and the intensity enhancement reaches a maximum. For stronger coupling ( $\gamma_c \gg \gamma_i$ ), the radiative channel for the dark mode limits the energy stored and the near-field intensity enhancement decreases. The analytical profile for the field enhancement has been reconstructed in Fig. 4.2(f) from the values reported in Fig. 4.1(c). The agreement with the direct evaluation of the intensity with numerical calculations is again almost perfect and confirms the theoretical predictions. For a symmetry breaking of 12 nm, a particular regime is reached for which the contributions of non radiative and radiative losses to the resonance width are equal (i.e.  $\gamma_c = \gamma_i$ ) and the energy stored by the mode is maximum. For this regime, the modulation damping is exactly equal to 1/4.

This strong variation of near-field intensity is expected to have a direct influence on the surface enhanced Raman scattering (SERS) response of adsorbed molecules. SERS is a very attractive spectroscopic technique because detailed information on the vibrational levels in the analyte is contained in the Raman signal and may be used for chemical detection. The electromagnetic enhancement factor satisfies  $EF = |E_{\text{ex}}/E_0|^2 |E_{\text{sto}}/E_0|^2$  where  $E_{\text{ex}}/E_0$  is the near-field intensity enhancement factor at the excitation laser

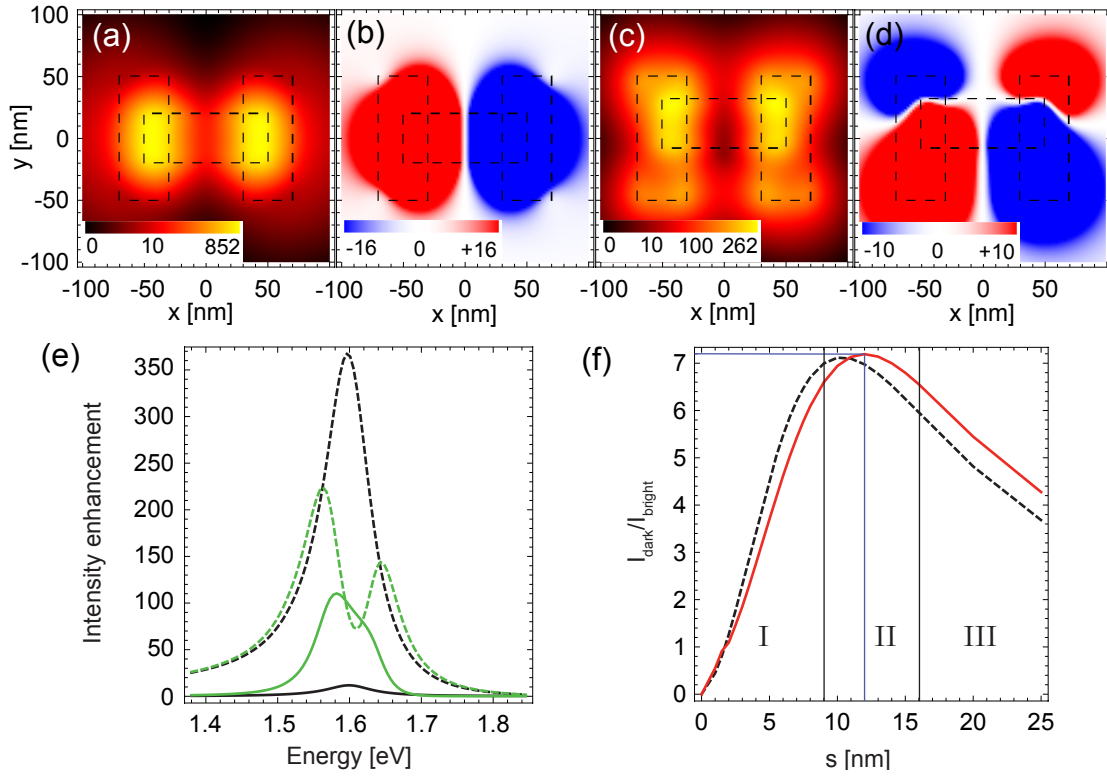


Figure 4.2: Electric field intensity on a  $(x,y)$  plane at half the distance between both structures for illumination energy 1.61 eV (a) in the symmetric case and (c) with  $s = 12$  nm symmetry breaking, respectively. (b,d) Corresponding amplitude of the real part of the  $z$ -component of the instantaneous electric field intensity. (e) Intensity enhancement as a function of the frequency: dashed—4 nm from the top bar extremity, continuous—4 nm from one of the bottom bar extremities, black—symmetric case, green—symmetry breaking of 12 nm. (f) Dark mode intensity enhancement normalized to bright mode intensity enhancement as a function of the symmetry breaking  $s$ : dashed black—directly computed, continuous red—reconstructed from the width profile of Fig. 4.1(c) (see text).

wavelength and  $E_{sto}/E_0$  is the near-field enhancement factor at the wavelength specific to the Stokes mode of interest for the molecular analyte. Since plasmon resonances are able to concentrate the electromagnetic field in extremely small volumes, they are very good candidates for SERS. In the configuration where both the excitation and Stokes wavelengths are located within the plasmon resonance spectral range, the enhancement factors are comparable and the SERS signal is enhanced by the fourth power of the field amplitude. For the utilization of Fano resonances to enhance SERS signals, the choice of the coupling regime optimizing the field enhancement is particularly critical.

In Figure 4.3, an array of gold nanocrescents is studied as a SERS substrate. The fabrication and measurements were performed by our collaborators at the Paul Scherrer Institute [129]. First, extreme ultraviolet interference lithography has been used to



#### 4.1. Three coupling regimes in Fano resonances: implications for sensing.

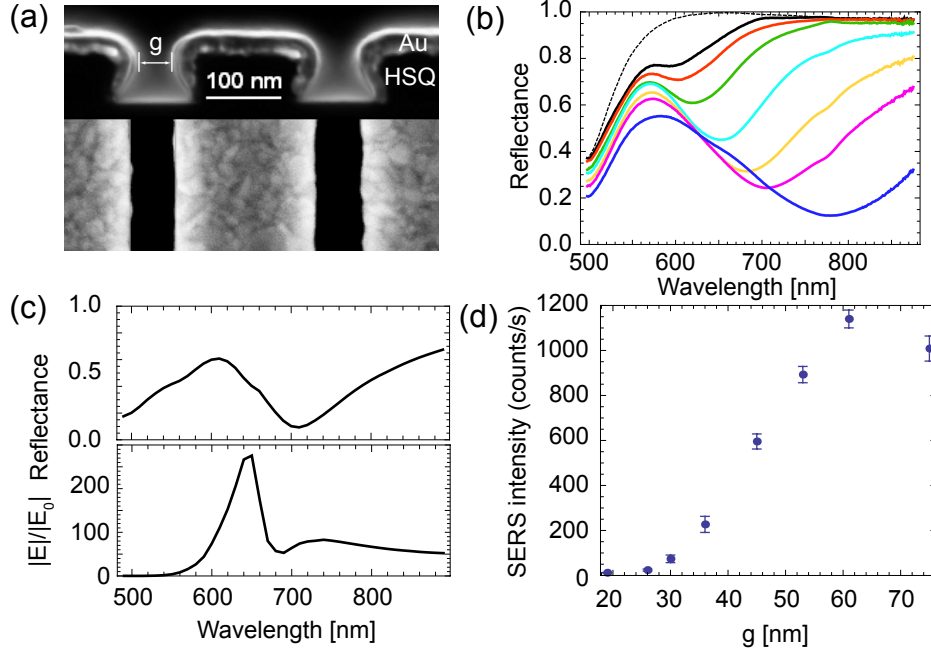


Figure 4.3: Array of gold nanocrescents as a Fano-resonant SERS substrate [129]. The underlying grating consists of HSQ photoresist with a periodicity of 250 nm, a depth of 80 nm and a spacing of 100 nm between two lines. A layer of 30 nm of gold is evaporated at  $60^\circ$  from the surface normal. (a) Top: cross sectional SEM view of the array; bottom: top SEM view. (b) Experimental reflectance spectra for various gap sizes  $g$ : dashed–0 nm, black–26 nm, red–30 nm, green–36 nm, light blue–45 nm, yellow–53 nm, purple–61 nm, dark blue–75 nm. (c) Top: reflectance spectrum for a period of 250 nm calculated with SIE method for a gap size of 50 nm; bottom: corresponding near-field enhancement at the extremities of the crescents (d) SERS intensity for varying gap size. The excitation was set at 633 nm and the SERS intensity corresponds to the  $1008\text{ cm}^{-1}$  peak of a self assembled benzeneethanethiol monolayer. Error bars correspond to the standard deviation of 16 spatially separated measurements and quantitative analysis of SEM images across the patterned area.

expose line patterns with 250 nm period into a 90 nm thick hydrogen silsesquioxane (HSQ) placed on a silicon substrate. A 30 nm thick layer of gold was then deposited at  $60^\circ$  angle from the surface normal and with an azimuthal orientation perpendicular to the length of the nanowires. Repeated cycles of metal deposition followed by flipping the substrate to the opposite direction were carried out until the final thickness was reached [130]. The resulting gold nanostructures have the form of crescents as seen in the Scanning Electron Microscope (SEM) images in Fig. 4.3(a). Individual metallic crescents can support plasmon resonances, the region of highest field enhancement located at their tip extremities [131, 132]. The experimental reflectance spectra of several samples for various separations between nearest neighbors are shown in Fig. 4.3(b) [129]. Placed

in a closed-packed array, the reflection spectrum resembles that of an infinite metallic film, close to unity for energies below the interband transition of gold. As the gap opens, a surface plasmon is excited in the gap between two neighboring nanostructures. The destructive interference of light re-emitted by the gap plasmon with the directly reflected light yields a dip in the reflectance spectrum and enhanced transmission through the nanoslits [19] [Fig. 4.3(b)]. Comparing the far-field reflectance spectrum to the near-field enhancement from numerical simulations with the SIE method [Fig. 4.3(c)], this dip is in fact asymmetric and carries the traces of a Fano resonance. For very large gaps, the transmission window widens and red-shifts, the degree of asymmetry of the Fano resonance increases, and the resonance frequency shifts towards the reflectance peak (Chapter 3). In this system, the continuum of radiative waves is given by the light directly transmitted through the slits, whereas the plasmon mode excited in the gap plays the role of the resonant mode weakly coupled to radiation for a very small slit opening. In Fig. 4.3(d), the SERS intensity of the array is measured as the gap widens and the radiative channel opens for the plasmon mode. As previously discussed, the SERS intensity provides an indirect measurement of the electromagnetic intensity enhancement in the nanostructures. As expected from my theoretical prediction, a maximum is observed corresponding to the situation where radiative coupling of energy balances intrinsic losses. This situation occurs for a gap of 61 nm, and the corresponding minimum in reflectance is 23.4% in Fig. 4.3(b). Taking the ratio of the reflectance spectrum for 61 nm with the reference for 0 nm gives 24.6% for the modulation damping parameter  $b$ . This value is in excellent agreement with the theoretical prediction of  $1/4$ , confirming experimentally the validity of the theoretical model predicting an intermediate coupling regime optimal for near-field enhancement.

### 4.1.3 Refractive index sensing

Plasmon resonances depend on the dielectric properties of the metal, the size and shape of the nanostructures and the dielectric function of the surrounding environment [7, 8]. The latter effect can be used for the development of sensors for global or local refractive index variations. In this Section, we aim at studying the efficiency of Fano-resonant systems for refractive index sensing as a function of the modes coupling. In the first case, the dielectric function of the entire environment is modified, corresponding for example to a change of the type of liquid surrounding the nanostructures [133]. The second type consists in perturbing the local environment of the nanostructures by attaching a biochemical analyte, which is equivalent to a variation of the refractive index in a thin layer of a few nanometers around the nanostructures surface. The figure of merit (FOM) of a resonance for refractive index sensing is a unitless number defined as the ratio of the mode sensitivity to its full width at half maximum (FWHM) [134, 135]:

$$\text{FOM} = \frac{\text{sensitivity [eV} \cdot \text{RIU}^{-1}]}{\text{FWHM [eV]}}, \quad (4.3)$$

#### 4.1. Three coupling regimes in Fano resonances: implications for sensing.

It has been seen in Section 4.1.1 that the FWHM of Fano resonances depends on the modes coupling. Consequently, the FOM of Fano-resonant system is not only a property of the individual modes. It becomes therefore impossible to compare Fano resonant system for which the modes coupling is not controllable independently of the other parameters [35, 109, 115, 116]. Therefore, a FOM for Fano resonant systems related only to the intrinsic properties of the dark mode but not to the modes coupling will be introduced. In Section 4.1.3, the induced frequency shift of the plasmon resonance is derived analytically from perturbation theory in the framework of Chapter 1. The sensitivity and FOM of the plasmon resonances for global and local refractive index changes are then discussed with support of numerical simulations in Section 4.1.3.

#### Perturbation theory

In this Section, an analytical expression for the frequency shift of a plasmon resonance to a variation of the refractive index will be derived using perturbation theory in the framework of Chapter 1. The field of a non-radiative mode is confined to a region defined by the projection operator  $Q$ . A perturbation of the refractive index in the  $Q$  region will therefore be considered in the following. We start from the pseudo eigenvalue equation for a plasmon mode:

$$Q \underline{\mathcal{M}}_{\omega_d} Q |\mathbf{E}_d\rangle = z_d^2 |\mathbf{E}_d\rangle, \quad (4.4)$$

where  $z_d = \omega_d + i\gamma_d$  is the complex frequency eigenvalue. Assuming that the spectrum contains only the mode  $|\mathbf{E}_d\rangle$  in the frequency range under consideration, the operator  $Q$  can be written in an explicit form  $Q = |\mathbf{E}_d\rangle \langle \mathbf{E}_d|$ . Considering that the plasmon mode is normalized, Equation (4.4) becomes:

$$c^2 \int d^3\mathbf{r} \frac{\epsilon'(\mathbf{r}) + i\epsilon''(\mathbf{r})}{\epsilon'(\mathbf{r})^2 + \epsilon''(\mathbf{r})^2} \mathbf{E}_d^*(\mathbf{r}) \cdot \nabla \times \nabla \times \mathbf{E}_d(\mathbf{r}) = \omega_d^2 - \gamma_d^2 + 2i\gamma_d\omega_d, \quad (4.5)$$

where  $\epsilon' = \text{Re}(\epsilon(\omega_d))$  and  $\epsilon'' = \text{Im}(\epsilon(\omega_d))$ . The imaginary part of Eq. (4.5) gives the equation for the damping parameter  $\gamma_d$ , which depends on the conductivity of the materials and the penetration of the field in the conductive materials. Taking the real part of Eq. (4.5) and neglecting second order contributions from intrinsic losses yields:

$$\int d^3\mathbf{r} \frac{c^2}{\epsilon'(\mathbf{r})} \mathbf{E}_d^*(\mathbf{r}) \cdot \nabla \times \nabla \times \mathbf{E}_d(\mathbf{r}) = \omega_d^2. \quad (4.6)$$

A perturbation  $\Delta\epsilon$  is introduced to the real part of the permittivity  $\epsilon_1(\mathbf{r}) = \epsilon'(\mathbf{r}) + \Delta\epsilon f(\mathbf{r})$  where  $\Delta\epsilon \ll \epsilon_b$  and  $f(\mathbf{r})$  is the characteristic function of the perturbation, usually restricted to a sub-domain  $V$  of the total space. The permittivity of the perturbation is

assumed non-resonant and non dispersive. The mode has a new frequency eigenvalue  $\omega_1$ :

$$\int d^3\mathbf{r} \frac{c^2}{\epsilon_1(\mathbf{r})} \mathbf{E}_d^*(\mathbf{r}) \cdot \nabla \times \nabla \times \mathbf{E}_d(\mathbf{r}) = \omega_1^2. \quad (4.7)$$

Using the definition of  $\epsilon_1$  and considering first order perturbation:

$$\omega_1^2 = \omega_d^2 - \int_V d^3\mathbf{r} \frac{c^2 \Delta\epsilon}{\epsilon_1(\mathbf{r})^2} \mathbf{E}_d^*(\mathbf{r}) \cdot \nabla \times \nabla \times \mathbf{E}_d(\mathbf{r}). \quad (4.8)$$

The shift in frequency due to the perturbation can then be written as:

$$\Delta\omega_d \simeq -\frac{\omega_d}{2} \int_V d^3\mathbf{r} \frac{c^2 \Delta\epsilon}{\epsilon'(\mathbf{r})^2} \mathbf{E}_d^*(\mathbf{r}) \cdot \nabla \times \nabla \times \mathbf{E}_d(\mathbf{r}). \quad (4.9)$$

The assumption that the plasmon mode is not a true eigenvector of the operator  $\underline{\underline{M}}_\omega$  is a cornerstone of the model elaborated in Chapter 1, but in the context of Eq. (4.9) it does not strongly influence the integral, which can be simplified to:

$$\Delta\omega_d \simeq -\frac{\omega_d}{2} \int_V d^3\mathbf{r} \frac{\Delta\epsilon}{\epsilon'(\mathbf{r})} |\mathbf{E}_d(\mathbf{r})|^2. \quad (4.10)$$

Equation (4.10) is equivalent to the well known result for non lossy systems [136, 137]. It implies in particular that the perturbation induces a spectral shift if it is placed in the region where the mode field is the most intense. For a nanoparticle with a volume much smaller than the modal volume, the perturbation is proportional to the intensity enhancement at its position.

### Sensitivity and figure of merit for refractive index sensing

We now want to investigate the behavior of the bright mode and the Fano resonance sensitivity [Eq. (4.10)] and FOM [Eq. (4.3)] as a function of the coupling strength. In Figures 4.4(a) and (b), the refractive index of the surrounding medium is increased from 1.33 (water) for a structure with a symmetry breaking of  $s=10$  nm. The position and width of the bright and dark modes are obtained by locally fitting the spectrum with a lorentzian or an anti-lorentzian profile [Eq. (4.1)] respectively. The asymmetry parameter slightly shifts the Fano resonance position (Chapter 3) but as it depends on the modes detuning, it does not vary strongly with the refractive index perturbation. Hence, it does not play a role when measuring a frequency shift of the resonances positions (the same remark holds for the frequency shift of the Fano resonance position  $\omega_a$  from the dark mode frequency  $\omega_d$ ). From perturbation theory, the frequency shift of the plasmon mode is linear with respect to the refractive index difference, which is verified in Fig. 4.4(a) and (b). A bulk perturbation affects the modes frequency depending on the proportion of the mode that lies in the surrounding environment. To the contrary of most photonic resonances, surface plasmon resonances are usually bound to the surface of the metallic

#### 4.1. Three coupling regimes in Fano resonances: implications for sensing.

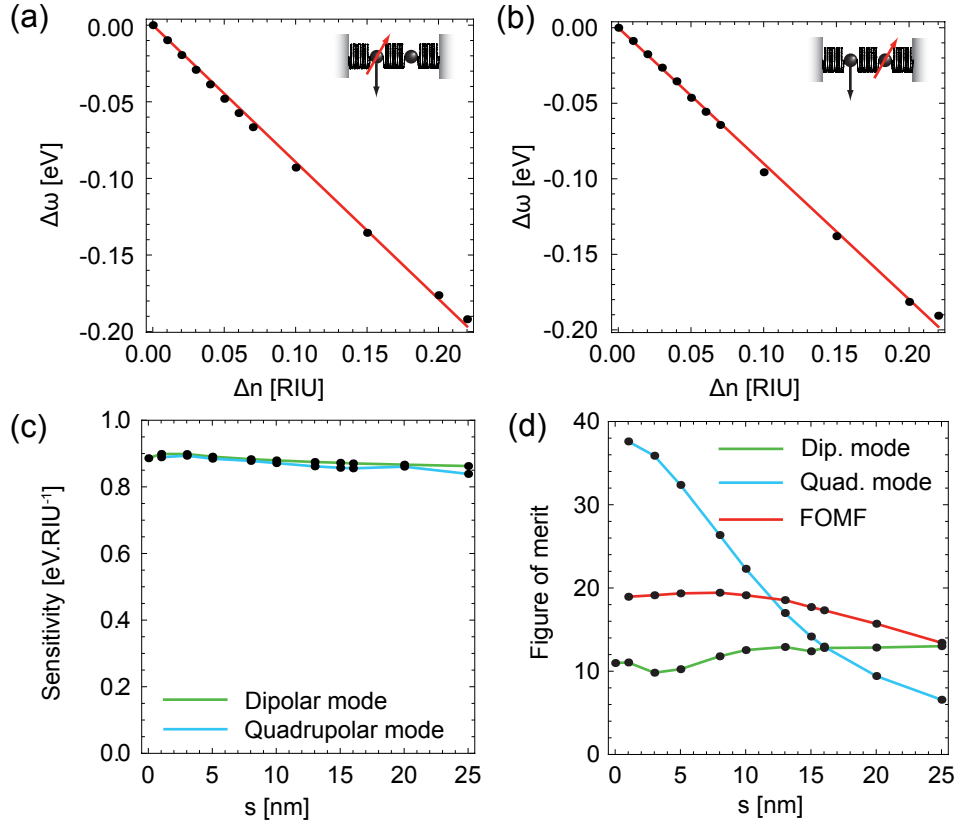


Figure 4.4: Refractive index sensing with Fano-resonant systems. In the mechanical analog of two coupled oscillators, this effect is reproduced by tuning the mass of each oscillator. (a–b) Variations of the plasmon resonance position  $\Delta\omega$  as a function of the change in refractive index of the surrounding environment (initial refractive index  $n=1.33$ ) in a configuration with symmetry breaking  $s=10$  nm: (a) dipolar mode (b) quadrupolar mode. (c) Spectral sensitivity  $\delta\omega/\delta n$  to the refractive index variation and (d) conventional FOM [Eq. (4.3)] as a function of the symmetry breaking for the dipolar (blue) and quadrupolar (green) modes. Red: adapted figure of merit for Fano resonances [FOMF, Eq. (4.11)].

structures and mostly present in the surrounding environment and as a result strongly affected by perturbations of its refractive index. Since the dark and the bright modes have their field equally present in the environment, their sensitivity is similar and almost independent of their coupling [Fig. 4.4(c)]. As the modes coupling increases, the bright mode width slightly decreases, so that its FOM increases [Fig. 4.4(d)]. On the other hand, the Fano resonance width strongly increases [Fig. 4.1(c)] so that its FOM decreases from 38 for  $s=1$  nm to 6.5 for  $s=25$  nm. At this coupling regime, the reflectance spectrum appears as two individual peaks [Fig. 4.5(a)].

The low energy peak corresponds to a modes combination for which the top bar is out of

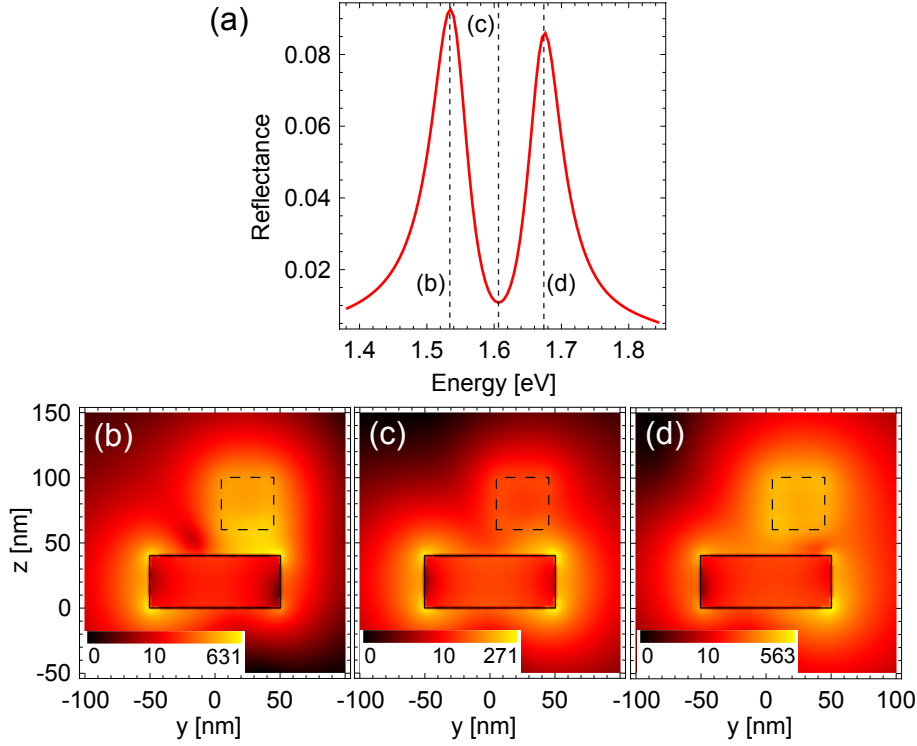


Figure 4.5: (a) Reflectance at  $s = 25$  nm of symmetry breaking. It appears as two individual peaks with spectral spacing larger than their width and indicates a strong coupling regime. (b,c,d) Electric field intensity on a  $y = \text{cst}$  plane ( $y = 60$  nm in Fig. 4.2) at energies 1.53 eV, 1.60 eV and 1.68 eV.

phase with the closest extremities of the bottom bars [Fig. 4.5(b)]. The electric field is linking the extremities of the top bar to the nearest extremities of the bottom bars due to their opposite charge distribution. A high field enhancement in the region of sampling is observed, similarly to the high field observed in the gap of a nanoantenna. The high energy peaks corresponds to the in-phase superposition of the modes [Fig. 4.5(d)]. As a result, the field is more homogeneously distributed in the structure and almost vanishing in the gap. As the modes coupling is strong, the intensity enhancement in the spectral dip is relatively low [Fig. 4.2(c)]. The limit at which the coupling regime can be considered as strong is when the full width of the Fano dip, that is the peaks separation, is similar to their FWHM. The crossing of the FOM occurs at 16 nm of symmetry breaking [Fig. 4.4(d)].

We now consider the situation where the system is locally perturbed by a thin layer of 4 nm with refractive index 1.55 (Fig. 4.6). This situation corresponds to attaching biomolecules on the metallic surfaces of the nanostructure [40, 138]. The background material is still water. For each coupling situation, the frequency shift of the bright mode

#### 4.1. Three coupling regimes in Fano resonances: implications for sensing.

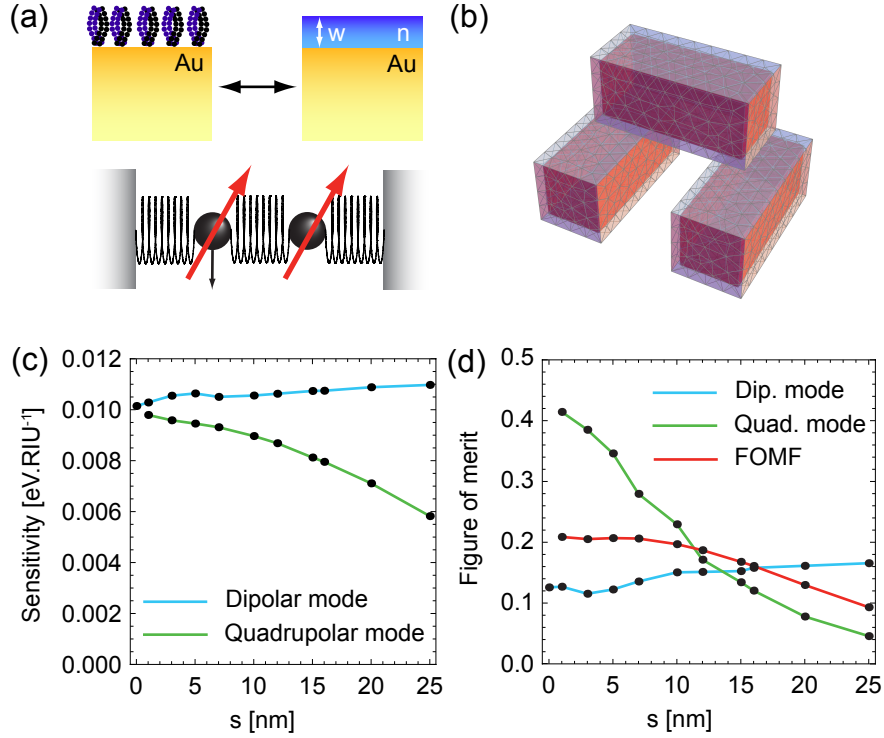


Figure 4.6: (a) Local refractive index sensing of biomolecules adsorbed on the metallic surface. The optical equivalent is the addition of a thin layer of an effective refractive index  $n=1.55$  and width  $w = 4$  nm. In the mechanical analog of two coupled oscillators, this effect is reproduced by tuning the mass of each oscillator. (b) Discretization of the system made of the nanostructure and the attached layer of 4 nm with refractive index 1.55. (c) Spectral sensitivity  $\delta\omega/\delta n$  to the refractive index variation and (d) figure of merit [Eq. (4.3)] as a function of the symmetry breaking for the dipolar (blue) and quadrupolar (green) modes. Red: adapted figure of merit for Fano resonances [FOMF, Eq. (4.11)].

and the Fano resonance dip are computed and reported in Fig. 4.6(c). As the coupling increases, the Fano resonance sensitivity slightly decreases and its spectral broadening drastically reduces the FOM [Fig. 4.6(d)] which becomes comparable to the bright mode FOM for a symmetry breaking of 12 nm. Fano resonances have a higher FOM and appear more suitable than conventional plasmon resonances for refractive index sensing, since the contribution of radiative and non-radiative losses to their spectral width can be controlled.

Overall, both the bright mode and Fano resonances have a comparable sensitivity but their FOM for refractive index sensing are mostly determined by their respective width. In particular, the FOM of a Fano resonance can be drastically increased as the modes coupling is increased, but it does not take into account that the modulation depth is reduced and that the detection is expected to be noise limited in the weak coupling

regime [Fig. 4.1(d)]. Although the FOM introduced by Van Duyne and co-workers [Eq. (4.3)] successfully characterizes the efficiency of a plasmon resonance for refractive index sensing [134], it does not appear to be appropriate to compare this efficiency for Fano resonances. With a simple argument based on modes coupling, we now propose an adapted figure of merit. The width  $\gamma_a$  of a Fano resonance is the sum of the contributions from intrinsic losses  $\gamma_i$  and from the modes coupling  $\gamma_c$ . From Eq. (4.2) the product  $2\gamma_a\sqrt{b} = 2\gamma_i$  does not depend on the coupling strength and corresponds to the Fano resonance width in the optimal regime of local field enhancement [Fig. 4.2(f)]. Therefore, the unitless figure of merit for a Fano resonance (FOMF) defined by:

$$\text{FOMF} = \frac{\text{sensitivity [eV}\cdot\text{RIU}^{-1}]}{4\sqrt{b}\gamma_a [\text{eV}]}, \quad (4.11)$$

takes solely into account its sensitivity to variations of the refractive index and its intrinsic width. Most importantly, it is independent from the coupling regime and depends on physical quantities directly measurable in the far-field. The FOMF is equivalent to the conventional FOM when the modulation damping is 1/4, corresponding to the optimal coupling regime (Section 4.1.2). It is therefore possible with the FOMF to compare different Fano-resonant systems with each other, including the ones for which the coupling cannot be controlled independently of the other parameters [35, 109, 115, 116]. In such cases, the modulation damping is found by performing a fit of the entire spectrum following the procedure of Chapter 3. The FOMF for both bulk and local perturbations is shown in Fig. 4.4(d) and Fig. 4.6(d), respectively. It decreases for high values of  $s$  because the strong coupling regime is attained and the analytical model reaches its limit.

## 4.2 Towards large scale fabrication

The practical implementation of Fano-resonant systems in the visible range requires the fabrication of metallic structures with a nanometer range resolution. Among the most commonly used techniques, focused ion beam (FIB) [139, 140] and electron beam lithography (EBL) [141] allow extremely precise fabrication. However, those techniques suffer from their serial nature resulting in high costs and poor throughput. In contrast to FIB and EBL, replication based techniques enable surface patterning over large areas. Imprint lithography uses compression molding to create a thickness contrast pattern and can be highly parallelized by fabrication of multiple stamps from the same original pattern. Its resolution can be scaled down to the nanometer range [142]. The high throughput and low cost of the nanoimprint lithography (NIL) technique make it very attractive for technology transfers towards industrial applications. Although the scope of this thesis is not on nanofabrication, the implementation of Fano-resonant devices with a method that has the potential to be translated to an industrial environment was of particular importance to me. Therefore, I would like to report on a collaborative work with the Microsystems Laboratory at EPFL on nanofabrication of plasmonic structures



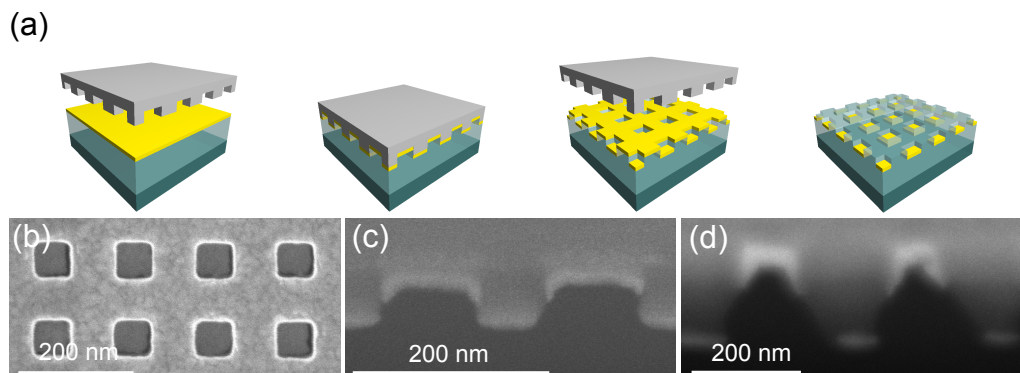


Figure 4.7: (a) Schematic of the metal nanoimprint process. A gold film is deposited on a parylene C layer, imprinted at 120-140 °C using a silicon stamp and cooled to room temperature before pressure release. (b) Imprint of a 300 nm period array into 40 nm of gold deposited on a 2  $\mu\text{m}$  parylene C film. The brighter is the top grid layer, the darker are the gold dots embedded into the parylene C. (c–d) Focused Ion Beam (FIB) cross sections of the corresponding imprinted films showing the well defined vertical separation between two metal layers: (c) 45 nm separation, (d) 120 nm separation [143].

using NIL [143, 144]. In this work, a thin gold layer deposited on a polymer has been patterned in a one step process of press and release, the resulting nanocut structures consisting of two isolated layers of metal (Fig. 4.7). I show in this section that the fabricated structures can support dipolar and quadrupolar plasmon resonances in a similar way as split-ring resonators [138], and their optical extinction spectrum have a Fano-like line shape.

The bilayer consisting of Au on top of parylene C (poly-chloro-p-xylylene C) was deposited on a glass substrate by e-beam evaporation and chemical vapour deposition (CVD), respectively. After deposition, a sharp silicon stamp patterned with EBL was used to cut the structures into the metal. A proper metal nanocutting is achieved at temperatures where viscosity of the polymer is low enough for an abrupt vertical metal displacement. At this temperature, the overlaying metal is deformed, breaks under pressure, and is finally pushed into the polymer to a maximal depth depending on the protrusion height of the stamp [Fig. 4.7(a)]. Periodic patterns of squares with dimensions ranging from 60 nm to 500 nm were successfully obtained using nanocutting [Fig. 4.7(b)]. The FIB cross sections in Fig. 4.7(c) show that the two metallic layers are electrically isolated after the nanoimprint process. For large stamps protrusion heights, the applied pressure deforms the top metallic layer and the polymer material is displaced during stamping and pushes the central region of the top layer up, so that the top metallic layer acquires a three-dimensional geometry [Fig. 4.7(d)]. As-fabricated samples have a double layer of gold nanostructures. By removing the top metal layer using adhesive tapes, it is possible to obtain samples with a single layer of gold nanostructures.

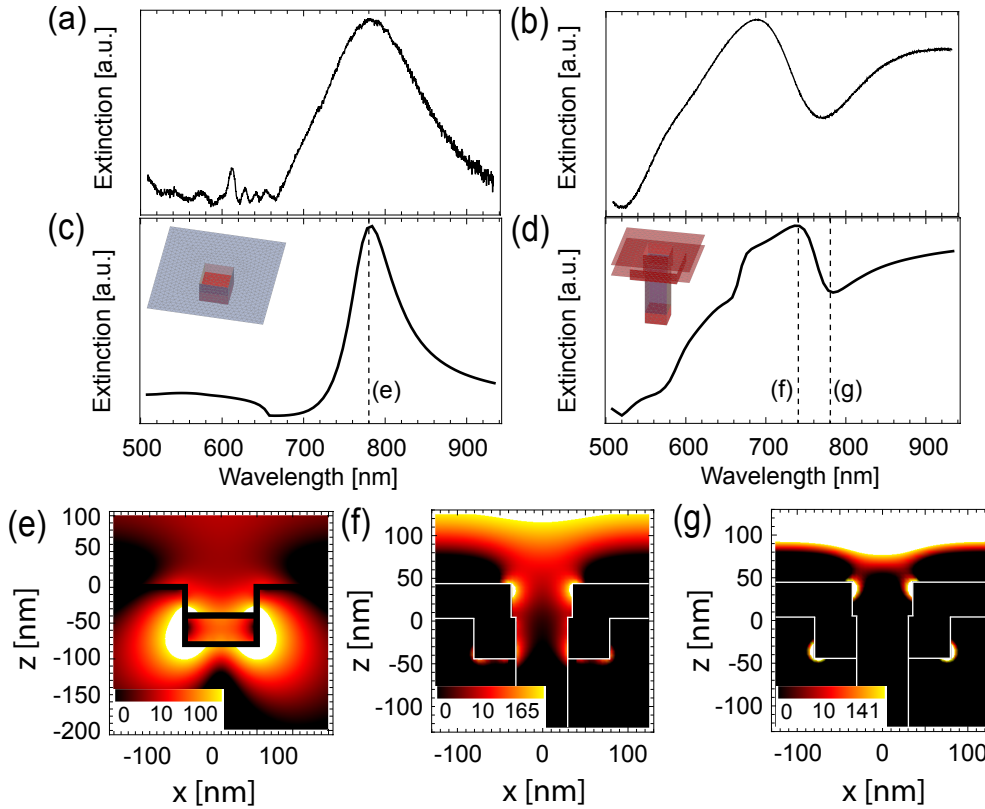


Figure 4.8: Extinction spectra of (a) an array of individual dots embedded in a film of parylene C and (b) a double gold layer with 120 nm separation [144]. (c–d) Corresponding numerical simulations with SIE method. A constant refractive index of 1.639 and experimental data [102] were chosen for parylene C and gold, respectively. The discretized objects in the unit cell used for simulations are shown in the insets. (e) Electric intensity enhancement in the near-field of the dots array at 780 nm. (f–g) Electric intensity enhancement in the near-field of the top gold grid at 740 nm and 780 nm, respectively.

The optical response of the single and double layer gold nanostructures was measured in extinction using an inverted microscope in bright field configuration and normalized with respect to the lamp spectrum [144]. The plasmon resonance of individual dots appears as an extinction peak in Fig. 4.8(a) whose spectral position is in very good agreement with calculations using the SIE method in Fig. 4.8(c). In order to perform the measurements at normal incidence, light is collected over a large number of structures in the array. A variation of the dimensions of the individual dots in the array induces an inhomogeneous broadening of the extinction peak as compared to simulations. From Fig. 4.8(e), the electric field intensity is mostly distributed in the parylene C substrate and therefore inaccessible to molecular analytes for biosensing applications [135].

With the structures of Fig. 4.7(d), a broadband high extinction is observed due to the high filling factor of metal. Nevertheless, a dip in extinction is observed at 780 nm

because the structures on top can support not only a dipolar plasmon resonance like in the individual dots of Fig. 4.8(a), but also a resonance with a quadrupolar distribution of charges. This structure is similar to an array of split ring resonators, very well known from the metamaterial community and proven very efficient for the detection of single molecular monolayers [138, 145]. The excitation of the dark quadrupolar mode leads to the opening of a transmission window for light with a Fano-like line shape in the extinction spectrum [Fig. 4.8(d)]. The field distribution in Fig. 4.8(f) shows that a dipolar mode is excited at 740 nm and contributes to the extinction maximum. At 780 nm, the quadrupolar is resonantly excited [Fig. 4.8(g)]. The electric field is now also distributed in the air region above the structure and accessible to molecular analytes for biosensing applications.

### 4.3 Conclusions

To summarize, it has been analytically demonstrated, numerically and experimentally verified that Fano resonances in plasmonic nanostructures, and more generally in non-conservative systems, have three coupling regimes: in the weak coupling regime, a very high sensitivity to the opening of a radiative channel for the dark mode is observed. In the weak coupling regime, the resonance life time is very long, which would in principle enable a high storage of electromagnetic energy in the dark mode. However, intrinsic losses in the metal strongly damp these long-lived oscillations of the field, so that an optimal regime of highest electromagnetic field enhancement is obtained only when the in and out-coupling balance intrinsic losses (intermediate regime). For stronger coupling, the specific features of Fano resonances are altered: the field enhancement is not maximized and the spectral width becomes large.

The knowledge of the mechanisms of Fano resonances acquired from these analytical and numerical studies has been translated to the optimization of nanoplasmonic systems for a broad range of applications involving Fano resonances. It has been shown in particular how the best coupling regime for a specific application can be chosen. In the weak coupling regime, the modulation depth is a physical value extremely sensitive to the modes coupling, which can be used for nanoscale plasmon rulers to measure nanometric displacements [126, 127]. In the intermediate regime, the best electromagnetic field enhancement is obtained and the devices are optimized for second harmonic generation [146], as well as for surface enhanced Raman scattering [41] and antenna-based trapping [147] for biomolecule recognition. The sensitivity of Fano-resonant systems to local perturbations of the refractive index has then be discussed [36, 40]. Here, higher figures of merit than conventional plasmon resonances can be obtained because the contribution of radiative and non-radiative losses to the spectral width can be controlled. This analysis has finally led to the introduction of an intrinsic figure of merit for refractive index sensing using Fano-resonant systems.

## Chapter 4. Applications

---

Finally, some specific experimental realizations of Fano resonant systems have been explored. It has then been shown that a gold film can be patterned at the nanoscale with a single step press and release nanoimprint process. The resulting nanostructures consist of two gold layers with complementary geometries and isolated from each other by a layer of polymer with controllable thickness. Experimental extinction spectra together with numerical simulations with the SIE method show that these nanostructures can support dipolar and quadrupolar plasmon resonances. These results pave the way towards large scale and industrial fabrication of three-dimensional metamaterials supporting Fano resonances.

## 5 Conclusion

In this thesis, the fundamental properties of Fano resonances in plasmonic nanostructures, and more generally in non-conservative systems, have been investigated. In particular, I have developed an *ab initio* framework to describe their properties. From Maxwell's equations and using Feshbach formalism of projection operators, a general analytical formula for the spectral response of such systems has been derived. The approach developed here overcomes the theoretical difficulty of dealing with non-hermitian operators, a characteristic feature of plasmonic systems which was not considered in Fano's original work. An equivalence between the derived resonance formula and the model of two coupled oscillators has been drawn, which confirms the general character of the developed framework.

The study of Fano resonant plasmonic systems requires three-dimensional full-field electromagnetic calculations. An original surface integral formulation for light scattering by periodic structures has therefore been developed and implemented. With this versatile numerical method, a very large variety of geometries can be simulated, including two-dimensional arrays of individual nanostructures on a substrate or in multilayered backgrounds, which is a situation often encountered in experimental conditions. The surface discretization using finite elements provides a high flexibility, allowing the investigation of irregular shapes. Thanks to the singularity subtraction technique, insights into the extreme near-field of the scatterers as well as into the corresponding far-field can be obtained with great accuracy. This particular advantage of the surface integral formulation compared to other numerical methods enables the accurate study of all the different aspects of Fano resonances in realistic plasmonic systems. The SIE method shows a very large potential for further extensions. Between publication of the original work and the redaction of this thesis, advances have been made in its application to plasmonics [148], proposing in particular alternate combinations of the electric field integral equation and the magnetic field integral equation for improved convergence [149]. It has also been extended to the non-linear regime for the study of second-harmonic generation [150]. Another possibility is to replace the Green's function for a homogeneous

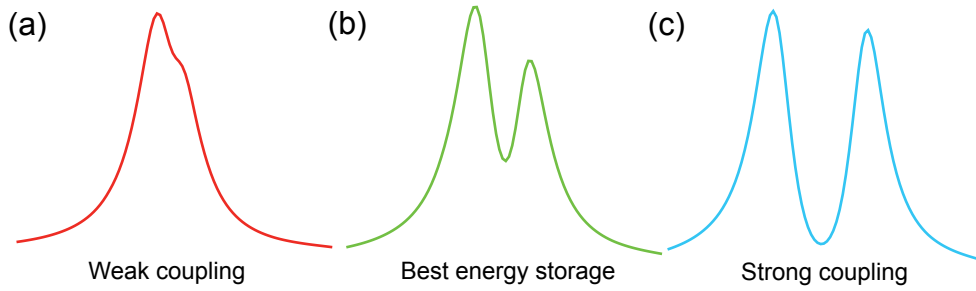


Figure 5.1: Fano resonances exhibit three coupling regimes: (a) weak coupling regime, (b) regime of best electromagnetic energy storage, (c) strong coupling regime.

background with the Green’s function for a stratified medium, which can be readily computed in non-periodic [151] and periodic systems [152, 153]. Although the current version of the SIE method can simulate stratified backgrounds with appropriate use of the periodicity in two dimensions, it cannot handle such background for periodicities in one dimension, which would be useful for *e.g.* the study of plasmonic waveguides [154]. Besides, including the stratified geometry directly in the computation of the Green’s function would drastically reduce the size of the matrix system to solve, because it would not require the discretization of planar surfaces over the entire unit cell.

It has then been shown that the line shape of Fano resonances satisfy the predictions of the *ab initio* theory in a broad variety of plasmonic nanostructures, and a methodology to tailor their optical response was provided. The far-field spectra have also been related to the near-field distributions of the bright and dark modes, as well as to their coupling. It has also been shown that Fano resonances can be decomposed into three coupling regimes (Fig. 5.1): in the weak coupling regime, a very high sensitivity to the opening of a radiative channel for the dark mode is observed. An optimal regime of highest electromagnetic field enhancement is obtained only when the in and out-coupling balance intrinsic losses. For stronger coupling, the specific features of Fano resonances are altered.

The knowledge of the mechanisms of Fano resonances acquired from these analytical and numerical studies has been translated to the optimization of nanoplasmonic systems for a broad range of applications involving Fano resonances. It has been shown in particular how the best coupling regime for a specific application can be chosen. In the weak coupling regime [Fig. 5.1(a)], radiative losses of the dark mode are almost suppressed. Introducing gain in such a system would increase the Fano resonance modulation depth, to threshold and laser emission [20]. In this regime, it has also been shown that the modulation depth is a physical value extremely sensitive to the modes coupling, which can be used for nanoscale plasmon rulers to measure nanometric displacements [126, 127]. In the intermediate regime [Fig. 5.1(b)], the best electromagnetic field enhancement is obtained and the devices are optimized for second harmonic generation [146], as well as for surface enhanced Raman scattering [41] and antenna-based trapping [147] for

---

biomolecular recognition. The sensitivity of Fano-resonant systems to local perturbations of the refractive index has then be discussed [36, 40]. Higher figures of merit than conventional plasmon resonances can be obtained because the contribution of radiative and non-radiative losses to the spectral width can be controlled. This analysis has finally led to the introduction of a new figure of merit for refractive index sensors depending only on the intrinsic properties of the resonant mode, enabling the comparison between Fano-resonant systems.

Fano resonances have very recently become a topic of particularly high interest in nanophotonics for their potential to surpass the efficiency of conventional plasmon resonances [14, 15]. A general understanding of Fano-resonant plasmonic systems has emerged from this thesis, which should ultimately lead to optimized applications in switching and optical communications, biological and chemical sensing based on this phenomenon. Together with the tremendous progresses that have recently been made on original and low-cost fabrication techniques, characterization techniques and devices integration, the road is now open towards practical implementations of nanoscale devices for industrial applications [14, 15, 110, 155].





# A Derivation of specific equations

This Appendix provides some additional derivation details that were omitted in the main text for clarity

## A.1 Classical equivalent of Fano resonance formula

The amplitude of the response of system B is given by:

$$c_b \simeq \frac{\omega_d^2 - \omega^2}{\mathcal{L}_d(\omega_d^2 - \omega^2) - g^2} \hat{f}. \quad (\text{A.1})$$

We introduce the following shortcut notations:  $x = \text{Re}(\mathcal{L}_d)$  and  $y = \text{Im}(\mathcal{L}_d)$ . We then have:

$$c_b = \frac{\omega_d^2 - \omega^2}{(x + iy)(\omega_d^2 - \omega^2) - g^2} \hat{f} \quad (\text{A.2})$$

$$= \frac{\omega_d^2 - \omega^2}{[x(\omega_d^2 - \omega^2) - g^2] + iy(\omega_d^2 - \omega^2)} \hat{f}, \quad (\text{A.3})$$

so that

$$|c_b|^2 = \frac{(\omega_d^2 - \omega^2)^2 |\hat{f}|^2}{(x^2 + y^2)(\omega_d^2 - \omega^2)^2 + g^4 - 2g^2x(\omega_d^2 - \omega^2)} \quad (\text{A.4})$$

$$= \frac{|\hat{f}|^2}{x^2 + y^2} \frac{(\omega_d^2 - \omega^2)^2}{(\omega_d^2 - \omega^2 - \frac{g^2x}{x^2+y^2})^2 + \frac{g^4}{x^2+y^2} - \frac{g^4x^2}{(x^2+y^2)^2}}. \quad (\text{A.5})$$

Defining  $\Gamma = g^2y/(x^2 + y^2)$  and  $\Delta = -g^2x/[\omega_d(x^2 + y^2)]$ , it leads to:

$$|c_b|^2 = \frac{|\hat{f}|^2}{x^2 + y^2} \frac{(\omega_d^2 - \omega^2)^2}{(\omega_d^2 - \omega^2 + \omega_d\Delta)^2 + \Gamma^2}. \quad (\text{A.6})$$

## Appendix A. Derivation of specific equations

---

Finally, by defining  $q = \omega_d \Delta / \Gamma$  and  $\kappa = (\omega^2 - \omega_d^2 - \omega_d \Delta) / \Gamma$ :

$$|c_b|^2 = \frac{|\hat{f}|^2}{x^2 + y^2} \frac{(\kappa + q)^2}{\kappa^2 + 1}. \quad (\text{A.7})$$

On the other hand, the amplitude of the response of oscillator D is given by:

$$c_d = \frac{-g}{\omega_d^2 - \omega^2} c_b = \frac{-g}{\mathcal{L}_d(\omega_d^2 - \omega^2) - g^2} \hat{f}, \quad (\text{A.8})$$

so that

$$|c_d|^2 = \frac{|\hat{f}|^2}{x^2 + y^2} \frac{g^2}{(\omega_d^2 - \omega^2 + \omega_d \Delta)^2 + \Gamma^2}, \quad (\text{A.9})$$

and finally:

$$|c_d|^2 = \frac{|\hat{f}|^2 g^2}{(x^2 + y^2) \Gamma^2} \frac{1}{\kappa^2 + 1} \quad (\text{A.10})$$

$$= \frac{|\hat{f}|^2 (x^2 + y^2)}{g^2 y^2} \frac{1}{\kappa^2 + 1}. \quad (\text{A.11})$$

## A.2 Generalized Fano formula in non-reciprocal systems

The amplitude of the response of system B is given by:

$$c_b \simeq \frac{\omega_d^2 + i\gamma_d \omega - \omega^2}{\mathcal{L}_d(\omega_d^2 + i\gamma_d \omega - \omega^2) - g^2} \hat{f}. \quad (\text{A.12})$$

We introduce the following shortcut notations:  $x = \text{Re}(\mathcal{L}_d)$ ,  $y = \text{Im}(\mathcal{L}_d)$  and  $\Gamma_i = \gamma_d \omega_d$ . We then have:

$$c_b = \frac{\omega_d^2 + i\Gamma_i - \omega^2}{(x + iy)(\omega_d^2 + i\Gamma_i - \omega^2) - g^2} \hat{f} \quad (\text{A.13})$$

$$= \frac{\omega_d^2 + i\Gamma_i - \omega^2}{[x(\omega_d^2 - \omega^2) - y\Gamma_i - g^2] + i[y(\omega_d^2 - \omega^2) + x\Gamma_i]} \hat{f}, \quad (\text{A.14})$$

so that

$$|c_b|^2 = \frac{[(\omega_d^2 - \omega^2)^2 + \Gamma_i^2] |\hat{f}|^2}{(x^2 + y^2)(\omega_d^2 - \omega^2)^2 + (y\Gamma_i + g^2)^2 - 2xg^2(\omega_d^2 - \omega^2) + (x\Gamma_i)^2} \quad (\text{A.15})$$

$$= \frac{|\hat{f}|^2}{x^2 + y^2} \frac{(\omega_d^2 - \omega^2)^2 + \Gamma_i^2}{(\omega_d^2 - \omega^2 - \frac{g^2 x}{x^2 + y^2})^2 + \frac{g^4 y^2}{(x^2 + y^2)^2} + \Gamma_i^2 + \frac{2g^2 y \Gamma_i}{x^2 + y^2}}, \quad (\text{A.16})$$

### A.3. Electromagnetic Fano resonance formula

Defining  $\Delta = -g^2 x / [\omega_d(x^2 + y^2)]$ ,  $\Gamma_c = g^4 y^2 / (x^2 + y^2)$  and  $\Gamma = \Gamma_c + \Gamma_i$ , it leads to

$$|c_b|^2 = \frac{|\hat{f}|^2}{x^2 + y^2} \frac{(\omega_d^2 - \omega^2)^2 + \Gamma_i^2}{(\omega_d^2 - \omega^2 + \omega_d \Delta)^2 + \Gamma^2}. \quad (\text{A.17})$$

Finally, by defining  $q = \omega_d \Delta / \Gamma$ ,  $b = \Gamma_i^2 / \Gamma^2$  and  $\kappa = (\omega^2 - \omega_d^2 - \omega_d \Delta) / \Gamma$ :

$$|c_b|^2 = \frac{|\hat{f}|^2}{x^2 + y^2} \frac{(\kappa + q)^2 + b}{\kappa^2 + 1}. \quad (\text{A.18})$$

On the other hand, the amplitude of the response of oscillator D is given by:

$$c_d = \frac{-g}{\omega_d^2 + i\gamma_d \omega - \omega^2} c_b = \frac{-g}{\mathcal{L}_d(\omega_d^2 + i\gamma_d \omega - \omega^2) - g^2} \hat{f}, \quad (\text{A.19})$$

so that

$$|c_d|^2 = \frac{|\hat{f}|^2}{x^2 + y^2} \frac{g^2}{(\omega_d^2 - \omega^2 + \omega_d \Delta)^2 + \Gamma^2}, \quad (\text{A.20})$$

and finally:

$$|c_d|^2 = \frac{|\hat{f}|^2 g^2}{(x^2 + y^2) \Gamma^2} \frac{1}{\kappa^2 + 1} \quad (\text{A.21})$$

$$= \frac{|\hat{f}|^2 \Gamma_c}{y^2 (\Gamma_c + \Gamma_i)^2} \frac{1}{\kappa^2 + 1}. \quad (\text{A.22})$$

### A.3 Electromagnetic Fano resonance formula

The ratio of the optical response of the total field  $|\mathbf{E}\rangle$  to the one of the continuum  $|P\mathbf{E}_b\rangle$  satisfies:

$$\frac{|\langle g|T|\mathbf{E}\rangle|^2}{|\langle g|T|P\mathbf{E}_b\rangle|^2} = \frac{(\chi^2 + \Gamma_i^2 + \Gamma_c \chi q')^2 + \Gamma_c^2 \Gamma_i^2 q'^2}{(\chi^2 + \Gamma_i^2 + \Gamma_c \Gamma_i)^2 + \Gamma_c^2 \chi^2} \quad (\text{A.23})$$

$$= \frac{(\chi^2 + \Gamma_i^2)^2 + 2(\chi^2 + \Gamma_i^2) \Gamma_c \chi q' + \Gamma_c^2 \chi^2 q'^2 + \Gamma_c^2 \Gamma_i^2 q'^2}{(\chi^2 + \Gamma_i^2)^2 + (\Gamma_c \Gamma_i)^2 + 2(\chi^2 + \Gamma_i^2) \Gamma_c \Gamma_i + \Gamma_c^2 \chi^2} \quad (\text{A.24})$$

$$= \frac{\chi^2 + \Gamma_i^2 + 2\Gamma_c \chi q' + \frac{\Gamma_c^2 \chi^2 q'^2 + \Gamma_c^2 \Gamma_i^2 q'^2}{\chi^2 + \Gamma_i^2}}{\chi^2 + \Gamma_i^2 + \frac{\Gamma_c^2 \chi^2}{\chi^2 + \Gamma_i^2} + 2\Gamma_c \Gamma_i + \frac{(\Gamma_c \Gamma_i)^2}{\chi^2 + \Gamma_i^2}} \quad (\text{A.25})$$

$$= \frac{\chi^2 + \Gamma_i^2 + 2\Gamma_c \chi q' + \Gamma_c^2 q'^2}{\chi^2 + (\Gamma_c + \Gamma_i)^2} \quad (\text{A.26})$$

## Appendix A. Derivation of specific equations

---

Defining  $\Gamma = \Gamma_c + \Gamma_i$ , this leads to:

$$\frac{|\langle g|T|\mathbf{E}\rangle|^2}{|\langle g|T|P\mathbf{E}_b\rangle|^2} = \frac{\frac{\chi^2}{\Gamma^2} + \frac{2\Gamma_c\chi q'}{\Gamma^2} + \frac{\Gamma_i^2}{\Gamma^2} + \frac{\Gamma_c^2 q'^2}{\Gamma^2}}{\frac{\chi^2}{\Gamma^2} + 1} \quad (\text{A.27})$$

$$= \frac{\left(\frac{\chi}{\Gamma} + \frac{q'}{1+\Gamma_i/\Gamma_c}\right)^2 + \frac{\Gamma_i^2}{\Gamma^2}}{\frac{\chi^2}{\Gamma^2} + 1}. \quad (\text{A.28})$$

Finally, by defining  $q = q'/(1 + \Gamma_i/\Gamma_c)$ ,  $b = \Gamma_i^2/\Gamma^2$  and  $\kappa = \chi/\Gamma$ , we obtain:

$$\frac{|\langle g|T|\mathbf{E}\rangle|^2}{|\langle g|T|P\mathbf{E}_b\rangle|^2} = \frac{(\kappa + q)^2 + b}{\kappa^2 + 1}. \quad (\text{A.29})$$

### A.4 Field enhancement

The non-normalized total field  $|\tilde{\mathbf{E}}\rangle$  satisfies:

$$|\tilde{\mathbf{E}}\rangle = |P\mathbf{E}_b\rangle + \frac{\langle \mathbf{E}_d | \underline{\mathcal{M}}_\omega | P\mathbf{E}_b \rangle}{\omega_d^2 + 2i\gamma_d\omega_d - \omega^2 + \omega_d\Delta} (\underline{G}_b P \underline{\mathcal{M}}_\omega |\mathbf{E}_d\rangle - |\mathbf{E}_d\rangle). \quad (\text{A.30})$$

It is related to the normalized total field by:

$$|\mathbf{E}\rangle = f^{-1}(\chi) \sqrt{\frac{\xi^2}{\xi^2 + 1}} |\tilde{\mathbf{E}}\rangle, \quad (\text{A.31})$$

so that

$$Q|\mathbf{E}\rangle = f^{-1}(\chi) \sqrt{\frac{\xi^2}{\xi^2 + 1}} \frac{\langle \mathbf{E}_d | \underline{\mathcal{M}}_\omega | P\mathbf{E}_b \rangle |\mathbf{E}_d\rangle}{\omega_d^2 + 2i\gamma_d\omega_d - \omega^2 + \omega_d\Delta}. \quad (\text{A.32})$$

Finally, considering  $|\langle \mathbf{E}_d | \mathbf{E}_d \rangle|^2 = 1$ :

$$|\langle \mathbf{E} | Q | \mathbf{E} \rangle|^2 = f^{-2}(\chi) \frac{\xi^2}{\xi^2 + 1} \frac{|\langle \mathbf{E}_d | \underline{\mathcal{M}}_\omega | P\mathbf{E}_b \rangle|^2}{\chi^2 + \Gamma_i^2} \quad (\text{A.33})$$

$$= \frac{\chi^2 + \Gamma_i^2}{(\Gamma_c\chi)^2} \frac{|\langle \mathbf{E}_d | \underline{\mathcal{M}}_\omega | P\mathbf{E}_b \rangle|^2}{\frac{(\chi^2 + \Gamma_i^2 + \Gamma_c\Gamma_i)^2}{(\Gamma_c\chi)^2} + 1} \quad (\text{A.34})$$

$$= \frac{|\langle \mathbf{E}_d | \underline{\mathcal{M}}_\omega | P\mathbf{E}_b \rangle|^2 (\chi^2 + \Gamma_i^2)}{(\chi^2 + \Gamma_i^2 + \Gamma_c\Gamma_i)^2 + \Gamma_c^2\chi^2} \quad (\text{A.35})$$

$$= \frac{1}{\kappa^2 + 1} \frac{|\langle \mathbf{E}_d | \underline{\mathcal{M}}_\omega | P\mathbf{E}_b \rangle|^2}{(\Gamma_c + \Gamma_i)^2}. \quad (\text{A.36})$$

## A.5 Complex integrals

The integral involved in the expressions of the frequency shift and asymmetry parameter is given by:

$$\mathcal{I} = \Gamma_b^2 \mathcal{P} \int \frac{d\omega'}{(\omega'^2 - \omega_d^2)[(\omega'^2 - \omega_b^2)^2 + \Gamma_b^2]}, \quad (\text{A.37})$$

where  $\omega_s$  is the bright mode's resonance frequency and  $\Gamma_s$  its resonance width. After the change of variables  $\omega'' = \omega'^2$  it becomes:

$$\mathcal{I} \simeq \frac{\Gamma_b^2}{2\omega_d} \mathcal{P} \int \frac{d\omega''}{(\omega'' - \omega_d^2)(\omega'' - \omega_b^2 + i\Gamma_b)(\omega'' - \omega_b^2 - i\Gamma_b)}. \quad (\text{A.38})$$

In order to calculate the integral  $\mathcal{I}$ , we assume that  $\omega''$  is a complex variable. The integration path in the complex plane is a closed path following the real axis and half a circle of infinite radius on the lower complex plane, including poles at  $\omega_b^2 + i\Gamma_b$  and  $\omega_b^2 - i\Gamma_b$ . Using the residue theorem, one obtains:

$$\mathcal{I} \simeq \frac{\pi i \Gamma_b^2}{2\omega_d} \left( \frac{1}{(\omega_d^2 - \omega_b^2)^2 + \Gamma_b^2} + \frac{2}{2i\Gamma_b(\omega_b^2 + i\Gamma_b - \omega_d^2)} \right) \quad (\text{A.39})$$

$$= \frac{\pi \Gamma_b}{2\omega_d} \left( \frac{i\Gamma_b + \omega_b^2 - i\Gamma_b - \omega_d^2}{(\omega_d^2 - \omega_b^2)^2 + \Gamma_b^2} \right) \quad (\text{A.40})$$

$$= \frac{\pi \Gamma_b}{2\omega_d} \frac{\omega_b^2 - \omega_d^2}{(\omega_d^2 - \omega_b^2)^2 + \Gamma_b^2}. \quad (\text{A.41})$$



# B List of symbols

Symbol	Name	Value
$c_0$	Speed of light in vacuum	$299792458 \text{ m} \cdot \text{s}^{-1}$
$\epsilon_0$	Electric permittivity of vacuum	$8.854187817... \times 10^{-12} \text{ A} \cdot \text{s} \cdot \text{V}^{-1} \cdot \text{m}^{-1}$
$\mu_0$	Magnetic permeability of vacuum	$4\pi \times 10^{-7} \text{ N} \cdot \text{A}^{-2}$
$Z_0$	Impedance of vacuum	$376.7403134... \Omega$
$\hbar$	Planck's constant	$1.054571726... \times 10^{-34} \text{ J} \cdot \text{s}$

Table B.1: Natural constants used in this thesis.

Symbol	Physical quantity
$\psi_d$	Discrete state in an atomic system
$E_d$	Energy of the discrete state
$\psi_E, \psi_{1E}, \psi_{2E}, \dots$	Continua of states
$E$	Energy spectrum of the continua
$V_E$	Coupling constant
$H$	Hamiltonian of the atomic system
$\chi_E, \chi_{1E}, \chi_{2E}, \dots$	Total wavefunction
$a, b_E$	Expansion coefficients of the eigenvectors
$\epsilon$	Reduced energy / dielectric permittivity
$\Delta\phi$	Fano resonance phase shift
$\mathcal{P}$	Principal part
$F(E)$	Fano resonance energy shift
$\Gamma$	Spectral width of Fano resonance
$q$	Asymmetry parameter
$\Psi_d$	Modified discrete state
$T$	Transition operator from an initial state

Table B.2: Physical quantities introduced in Section 1.1.1 and their symbolic representation.

## Appendix B. List of symbols

---

Symbol	Physical quantity
$c$	Resonance amplitude
$\omega_0$	Resonance frequency
$\gamma_0$	Resonance damping
$t$	Time
$h^+$	Incoming wave amplitude
$h^-$	Outgoing wave amplitude
$\gamma$	External leakage/ Drude model damping
$\iota, \eta$	Coupling constants
$B$	Background reflection
$\phi$	Phase shift of background reflection
$\omega$	Angular frequency
$C_{\text{sct}}$	Scattering cross section
$C_{\text{abs}}$	Absorption cross section
$\lambda$	Vaccum wavelength

Table B.3: Physical quantities introduced in Section 1.1.2 and their symbolic representation.

Symbol	Physical quantity
$\omega_b$	Oscillator B/ bright mode's resonance frequency
$\gamma_b$	Oscillator B damping constant
$\omega_d$	Oscillator D/ dark mode's resonance frequency
$\gamma_d$	Oscillator D/ dark mode's damping constant
$x_b, x_d$	Positions from rest
$g$	Oscillators coupling
$f$	External force
$c_b, c_d$	Frequency dependent amplitudes of the oscillators
$\mathcal{L}$	Linear differential operator representing equations of motion
$\mathcal{L}_\omega$	Fourier component of $\mathcal{L}$
$\mathcal{L}_d$	$\mathcal{L}_\omega$ evaluated at $\omega_d$
$\Delta$	Fano resonance frequency shift
$\kappa$	Reduced frequency
$\sigma_f$	Fano resonance line shape in classical systems
$\Gamma_i$	Part of Fano resonance width related to intrinsic losses
$\Gamma_c$	Part of Fano resonance width related to coupling
$\sigma_a$	Generalized Fano resonance line shape

Table B.4: Physical quantities introduced in Section 1.2 and their symbolic representation.



---

Symbol	Physical quantity
$\mathbf{E}$	Electric field
$\mathbf{r} = (x, y, z)$	Coordinate system
$\underline{\mathcal{M}}$	Electromagnetic equivalent of the Hamiltonian
$\underline{P}$	Projection operator to radiative fields
$Q$	Projection operator to radiative fields
$z_d$	Dark mode's complex frequency
$\mathbf{I}$	Identity operator
$\underline{\underline{G}}_b$	Green's dyadic of the continuum
$ \mathbf{E}_d\rangle$	Dark mode
$ P\mathbf{E}_b\rangle$	Continuum
$ \tilde{\mathbf{E}}\rangle$	Total field
$ \mathbf{E}\rangle$	Normalized total field
$ \mathbf{J}\rangle$	Source current field
$\Gamma_b$	Bright mode's resonance frequency
$\omega_p$	Drude model plasma frequency
$W_b$	Bright mode width in frequency units
$W_a$	Fano resonance width in frequency units
$\sigma_b$	Bright mode resonance line shape
$\sigma_{\text{tot}}$	Line shape of the system bright/dark mode
$\omega_a$	Fano resonance frequency
$\gamma_b$	Bright mode width in frequency units for a lorentzian profile
$\gamma_i$	Part of Fano resonance width related to intrinsic losses in frequency units
$\gamma_i$	Part of Fano resonance width related to coupling in frequency units
$\gamma_a$	Fano resonance width for a profile given as a function of the frequency

---

Table B.5: Physical quantities introduced in Section 1.3, Chapters 3 and 4, and their symbolic representation.

## Appendix B. List of symbols

---

Symbol	Physical quantity
$\mathbf{j}$	Source current density
$\mathbf{H}$	Magnetic field
$\mathbf{E}_n^{\text{inc}}$	Incident electric field
$\mathbf{H}_n^{\text{inc}}$	Incident magnetic field
$\mathbf{E}_n^{\text{scat}}$	Scattered electric field
$\mathbf{H}_n^{\text{scat}}$	Scattered magnetic field
$V_n$	Domain $n$
$\epsilon_n$	Relative dielectric permittivity in domain $n$
$\mu_n$	Relative magnetic permeability in domain $n$
$\Omega$	Unit cell
$\mathbf{a}_i$	Lattice vector
$\partial V_n$	Boundary surface of domain $n$
$\hat{\mathbf{n}}_n$	Outward-pointing normal unit vector on $\partial V_n$
$\mathbf{J}_n$	Electric equivalent surface current on $\partial V_n$
$\mathbf{M}_n$	Magnetic equivalent surface current on $\partial V_n$
$\underline{\underline{G}}_n$	Green's dyadic of domain $n$
$G_n$	Scalar Green's function of domain $n$
$k_n$	Wavenumber in domain $n$
$\mathbf{k}$	Floquet–Bloch vector
$\underline{\underline{G}}_{n,\mathbf{k}}$	Pseudo-periodic Green's dyadic
$G_{n,\mathbf{k}}$	Pseudo-periodic Green's function
$V_n^\Omega$	Intersection of domain $n$ with the unit cell
$\partial V_n^\Omega$	Intersection of the boundary surface with the unit cell
$\mathbf{E}_{n,\mathbf{k}}^{\text{inc}}$	Bloch component of incident electric field
$\mathbf{H}_{n,\mathbf{k}}^{\text{inc}}$	Bloch component of incident magnetic field
$\mathbf{E}_{n,\mathbf{k}}^{\text{scat}}$	Bloch component of scattered electric field
$\mathbf{H}_{n,\mathbf{k}}^{\text{scat}}$	Bloch component of scattered magnetic field
$\mathbf{J}_{n,\mathbf{k}}$	Bloch component of $\mathbf{J}_n$
$\mathbf{M}_{n,\mathbf{k}}$	Bloch component of $\mathbf{M}_n$
$\mathbf{t}$	Translation lattice vector
$\mathbf{u}$	Reciprocal lattice vector

Table B.6: Physical quantities introduced in Chapter 2 and their symbolic representation.

# Bibliography

- [1] C. Cohen-Tannoudji, J. Dupont-Roc, and G. Grynberg, *Photons & Atoms* (Wiley–VCH, 2004).
- [2] B. E. A. Saleh and M. C. Teich, *Fundamentals of Photonics* (John Wiley & Sons, 1991).
- [3] J. D. Joannopoulos, P. R. Villeneuve, and S. H. Fan, “Photonic crystals: Putting a new twist on light,” *Nature* **386**, 143–149 (1997).
- [4] R. W. Wood, “On a remarkable case of uneven distribution of light in a diffraction grating spectrum,” *Proc. R. soc. Lond. Ser. A* **18**, 269–275 (1902).
- [5] R. H. Ritchie, “Plasma Losses by Fast Electrons in Thin Films,” *Phys. Rev.* **106**, 874–881 (1957).
- [6] R. H. Ritchie, E. T. Arakawa, J. J. Cowan, and R. N. Hamm, “Surface–Plasmon Resonance Effect in Grating Diffraction,” *Phys. Rev. Lett.* **21**, 1530–1533 (1968).
- [7] S. A. Maier, *Plasmonics: Fundamentals and Applications* (Springer Science, 2007).
- [8] J. Mock, M. Barbic, D. Smith, D. Schultz, and S. Schultz, “Shape effects in plasmon resonance of individual colloidal silver nanoparticles,” *J. Chem. Phys.* **116**, 6755–6759 (2002).
- [9] T. Ebbesen, H. Lezec, H. Ghaemi, T. Thio, and P. Wolff, “Extraordinary optical transmission through sub-wavelength hole arrays,” *Nature* **391**, 667–669 (1998).
- [10] S. Collin, G. Vincent, R. Haidar, N. Bardou, S. Rommeluere, and J.-L. Pelouard, “Nearly Perfect Fano Transmission Resonances Through Nanoslits Drilled in a Metallic Membrane,” *Phys. Rev. Lett.* **104**, 027401 (2010).
- [11] F. J. Garcia-Vidal, L. Martin-Moreno, T. W. Ebbesen, and L. Kuipers, “Light Passing Through Subwavelength Apertures,” *Rev. Mod. Phys.* **82**, 729–787 (2010).
- [12] W. L. Barnes, A. Dereux, and T. W. Ebbesen, “Surface plasmon subwavelength optics,” *Nature* **424**, 824–830 (2003).

## Bibliography

---

- [13] N. J. Halas, S. Lal, W.-S. Chang, S. Link, and P. Nordlander, “Plasmons in strongly coupled metallic nanostructures,” *Chem. Rev.* **111**, 3913–3961 (2011).
- [14] B. Luk’yanchuk, N. I. Zheludev, S. A. Maier, N. J. Halas, P. Nordlander, H. Giessen, and C. T. Chong, “The Fano resonance in plasmonic nanostructures and metamaterials,” *Nat. Mater.* **9**, 707–715 (2010).
- [15] A. E. Miroschnichenko, S. Flach, and Y. S. Kivshar, “Fano resonances in nanoscale structures,” *Rev. Mod. Phys.* **82**, 2257–2298 (2010).
- [16] U. Fano, “Some theoretical considerations on anomalous diffraction gratings,” *Phys. Rev.* **50**, 573 (1936).
- [17] U. Fano, “The theory of anomalous diffraction gratings and of quasi-stationary waves on metallic surfaces (Sommerfeld’s waves),” *J. Opt. Soc. Am.* **31**, 213–222 (1941).
- [18] U. Fano, “Effects of Configuration Interaction on Intensities and Phase Shifts,” *Phys. Rev.* **124**, 1866 (1961).
- [19] F. Pardo, P. Bouchon, R. Haidar, and J.-L. Pelouard, “Light funneling mechanism explained by magnetoelectric interference,” *Phys. Rev. Lett.* **107**, 093902 (2011).
- [20] N. I. Zheludev, S. L. Prosvirnin, N. Papasimakis, and V. A. Fedotov, “Lasing spaser,” *Nat. Photonics* **2**, 351–354 (2008).
- [21] M. J. Dicken, K. Aydin, I. M. Pryce, L. A. Sweatlock, E. M. Boyd, S. Walavalkar, J. Ma, and H. A. Atwater, “Frequency Tunable Near-Infrared Metamaterials Based on VO<sub>2</sub> Phase Transition,” *Opt. Express* **17**, 18330–18339 (2009).
- [22] Z. L. Samson, K. F. MacDonald, F. De Angelis, B. Gholipour, K. Knight, C. C. Huang, E. Di Fabrizio, D. W. Hewak, and N. I. Zheludev, “Metamaterial Electro-Optic Switch of Nanoscale Thickness,” *Appl. Phys. Lett.* **96** (2010).
- [23] A. E. Nikolaenko, F. De Angelis, S. A. Boden, N. Papasimakis, P. Ashburn, E. Di Fabrizio, and N. I. Zheludev, “Carbon nanotubes in a photonic metamaterial,” *Phys. Rev. Lett.* **104**, 153902 (2010).
- [24] K. J. Boller, A. Imamoglu, and S. E. Harris, “Observation of electromagnetically induced transparency,” *Phys. Rev. Lett.* **66**, 2593–2596 (1991).
- [25] S. Zhang, D. A. Genov, Y. Wang, M. Liu, and X. Zhang, “Plasmon-Induced Transparency in Metamaterials,” *Phys. Rev. Lett.* **101**, 047401 (2008).
- [26] N. Liu, L. Langguth, T. Weiss, J. Kaestel, M. Fleischhauer, T. Pfau, and H. Giessen, “Plasmonic analogue of electromagnetically induced transparency at the drude damping limit,” *Nat. Mater.* **8**, 758–762 (2009).

- 
- [27] C. Wu, A. B. Khanikaev, and G. Shvets, “Broadband Slow Light Metamaterial Based on a Double-Continuum Fano Resonance,” *Phys. Rev. Lett.* **106**, 107403 (2011).
- [28] C. L. G. Alzar, M. A. G. Martinez, and P. Nussenzveig, “Classical Analog of Electromagnetically Induced Transparency,” *Am. J. Phys.* **70**, 37–41 (2002).
- [29] Y. S. Joe, A. M. Satanin, and C. S. Kim, “Classical analogy of Fano resonances,” *Phys. Scr.* **74**, 259–266 (2006).
- [30] S. H. Fan and J. D. Joannopoulos, “Analysis of guided resonances in photonic crystal slabs,” *Phys. Rev. B* **65**, 235112 (2002).
- [31] S. H. Fan, W. Suh, and J. D. Joannopoulos, “Temporal Coupled-Mode Theory for the Fano Resonance in Optical Resonators,” *J. Opt. Soc. Am. A-Opt. Image Sci. Vis.* **20**, 569–572 (2003).
- [32] Z. Ruan and S. Fan, “Temporal Coupled Mode Theory for Fano Resonance in Light Scattering by a Single Obstacle,” *J. Phys. Chem. C* **114**, 7324–7329 (2010).
- [33] M. Shapiro, “Electromagnetically Induced Transparency with Structured Multicontinua,” *Phys. Rev. A* **75**, 013424 (2007).
- [34] V. Giannini, Y. Francescato, H. Amrania, C. C. Phillips, and S. A. Maier, “Fano resonances in nanoscale plasmonic systems: A parameter-free modeling approach,” *Nano Lett.* **11**, 2835–2840 (2011).
- [35] N. A. Mirin, K. Bao, and P. Nordlander, “Fano Resonances in Plasmonic Nanoparticle Aggregates,” *J. Phys. Chem. A* **113**, 4028–4034 (2009).
- [36] F. Hao, P. Nordlander, Y. Sonnefraud, P. Van Dorpe, and S. A. Maier, “Tunability of Subradiant Dipolar and Fano-Type Plasmon Resonances in Metallic Ring/Disk Cavities: Implications for Nanoscale Optical Sensing,” *ACS Nano* **3**, 643–652 (2009).
- [37] N. Verellen, Y. Sonnefraud, H. Sobhani, F. Hao, V. V. Moshchalkov, P. Van Dorpe, P. Nordlander, and S. A. Maier, “Fano resonances in individual coherent plasmonic nanocavities,” *Nano Lett.* **9**, 1663–1667 (2009).
- [38] N. Liu, T. Weiss, M. Mesch, L. Langguth, U. Eigenthaler, M. Hirscher, C. Sönnichsen, and H. Giessen, “Planar metamaterial analogue of electromagnetically induced transparency for plasmonic sensing,” *Nano Lett.* **10**, 1103–1107 (2010).
- [39] N. Verellen, P. Van Dorpe, C. Huang, K. Lodewijks, G. A. E. Vandenbosch, L. Lagae, and V. V. Moshchalkov, “Plasmon Line Shaping Using Nanocrosses for High Sensitivity Localized Surface Plasmon Resonance Sensing,” *Nano Lett.* **11**, 391–397 (2011).

## Bibliography

---

- [40] C. Wu, A. B. Khanikaev, R. Adato, N. Arju, A. A. Yanik, H. Altug, and G. Shvets, “Fano-resonant asymmetric metamaterials for ultrasensitive spectroscopy and identification of molecular monolayers,” *Nat. Mater.* **11**, 69–75 (2012).
- [41] J. Ye, F. Wen, H. Sobhani, J. B. Lassiter, P. V. Dorpe, P. Nordlander, and N. J. Halas, “Plasmonic nanoclusters: Near field properties of the fano resonance interrogated with sers,” *Nano Lett.* **12**, 1660–1667 (2012).
- [42] I. M. Pryce, K. Aydin, Y. A. Kelaita, R. M. Briggs, and H. A. Atwater, “Highly strained compliant optical metamaterials with large frequency tunability,” *Nano Lett.* **10**, 4222–4227 (2010).
- [43] B. Gallinet and O. J. F. Martin, “Ab initio theory of Fano resonances in plasmonic nanostructures and metamaterials,” *Phys. Rev. B* **83**, 235427 (2011).
- [44] B. Gallinet and O. J. F. Martin, “Ab initio engineering of Fano resonances,” *Proc. SPIE* **8096**, 80961R (2011).
- [45] L. Rayleigh, “On the dynamical theory of gratings,” *Proc. R. soc. Lond. Ser. A* **79**, 399–416 (1907).
- [46] H. Beutler, “About the absorption series of argon, krypton and xenon to the term of ionisation boundaries between  $(2)P(3/2)(0)$  and  $(2)P(1/2)(0)$ ,” *Z. Phys.* **93**, 177–196 (1935).
- [47] W. E. Lamb and R. C. Retherford, “Fine structure of the hydrogen atom. part ii,” *Phys. Rev.* **81**, 222–232 (1951).
- [48] U. Fano and J. W. Cooper, “Line profiles in the far-uv absorption spectra of the rare gases,” *Phys. Rev.* **137**, A 1364 – A 1378 (1965).
- [49] D. Maystre, *Electromagnetic Surface Modes* (A. D. Boardman, ed., Wiley, Chichester, UK, 1982).
- [50] S. Fan, “Sharp asymmetric line shapes in side-coupled waveguide-cavity systems,” *App. Phys. Lett.* **80**, 908 (2002).
- [51] L. Verslegers, Z. Yu, Z. Ruan, P. B. Catrysse, and S. Fan, “From electromagnetically induced transparency to superscattering with a single structure: A coupled-mode theory for doubly resonant structures,” *Phys. Rev. Lett.* **108**, 083902 (2012).
- [52] R. Taubert, M. Hentschel, J. Kästel, and H. Giessen, “Classical analog of electromagnetically induced absorption in plasmonics,” *Nano Lett.* **12**, 1367–1371 (2012).
- [53] H. Feshbach, “A unified theory of nuclear reactions .2.” *Ann. Phys.* **19**, 287–313 (1962).

- 
- [54] T. F. O'Malley and S. Geltman, "Compound-atom states for 2-electron systems," *Phys. Rev.* **137**, A1344 (1965).
- [55] A. K. Bhatia and A. Temkin, "Line-Shape Parameters for P-1 Feshbach Resonances in He and Li+," *Phys. Rev. A* **29**, 1895–1900 (1984).
- [56] L. Novotny and B. Hecht, *Principles of Nano-Optics* (Cambridge University Press, 2006).
- [57] C. F. Bohren and D. R. Huffman, *Absorption and Scattering of Light by Small Particles* (Wiley-Interscience, 1983).
- [58] B. Gallinet and O. J. F. Martin, "Scattering on Plasmonic Nanostructures Arrays Modeled with a Surface Integral Formulation," *Photonic Nanostruct.* **8**, 278–284 (2010).
- [59] B. Gallinet, A. M. Kern, and O. J. F. Martin, "Accurate and versatile modeling of electromagnetic scattering on periodic nanostructures with a surface integral approach," *J. Opt. Soc. Am. A* **27**, 2261–2271 (2010).
- [60] L. Li, "New formulation of the fourier modal method for crossed surface-relief gratings," *J. Opt. Soc. Am. A* **14**, 2758–2767 (1997).
- [61] K. Sakoda, *Optical properties of photonic crystals* (Springer, Berlin, 2005).
- [62] M. G. Moharam, E. B. Grann, D. A. Pommet, and T. K. Gaylord, "Formulation for stable and efficient implementation of the rigorous coupled-wave analysis of binary gratings," *J. Opt. Soc. Am. A* **12**, 1068–1076 (1995).
- [63] D. Whittaker and I. Culshaw, "Scattering-matrix treatment of patterned multilayer photonic structures," *Phys. Rev. B* **60**, 2610–2618 (1999).
- [64] S. Tikhodeev, A. Yablonskii, E. Muljarov, N. Gippius, and T. Ishihara, "Quasiguided modes and optical properties of photonic crystal slabs," *Phys. Rev. B* **66**, 045102 (2002).
- [65] K. Yee, "Numerical solution of initial boundary value problems involving Maxwell's equations in isotropic media," *IEEE Transactions on Antennas and Propagation* **14**, 302–307 (1966).
- [66] P. Monk, *Finite Element Methods for Maxwell's Equations* (Oxford U. Press, 2003).
- [67] J. Jin, *Finite Element Method in electromagnetics* (Wiley, 2002).
- [68] R. Petit, *Electromagnetic theory of gratings* (Springer-Verlag, 1980).
- [69] J. Chandezon, D. Maystre, and G. Raoult, "A new theoretical method for diffraction gratings and its numerical application," *J. Opt.-Nouv. Rev. Opt.* **11**, 235–241 (1980).

## Bibliography

---

- [70] A. Wirgin and R. Deleuil, “Theoretical and experimental investigation of a new type of blazed grating,” *J. Opt. Soc. Am.* **59**, 1348–1357 (1969).
- [71] T. Delort and D. Maystre, “Finite-element method for gratings,” *J. Opt. Soc. Am. A* **10**, 2592–2601 (1993).
- [72] B. T. Draine and P. J. Flatau, “Discrete-dipole approximation for scattering calculations,” *J. Opt. Soc. Am. A* **11**, 1491–1499 (1994).
- [73] O. J. F. Martin and N. B. Piller, “Electromagnetic scattering in polarizable backgrounds,” *Physical Review E* **58**, 3909–3915 (1998).
- [74] P. C. Chaumet, A. Rahmani, and G. W. Bryant, “Generalization of the coupled dipole method to periodic structures,” *Phys. Rev. B* **67**, 165404 (2003).
- [75] B. T. Draine and P. J. Flatau, “Discrete-dipole approximation for periodic targets: theory and tests,” *Journal of the Optical Society of America A-Optics Image Science and Vision* **25**, 2693–2703 (2008).
- [76] P. C. Chaumet and A. Sentenac, “Simulation of light scattering by multilayer cross-gratings with the coupled dipole method,” *J. Quant. Spectrosc. Radiat. Transf.* **110**, 409–414 (2009).
- [77] T. Eibert, J. Volakis, D. Wilton, and D. Jackson, “Hybrid FE/BI modeling of 3-D doubly periodic structures utilizing triangular prismatic elements and an MPIE formulation accelerated by the Ewald transformation,” *Antennas and Propagation, IEEE Transactions on* **47**, 843–850 (1999).
- [78] M. S. Yeung and E. Barouch, “Three-dimensional nonplanar lithography simulation using a periodic fast multipole method,” *Proceedings of the society of photo-optical instrumentation engineers (SPIE)* **3051**, 509–521 (1997).
- [79] M. S. Yeung, “Single integral equation for electromagnetic scattering by three-dimensional homogeneous dielectric objects,” *IEEE Trans. Antennas Propag.* **47**, 1615–1622 (1999).
- [80] F. J. García de Abajo and A. Howie, “Retarded field calculation of electron energy loss in inhomogeneous dielectrics,” *Phys. Rev. B* **65**, 115418 (2002).
- [81] A. M. Kern and O. J. F. Martin, “Surface integral formulation for 3D simulations of plasmonic and high permittivity nanostructures,” *J. Opt. Soc. Am. A* **26**, 732–740 (2009).
- [82] R. F. Harrington, *Field Computation by Moment Methods* (Macmillan, 1968).
- [83] N. Marly, D. De Zutter, and H. Pues, “A surface integral equation approach to the scattering and absorption of doubly periodic lossy structures,” *Electromagnetic Compatibility, IEEE Transactions on* **36**, 14–22 (1994).



- 
- [84] N. Marly, B. Baekelandt, D. De Zutter, and H. Poes, “Integral equation modeling of the scattering and absorption of multilayered doubly-periodic lossy structures,” *Antennas and Propagation, IEEE Transactions on* **43**, 1281–1287 (1995).
- [85] L. Trintinalia and H. Ling, “Integral equation modeling of multilayered doubly-periodic lossy structures using periodic boundary condition and a connection scheme,” *Antennas and Propagation, IEEE Transactions on* **52**, 2253–2261 (2004).
- [86] I. Stevanovic, P. Crespo-Valero, K. Blagovic, F. Bongard, and J. R. Mosig, “Integral-equation analysis of 3-D metallic objects arranged in 2-D lattices using the Ewald transformation,” *IEEE Transactions on Microwave Theory and Techniques* **54**, 3688–3697 (2006).
- [87] C.-T. Tai, *Dyadic Green Functions in Electromagnetic Theory*, IEEE Series on Electromagnetic Waves (IEEE, 1994), 2nd ed.
- [88] W. Ludwig and C. Falter, *Symmetries in Physics: Group Theory Applied to Physical Problems*, vol. 64 of *Springer Series in Solid-State Sciences* (Springer-Verlag, 1988).
- [89] A. Rathsfeld, G. Schmidt, and B. H. Kleemann, “On a fast integral equation method for diffraction gratings,” *Communications in computational physics* **1**, 984–1009 (2006).
- [90] F. Capolino, D. R. Wilton, and W. A. Johnson, “Efficient computation of the 3D Green’s function for the Helmholtz operator for a linear array of point sources using the Ewald method,” *J. Comput. Phys.* **223**, 250–261 (2007).
- [91] I. Stevanovic and J. R. Mosig, “Periodic Green’s function for skewed 3-D lattices using the Ewald transformation,” *Microw. Opt. Technol. Lett.* **49**, 1353–1357 (2007).
- [92] G. Valerio, P. Baccarelli, P. Burghignoli, and A. Galli, “Comparative analysis of acceleration techniques for 2-d and 3-d green’s functions in periodic structures along one and two directions,” *IEEE Transactions on Antennas and Propagation* **55**, 1630 (2007).
- [93] K. E. Jordan, G. R. Richter, and P. Sheng, “An efficient numerical evaluation of the green-function for the helmholtz operator on periodic structures,” *Journal of Computational Physics* **63**, 222–235 (1986).
- [94] S. Rao, D. Wilton, and A. Glisson, “Electromagnetic scattering by surfaces of arbitrary shape,” *IEEE Transactions on Antennas and Propagation* **30**, 409–418 (1982).
- [95] P. Ylä-Oijala, M. Taskinen, and J. Sarvas, “Surface integral equation method for general composite metallic and dielectric structures with junctions,” *Progress In Electromagnetics Research-PIER* **52**, 81–108 (2005).

## Bibliography

---

- [96] G. R. Cowper, “Gaussian quadrature formulas for triangles,” *Int. J. Numer. Methods Eng.* **7**, 405–408 (1973).
- [97] T. K. Wu and L. L. Tsai, “Scattering from arbitrarily-shaped lossy dielectric bodies of revolution,” *Radio science* **12**, 709–718 (1977).
- [98] X. Q. Sheng, J. M. Jin, J. M. Song, W. C. Chew, and C. C. Lu, “Solution of combined-field integral equation using multilevel fast multipole algorithm for scattering by homogeneous bodies,” *IEEE Transactions on Antennas and Propagation* **46**, 1718–1726 (1998).
- [99] P. Ylä-Oijala and M. Taskinen, “Application of combined field integral equation for electromagnetic scattering by dielectric and composite objects,” *IEEE Transactions on Antennas and Propagation* **53**, 1168–1173 (2005).
- [100] I. Hanninen, M. Taskinen, and J. Sarvas, “Singularity subtraction integral formulae for surface integral equations with RWG, rooftop and hybrid basis functions,” *Progress in Electromagnetics Research-PIER* **63**, 243–278 (2006).
- [101] E. Anderson, Z. Bai, C. Bischof, S. Blackford, J. Demmel, J. Dongarra, J. Du Croz, A. Greenbaum, S. Hammarling, A. McKenney, and D. Sorensen, *LAPACK Users’ Guide* (Society for Industrial and Applied Mathematics, Philadelphia, PA, 1999), 3rd ed.
- [102] P. B. Johnson and R. W. Christy, “Optical-Constants of Noble-Metals,” *Phys. Rev. B* **6**, 4370 (1972).
- [103] G. Dolling, M. Wegener, C. M. Soukoulis, and S. Linden, “Negative-index metamaterial at 780 nm wavelength,” *Opt. Lett.* **32**, 53–55 (2007).
- [104] D. R. Smith, S. Schultz, P. Markos, and C. M. Soukoulis, “Determination of effective permittivity and permeability of metamaterials from reflection and transmission coefficients,” *Phys. Rev. B* **65**, 195104 (2002).
- [105] B. Gallinet and O. J. F. Martin, “The relation between near-field and far-field properties of plasmonic Fano resonances,” *Opt. Express* **19**, 22167–22175 (2011).
- [106] B. Gallinet and O. J. F. Martin, “Influence of electromagnetic interactions on the line shape of plasmonic Fano resonances,” *ACS Nano* **5**, 8999–9008 (2011).
- [107] A. Christ, O. J. F. Martin, Y. Ekinici, N. A. Gippius, and S. G. Tikhodeev, “Symmetry breaking in a plasmonic metamaterial at optical wavelength,” *Nano Lett.* **8**, 2171–2175 (2008).
- [108] M. Hentschel, M. Saliba, R. Vogelgesang, H. Giessen, A. P. Alivisatos, and N. Liu, “Transition from Isolated to Collective Modes in Plasmonic Oligomers,” *Nano Lett.* **10**, 2721–2726 (2010).

- 
- [109] Y. Sonnefraud, N. Verellen, H. Sobhani, G. A. E. Vandenbosch, V. V. Moshchalkov, P. Van Dorpe, P. Nordlander, and S. A. Maier, “Experimental realization of subradiant, superradiant, and fano resonances in ring/disk plasmonic nanocavities,” *ACS Nano* **4**, 1664–1670 (2010).
- [110] J. A. Fan, C. Wu, K. Bao, J. Bao, R. Bardhan, N. J. Halas, V. N. Manoharan, P. Nordlander, G. Shvets, and F. Capasso, “Self-assembled plasmonic nanoparticle clusters,” *Science* **328**, 1135–1138 (2010).
- [111] W. Zhang, B. Gallinet, and O. J. F. Martin, “Symmetry and selection rules for localized surface plasmon resonances in nanostructures,” *Phys. Rev. B* **81**, 233407 (2010).
- [112] O. J. F. Martin, C. Girard, D. R. Smith, and S. Schultz, “Generalized field propagator for arbitrary finite-size photonic band gap structures,” *Phys. Rev. Lett.* **82**, 315–318 (1999).
- [113] R. Singh, I. A. I. Al-Naib, M. Koch, and W. Zhang, “Sharp Fano Resonances in THz Metamaterials,” *Opt. Express* **19**, 6320–6327 (2011).
- [114] A. Christ, Y. Ekinici, H. H. Solak, N. A. Gippius, S. G. Tikhodeev, and O. J. F. Martin, “Controlling the Fano Interference in a Plasmonic Lattice,” *Phys. Rev. B* **76**, 201405 (2007).
- [115] K. Bao, N. A. Mirin, and P. Nordlander, “Fano Resonances in Planar Silver Nanosphere Clusters,” *Appl. Phys. A-Mater. Sci. Process.* **100**, 333–339 (2010).
- [116] M. Hentschel, D. Dregely, R. Vogelgesang, H. Giessen, and N. Liu, “Plasmonic Oligomers: The Role of Individual Particles in Collective Behavior,” *ACS Nano* **5**, 2042–2050 (2011).
- [117] L. Babic and M. J. A. de Dood, “Interpretation of Fano Lineshape Reversal in the Reflectivity Spectra of Photonic Crystal Slabs,” *Opt. Express* **18**, 26569–26582 (2010).
- [118] M. I. Tribelsky, S. Flach, A. E. Miroschnichenko, A. V. Gorbach, and Y. S. Kivshar, “Light Scattering by a Finite Obstacle and Fano Resonances,” *Phys. Rev. Lett.* **100**, 043903 (2008).
- [119] B. Gallinet, J. Kupec, B. Witzigmann, and M. A. Dupertuis, “Analysis of Photonic Crystal Defect Modes by Maximal Symmetrization and Reduction,” *J. Opt. Soc. Am. B-Opt. Phys.* **27**, 1364–1380 (2010).
- [120] A. Christ, T. Zentgraf, J. Kuhl, S. G. Tikhodeev, N. A. Gippius, and H. Giessen, “Optical Properties of Planar Metallic Photonic Crystal Structures: Experiment and Theory,” *Phys. Rev. B* **70**, 125113 (2004).

## Bibliography

---

- [121] A. Christ, S. G. Tikhodeev, N. A. Gippius, J. Kuhl, and H. Giessen, “Waveguide-Plasmon Polaritons: Strong Coupling of Photonic and Electronic Resonances in a Metallic Photonic Crystal Slab,” *Phys. Rev. Lett.* **91**, 183901 (2003).
- [122] C. Genet, M. P. van Exter, and J. P. Woerdman, “Fano-Type Interpretation of Red Shifts and Red Tails in Hole Array Transmission Spectra,” *Optics Communications* **225**, 331 (2003).
- [123] M. Sarrazin, J. P. Vigneron, and J. M. Vigoureux, “Role of Wood anomalies in Optical Properties of Thin Metallic Films with a Bidimensional Array of Subwavelength Holes,” *Phys. Rev. B* **67**, 085415 (2003).
- [124] A. M. Kern and O. J. F. Martin, “Excitation and reemission of molecules near realistic plasmonic nanostructures,” *Nano Lett.* **11**, 482–487 (2011).
- [125] D. J. Bergman and M. I. Stockman, “Surface Plasmon Amplification by Stimulated Emission of Radiation: Quantum Generation of Coherent Surface Plasmons in Nanosystems,” *Phys. Rev. Lett.* **90**, 027402 (2003).
- [126] N. Liu, M. Hentschel, T. Weiss, A. P. Alivisatos, and H. Giessen, “Three-dimensional plasmon rulers,” *Science* **332**, 1407–1410 (2011).
- [127] C. Sonnichsen, B. M. Reinhard, J. Liphardt, and A. P. Alivisatos, “A molecular ruler based on plasmon coupling of single gold and silver nanoparticles,” *Nat. Biotechnol.* **23**, 741–745 (2005).
- [128] T. Sannomiya, C. Hafner, and J. Voeroes, “Strain mapping with optically coupled plasmonic particles embedded in a flexible substrate,” *Opt. Lett.* **34**, 2009–2011 (2009).
- [129] Fabrication of the samples with extreme ultraviolet lithography and experimental reflectance spectra are courtesy of Thomas Siegfried, Paul Scherrer Institute, Villigen, Switzerland.
- [130] T. Siegfried, Y. Ekinici, H. H. Solak, O. J. F. Martin, and H. Sigg, “Fabrication of sub-10 nm gap arrays over large areas for plasmonic sensors,” *Appl. Phys. Lett.* **99**, 263302 (2011).
- [131] N. L. Bocchio, A. Unger, M. Alvarez, and M. Kreiter, “Thin layer sensing with multipolar plasmonic resonances,” *J. Phys. Chem. C* **112**, 14355–14359 (2008).
- [132] A. Unger and M. Kreiter, “Analyzing the Performance of Plasmonic Resonators for Dielectric Sensing,” *J. Phys. Chem. C* **113**, 12243–12251 (2009).
- [133] Y. Zhang, N. K. Grady, C. Ayala-Orozco, and N. J. Halas, “Three-dimensional nanostructures as highly efficient generators of second harmonic light,” *Nano Lett.* **11**, 5519–5523 (2011).

- [134] L. Sherry, S. Chang, G. Schatz, R. Van Duyne, B. Wiley, and Y. Xia, “Localized surface plasmon resonance spectroscopy of single silver nanocubes,” *Nano Lett.* **5**, 2034–2038 (2005).
- [135] J. N. Anker, W. P. Hall, O. Lyandres, N. C. Shah, J. Zhao, and R. P. Van Duyne, “Biosensing with plasmonic nanosensors,” *Nat. Mater.* **7**, 442–453 (2008).
- [136] J. N. W. J. D. Joannopoulos, S. G. Johnson and R. D. Meade, *Photonic Crystals: Molding the Flow of Light* (Princeton University Press, 2nd ed, 2008).
- [137] R. Aaswath and S. Fan, “Perturbation theory for plasmonic modulation and sensing,” *Phys. Rev. B* **83**, 205131 (2011).
- [138] E. Cubukcu, S. Zhang, Y.-S. Park, G. Bartal, and X. Zhang, “Split ring resonator sensors for infrared detection of single molecular monolayers,” *Appl. Phys. Lett.* **95**, 043113 (2009).
- [139] M. Guillaumee, L. A. Dunbar, C. Santschi, E. Grenet, R. Eckert, O. J. F. Martin, and R. P. Stanley, “Polarization sensitive silicon photodiodes using nanostructured metallic grids,” *Appl. Phys. Lett.* **94**, 193503 (2009).
- [140] T. Sandén, R. Wyss, C. Santschi, G. Hassaine, C. Deluz, O. J. Martin, S. Wennmalm, and H. Vogel, “A zeptoliter volume meter for analysis of single protein molecules,” *Nano Lett.* **12**, 370–375 (2012).
- [141] V. M. Sundaram and S.-B. Wen, “An easy method to perform e-beam negative tone lift-off fabrication on dielectric material with a sandwiched conducting polymer layer,” *J. Micromech. Microeng.* **21**, 065021 (2011).
- [142] S. Chou, P. Krauss, and P. Renstrom, “Imprint lithography with 25-nanometer resolution,” *Science* **272**, 85–87 (1996).
- [143] Nanoimprint fabrication by Vaida Auzelyte and Valentin Flauraud, STI-IMT-LMIS, Ecole Polytechnique Fédérale de Lausanne, Switzerland. Focused Ion Beam cross sections by Christian Santschi, STI-IMT-NAM, Ecole Polytechnique Fédérale de Lausanne, Switzerland.
- [144] Experimental extinction spectra by Shourya Dutta-Gupta, STI-IMT-NAM, Ecole Polytechnique Fédérale de Lausanne, Switzerland.
- [145] N. Liu, H. Guo, L. Fu, S. Kaiser, H. Schweizer, and H. Giessen, “Three-dimensional photonic metamaterials at optical frequencies,” *Nat. Mater.* **7**, 31–37 (2008).
- [146] H. Tuovinen, M. Kauranen, K. Jefimovs, P. Vahimaa, T. Vallius, J. Turunen, N. V. Tkachenko, and H. Lemmetyinen, “Linear and second-order nonlinear optical properties of arrays of noncentrosymmetric gold nanoparticles,” *J. Nonlinear Opt. Phys. Mater.* **11**, 421–432 (2002).

## Bibliography

---

- [147] W. Zhang, L. Huang, C. Santschi, and O. J. F. Martin, “Trapping and sensing 10 nm metal nanoparticles using plasmonic dipole antennas,” *Nano Lett.* **10**, 1006–1011 (2010).
- [148] G. A. E. Vandenbosch, V. Volski, N. Verellen, and V. V. Moshchalkov, “On the use of the method of moments in plasmonic applications,” *Radio Sci.* **46**, RS0E02 (2011).
- [149] J. M. Taboada, J. Rivero, F. Obelleiro, M. G. Araujo, and L. Landesa, “Method-of-moments formulation for the analysis of plasmonic nano-optical antennas,” *J. Opt. Soc. Am. A-Opt. Image Sci. Vis.* **28**, 1341–1348 (2011).
- [150] J. Makitalo, S. Suuriniemi, and M. Kauranen, “Boundary element method for surface nonlinear optics of nanoparticles,” *Opt. Express* **19**, 23386–23399 (2011).
- [151] M. Paulus and O. J. F. Martin, “Green’s tensor technique for scattering in two-dimensional stratified media,” *Phys. Rev. E* **63**, 066615 (2001).
- [152] R. A. Kipp and C. H. Chan, “A numerically efficient technique for the method of moments solution for planar periodic structures in layered media ,” *IEEE Trans. Microw. Theory Tech.* **42**, 635–643 (1994).
- [153] W. Zhuang, R. S. Chen, and D. Z. Ding, “An efficient evaluation of the green’s functions for periodic structures in multilayered media,” *Microw. Opt. Technol. Lett.* **51**, 2639–2643 (2009).
- [154] D. Brunazzo, E. Descrovi, and O. J. F. Martin, “Narrowband optical interactions in a plasmonic nanoparticle chain coupled to a metallic film,” *Opt. Lett.* **34**, 1405–1407 (2009).
- [155] S. Cataldo, J. Zhao, F. Neubrech, B. Frank, C. Zhang, P. V. Braun, and H. Giessen, “Hole-Mask Colloidal Nano lithography for Large-Area Low-Cost Metamaterials and Antenna-Assisted Surface-Enhanced Infrared Absorption Substrates,” *ACS Nano* **6**, 979–985 (2012).

# Curriculum Vitæ

## Personal Information

Name: Benjamin Gallinet

Date of birth: May 9, 1987

Nationality: French

Address: Route de Chavannes 39, CH-1007, Lausanne, Switzerland

## Education

2009-present Doctoral education at the School of Engineering, Photonics Doctoral School, Ecole Polytechnique Fédérale de Lausanne (EPFL), Switzerland. Thesis in collaboration with Centre Suisse d'Electronique et de Microtechnique (CSEM SA) and BASF AG.

2004-2009 Master in Physical Engineering. Thesis in collaboration with the Swiss Federal Institute of Technology Zurich (ETHZ), awarded by the Prize Jean Landry for a scientific work with original research.

2007 Academic exchange year Carnegie Mellon University (CMU), Pittsburgh PA.

2004 Scientific baccalaureate in France (mathematics and physics).

## Academic working experience

2011-present Peer-reviewing activity for IEEE Photonics Technology Letters, International Journal of Optics, Photonics and Nanostructures: Fundamentals and Applications, Journal of the Optical Society of America, ACS Nano.

2009-present Teaching assistant for "Applied photonics" and "Ingénierie optique", supervision of students projects.

## Languages

French Mother tongue

English Fluent

German Conversational

## Peer-reviewed publications

- B. Gallinet, O. J. F. Martin, "Influence of Electromagnetic Interactions on the Line Shape of Plasmonic Fano Resonances", ACS Nano **5**, 8999-9008 (2011)

- B. Gallinet, O. J. F. Martin, "Relation between near-field and far-field properties of plasmonic Fano resonances", *Optics Express* **19**, 22167-22175 (2011)
- B. Gallinet, O. J. F. Martin, "Ab initio theory of Fano resonances in plasmonic nanostructures and metamaterials", *Physical Review B* **83**, 235427 (2011)
- B. Gallinet, A. M. Kern, O. J. F. Martin, "Accurate and versatile modeling of electromagnetic scattering on periodic nanostructures with a surface integral approach", *Journal of the Optical Society of America A* **27**, 2261-2271 (2010)
- B. Gallinet, O. J. F. Martin, "Scattering on plasmonic nanostructures arrays modeled with a surface integral formulation", *Photonics and Nanostructures: Fundamentals and Applications* **8**, 278-284 (2010)
- B. Gallinet, J. Kupec, B. Witzigmann, M.-A. Dupertuis, "Analysis of photonic crystal defect modes by maximal symmetrization and reduction", *Journal of the Optical Society of America B* **27**, 1364-1380 (2010)
- W. Zhang, B. Gallinet, O. J. F. Martin, "Symmetry and selection rules for localized surface plasmon resonances in nanostructures", *Physical Review B* **81**, 233407 (2010)

### Oral Presentations

- Contributed: "Ab Initio Electromagnetic Theory of Fano Resonances in Plasmonic Nanostructures", Progress in Electromagnetic Research (PIERS), Kuala Lumpur, Malaysia, March 25-29 2012
- Contributed: "Ab initio engineering of Fano resonances", Plasmonics - Metallic Nanostructures and Their Optical Properties IX (SPIE), San Diego, California, August 21-25 2011
- Contributed: "Analytical description of Fano resonances in plasmonic nanostructures", International Workshop on Theoretical and Computational Nano-Photonics (Tacona-Photonics), Bad Honnef, Germany, 24-26 October 2011
- Invited: "Surface Integral Modeling of Plasmonic and High Permittivity Nanostructures", International Conference on Computational and Mathematical Methods in Science and Engineering (CMMSE), Alicante, Spain, June 26-29 2011
- Invited: "Fano resonances in plasmonic nanostructures", Polydôme EPFL, November 4<sup>th</sup> 2011
- Contributed: "Multiscale and accurate modeling of high permittivity and plasmonic nanostructures", Integrated Photonics Research, Silicon and Nano Photonics (IPR), Monterey, California, July 25-28 2010
- Contributed: "Electromagnetic scattering on periodic structures, a surface integral simulation tool", International Workshop on Theoretical and Computational Nano-Photonics (Bad Honnef, Germany, 28-30 October 2009)